DTIC FILE COPY

2

AD-A223 144

Development of Metastable Processing Paths
for
High Temperature Alloys

Final Technical Report
submitted to
Defense Advanced Research Projects Agency (DoD)
for the period
January 1, 1987 through December 31, 1989

Contractor: Metallurgy Division
National Institute of Standards and Technology
Gaithersburg, MD 20899

Principal Investigator: William J. Boettinger
301-975-6160

Senior Project Scientists: Leonid A. Bendersky
John W. Cahn
Ursula R. Kattner
Benjamin A. Burton

Effective Date of Contract: February 9, 1987

Contract Expiration Date: December 31, 1989

Amount of Contract: $600,000

ARPA Order Number: 6065

Program Code Number: 7D10

DTIC
S ELECTE D
JUN 22 1990
E

Notice: Approved for public release. Distribution unlimited

90 06 22 157

UNCLASSIFIED
SECURITY CLASSIFICATION OF THIS PAGE

REPORT DOCUMENTATION PAGE

Form Approved
OMB No. 0704-0188

1a. REPORT SECURITY CLASSIFICATION: UNCLASSIFIED

1b. RESTRICTIVE MARKINGS: None

2a. SECURITY CLASSIFICATION AUTHORITY: N/A

2b. DECLASSIFICATION/DOWNGRADING SCHEDULE: N/A

3. DISTRIBUTION/AVAILABILITY OF REPORT: Approved for Public Release
Distribution Unlimited

4. PERFORMING ORGANIZATION REPORT NUMBER(S): N/A

5. MONITORING ORGANIZATION REPORT NUMBER(S):

6a. NAME OF PERFORMING ORGANIZATION: Metallurgy Div., NIST

6b. OFFICE SYMBOL *(If applicable)*: 450

7a. NAME OF MONITORING ORGANIZATION:

6c. ADDRESS *(City, State, and ZIP Code)*: Gaithersburg, MD 20899

7b. ADDRESS *(City, State, and ZIP Code)*:

8a. NAME OF FUNDING/SPONSORING ORGANIZATION: DARPA

8b. OFFICE SYMBOL *(If applicable)*:

9. PROCUREMENT INSTRUMENT IDENTIFICATION NUMBER:

8c. ADDRESS *(City, State, and ZIP Code)*:

10. SOURCE OF FUNDING NOS.

PROGRAM ELEMENT NO.	PROJECT NO.	TASK NO.	WORK UNIT ACCESSION NO.

11. TITLE *(Include Security Classification)*: Development of Metastable Processing Paths for High Temperature Alloys

12. PERSONAL AUTHOR(S): W.J. Boettinger, L.A. Bendersky, J.W. Cahn, and U.R. Kattner

13a. TYPE OF REPORT: Annual Technical

13b. TIME COVERED: FROM 1/1/87 TO 12/31/89

14. DATE OF REPORT *(Year, Month, Day)*: June 15, 1990

15. PAGE COUNT: 92

16. SUPPLEMENTARY NOTATION

17. COSATI CODES

FIELD	GROUP	SUB. GR.

18. SUBJECT TERMS ~~(Continue on reverse if necessary and identify by block number)~~: Intermetallics, Ti/Nb Aluminides, Phase Diagram, Rapid Solidification, Ternary Alloys, Solid State Quenching.

19. ABSTRACT *(Continue on reverse if necessary and identify by block number)*

The development of acceptable toughness and creep strength in high temperature intermetallic alloy matrices is closely related to the formation of proper distributions of second phase particles. Phases are needed both to arrest crack growth as low temperatures and to resist creep at high temperatures. The possibility of developing new processing strategies for high temperature intermetallic compounds has been investigated. In particular rapid solidification and/or rapid solid state quenching followed by controlled heat treatment can provide new and unusual microstructures of multiphase materials. This report describes research to: (a) develop an experimental basis and predictive models for solubility extension and metastable phase formation of intermetallic compounds by rapid solidification, (b) analyze the kinetics of decomposition of metastable phases involving ordering and (c) improve the phase diagram modeling of systems involving ordered phases. In (b) and (c), the focus has been on alloys in the Ti-Al-Nb system in which basic phase diagram and phase transformation data were previously quite limited.

20. DISTRIBUTION/AVAILABILITY OF ABSTRACT
☒ UNCLASSIFIED/UNLIMITED
☐ SAME AS RPT. ☐ DTIC USERS

21. ABSTRACT SECURITY CLASSIFICATION: UNCLASSIFIED

22a. NAME OF RESPONSIBLE INDIVIDUAL: W.J. Boettinger

22b. TELEPHONE (Include Area Code): 301-975-6160

22c. OFFICE SYMBOL: 450

DD Form 1473, JUN 86 *Previous editions are obsolete.*

UNCLASSIFIED
SECURITY CLASSIFICATION OF THIS PAGE

Development of Metastable Processing Paths
for
High Temperature Alloys

Final Technical Report
submitted to
Defense Advanced Research Projects Agency (DoD)
for the period
January 1, 1987 through December 31, 1989

Contractor: Metallurgy Division
National Institute of Standards and Technology
Gaithersburg, MD 20899

Principal Investigator: William J. Boettinger
301-975-6160

Senior Project Scientists: Leonid A. Bendersky
John W. Cahn
Ursula R. Kattner
Benjamin A. Burton

Effective Date of Contract: February 9, 1987

Contract Expiration Date: December 31, 1989

Amount of Contract: $600,000

ARPA Order Number: 6065

Program Code Number: 7D10

Notice: Approved for public release. Distribution unlimited

Accession For
NTIS GRA&I ☒
DTIC TAB ☐
Unannounced ☐
Justification
By
Distribution/
Availability Codes
Avail and/or
Dist Special
A-1

DTIC
COPY
INSPECTED
6

Table of Contents

Page

Summary 3

Research Highlight - Microstructures of Rapidly Solidified Intermetallics 4

Research Highlight - Progress in Ti-Al-Nb Intermetallics 5

Publications 6

I. Introduction 7

II. Rapid Solidification and Heat Treatment of Ordered Intermetallic Alloys 9

III. Investigation of Phase equilibrium and Transformations in Ti-Al-Nb Alloys 20

IV. Phase Diagram Modeling 23

V. Fiscal Status 43

VI. Appendix - Reprints of Manuscripts 44

Pathways for Microstructural Development in TiAl

Rapid Solidification and Ordering of $L2_1$ and B2 Phases in the NiAl-NiTi System

The Role of Elastic Energy in the Morphological Development of a Ni-Ti-Al Alloy

A Theory for the Trapping of Solute & Disorder in Intermetallic Compounds by Rapid Solidification

Investigation of B2 and Related Phases in the Ti-Al-Nb Ternary System

Omega-related Phases in a Ti-Al-Nb Alloy

The Formation of Ordered ω-Related Phases in Alloys of Composition Ti_4Al_3Nb

Coherent Precipitates in the BCC/Orthorhombic Two Phase Field of the Ti-Al-Nb System

Disorder Trapping in Ni_2TiAl (Abstract)

Summary

The development of acceptable toughness and creep strength in high temperature intermetallic alloy matrices is closely related to the formation of proper distributions of second phase particles. Phases are needed both to arrest crack growth at low temperatures and to resist creep at high temperatures. The possibility of developing new processing strategies for high temperature intermetallic compounds has been investigated. In particular rapid solidification and/or rapid solid state quenching followed by controlled heat treatment can provide new and unusual microstructures of multiphase materials. This report describes research performed in the Metallurgy Division at NIST under DARPA order #6065 between 1/1/87 and 12/31/89 to: (a) develop an experimental basis and predictive models for solubility extension and metastable phase formation of intermetallic compounds by rapid solidification, (b) analyze the kinetics of decomposition of metastable phases involving ordering and (c) improve the phase diagram modeling of systems involving ordered phases. In (b) and (c), the focus has been on alloys in the Ti-Al-Nb system in which basic phase diagram and phase transformation data were previously quite limited.

Research Highlight - Microstructures of Rapidly Solidified Intermetallics

One of the major processing paths to produce high temperature intermetallic alloy composites with microstructures designed for specific performance utilizes atomized powers. Powders are being combined with reinforcing fibers and particulate through various consolidation processes such as HIP to produce components. Recently published research, Acta Met. 37 (1989) 3379-3391, performed at NIST under DARPA Order #6065 has placed the prediction of alloy microstructure of atomized (rapidly solidified) intermetallics on a firm theoretical basis. The starting microstructure of the powders determines the microstructure evolution during subsequent processing.

The research treats for the first time the chemically ordered nature of the freezing solid and predicts the range of solidification rates required to achieve certain ideal microstructures. These ideal microstructures consist of solids without the normal segregation found in more slowly frozen material and also the possibility of a chemically disordered form of the intermetallic. Experimental research conducted under the same DARPA Order has shown the feasibility of producing these kinds of ideal structures in intermetallic alloys of NiAl containing Ti (Mat. Sci. and Eng. 98 (1988) 273-276). Heat treatment of these microstructures at temperatures similar to those used in HIP cycles have shown the unique opportunities possible for microstructural control (Scripta Met., 22, 1029-1034 (1988)). Cube-shaped strengthening particles of very hard Ni_2TiAl have been produced in the NiAl matrix. Such ideal microstructure can not be produced using ordinary cast material of this and many other alloy compositions.

Research Highlight - Progress in Ti-Al-Nb Intermetallics

Investigation of the phase diagram of the Ti-Al-Nb system at NIST under DARPA Order # 6065 has lead to the discovery of a new phase with a composition near Ti_4Al_3Nb. This phase appears in equilibrium with γ-TiAl and α_2-Ti_3Al at 700°C and has the crystal structure of an ordered hexagonal omega phase designated $B8_2$.

The discovery of the phase will guide future alloy development in this alloy system in two opposing directions. Because omega phases in large volume fractions often lead to brittle behavior, alloys in this composition range should perhaps be avoided. One the other hand, with a lower Nb content, the possibility of improved creep strength of two phase α_2 plus γ alloys using a very fine dispersion of this newly discovered phase is a possibility. A second positive example possible with higher Nb contents would involve two-phase microstructures of this new phase with the ductile orthorhombic phase Ti_2AlNb. Above 1100°C these compositions convert to an ordered BCC phase providing the opportunity for solution heat treatment and conversion to multiphase structures with a wide variety of microstructures for use at 1000°C. The details of the formation of the $B8_2$ phase from the high temperature ordered bcc phase are described in a paper in press in Acta Metallurgica.

Publications produced with full or partial support under DARPA Order #6065, 1/1/87 to 1/1/90

Rapid Solidification and Heat Treatment of Ordered Intermetallic Alloys

1. "Pathways for Microstructural Development in TiAl," L. A. Bendersky, J. A. Graves, F. S. Biancaniello, J. H. Perepezko and W. J. Boettinger, Mat. Sci. and Eng., 98, 265-268 (1988).
2. "Rapid Solidification and Ordering of $L2_1$ and B2 Phases in the NiAl-NiTi Systems," W. J. Boettinger, L. A. Bendersky, F. S. Biancaniello and J. W. Cahn, Mat. Sci. and Eng., 98, 273-276 (1988).
3. "The Role of Elastic Energy in the Morphological Development of a Ni-Ti-Al Alloy," L. A. Bendersky, P. W. Voorhees, W. J. Boettinger and W. C. Johnson, Scripta Met., 22, 1029-1034 (1988).
4. "A Theory for the Trapping of Solute & Disorder in Intermatallic Compounds by Rapid Solidification," W.J. Boettinger and M.J. Aziz, Acta. Met. 37, 3379-3392, (1989).

Investigation of Phase equilibrium and Transformations in Ti-Al-Nb Alloys

5. "Investigation of B2 and Related Phases in the Ti-Al-Nb Ternary System," L. A. Bendersky & W. J. Boettinger, Mat. Res. Soc. Sys. Proc., Mat. Res. Soc. Symp. Proc., 133, 45-50 (1989).
6. "Omega-related Phases in a Ti-Al-Nb Alloy," L. A. Bendersky & W. J. Boettinger, Proceedings of the 47th Annual Mtg of the Electron Microscope Society of America, G. W. Bailey, ed., San Francisco Press, San Francisco, CA (1989) 324-325.
7. "The Formation of Ordered ω-Related Phases in Alloys of Composition Ti_4Al_3Nb," L. A. Bendersky, W. J. Boettinger, B. P. Burton, F. S. Biancaniello and C. B. Shoemaker, Acta Met. 38 (1990), in press.
8. "Coherent Precipitates in the BCC/Orthorhombic Two Phase Field of the Ti-Al-Nb System," L. A. Bendersky, W. J. Boettinger and A. Roytburd, submitted to Acta Metallurgica.

I. Introduction

The development of high temperature materials is closely related to the formulation of processing strategies for chemically ordered phases. Most intermetallic compounds including aluminides, carbides, and silicides as well as high temperature ceramic phases are ordered. However, optimum mechanical properties are likely to come from intimate dispersions of several phases, some of which are ordered. These dispersions can be produced by a phase transformation sequence involving both ordering and phase separation beginning with a solid phase of a carefully selected unstable composition made by rapid solidification or rapid solid state quenching.

Recently, significant advances have occurred in the utilization and understanding of rapid solidification processing of alloys. Factors which promote refined segregation, solubility extension and metastable phase formation have been identified. However, much of this research has been focused towards disordered crystalline phases: i.e., terminal solid solutions, not ordered intermetallic compounds.

At the same time, significant advances have been realized in the thermodynamics and kinetics of order-disorder transitions. The distinction between first and higher order transitions has been clarified, the kinetics of ordering reactions and the structure and mobility of APB's have been determined and reactions that involve fine scale ordering and compositional separation have been studied.

This research attempts to combine the advances in these areas to develop new processing strategies for high temperature ordered multiphase materials.

In section II of this report we describe research focused on determining the possibility of extending the solubility range of ordered phases by rapid solidification. Subsequent heat treatment of these metastable alloys can form stable high temperature multiphase mixtures. This research also includes an examination of the state of nonequilibrium order of rapidly quenched intermetallic compounds.

Section III of this report summarizes research at phase identification and solid state transformation in compositions surrounding Ti_2NbAl in the Ti-Al-Nb alloy system.

Section IV of this report describes phase diagram modelling activities involving ordered phases. A complete reevaluation and calculation of the Nb-Al binary and Nb-Si diagrams have been produced. This is necessary to obtain a thermodynamic calculation of the Ti-Al-Nb and Nb-Al-Si ternary diagrams.

II. Rapid Solidification and Heat Treatment of Ordered Intermetallic Compounds

The study of rapid solidification of intermetallic alloys is important for two reasons. Many processing paths for composites employ blending of reinforcements with alloy powders made by atomization techniques followed by consolidation. Atomized powders, which are of course rapidly solidified, provide reduced segregation and a more ideal starting material of intermetallic alloys for subsequent solid state processing. Second, some rapidly solidified microstructures may provide unique opportunities as precursors to phase transformation paths in the solid state which are not possible with conventionally cast materials. The following topics were investigated.

A. The Microstructure of Rapidly Solidified and Heat Treated Alloys Near the TiAl Composition

Alloys based on the $L1_0$ phase of the Ti-Al system near TiAl are currently being considered for low density, high temperature applications. These alloys may ultimately be used in a form consisting of mixtures of phases such as TiAl with Ti_3Al ($\gamma + \alpha_2$) or TiAl with a BCC phase ($\gamma + \beta$) when Nb is added. Also composites, which may use atomized powders of TiAl, are of interest.

We have examined the microstructure of rapidly solidified melt spun ribbons of alloys between Ti-52 at% Al and Ti-54 at% Al. This work has been performed in close collaboration with Professor John Perepezko under DARPA/URI sponsorship and complements his research on rapidly solidified powders. The results are reported in detail in the reprint in the appendix, ("Pathways for Microstructural Development in TiAl," L. A. Bendersky, J. A. Graves, F. S. Biancaniello, J. H. Perepezko and W. J. Boettinger, Mat. Sci. and Eng., 98, 265-268 (1988)).

Briefly, as-solidified melt spun ribbons were found to contain a dendritic structure of one phase surrounded by a matrix phase. The dendritic phase was the ordered hexagonal phase with DO_{19} structure (α_2). The dendrites contain fine antiphase domains indicating that the ordered phase did not form directly from the liquid phase but formed by solid state reaction. A reasonable conclusion is that the disordered hexagonal (α) phase formed during rapid solidification. The matrix phase in the ribbon structure was the $L1_0$ structure (γ) based on ordered TiAl. Subsequent work by others and stimulated by this research, has found the hexagonal phase to form from the melt even under slow cooling resulting in a change in the equilibrium Ti-Al phase diagram.

The ribbons contained some indication of further solid state transformation. The α_2 structure at these compositions is supersaturated and must eventually decompose to a mixture of α_2 and γ. This transformation takes place by the formation of stacking faults in the DO_{19} phase. These faults locally transform the hexagonal stacking into a FCC stacking. These regions provide the nucleus for plates of the $L1_0$ (γ) phase. The transformation continues by thickening of the γ plates at the expense of the α_2 phase. In heat treated ribbons this process converts the hexagonal phase formed during solidification completely into γ phase.

B. Planar Interface Stability During the Solidification of an Intermetallic Compound

The results of the general theory for interface shape stability are usually given in a form that assumes that the liquidus and solidus lines are straight. For intermetallic compounds these curves are typically curved, especially near a maximum in the liquidus.

An examination of the scientific literature revealed a recent paper (C. Misbah, J. de Physique 47 (1986) 72) which correctly treats this question for the case where local equilibrium is maintained across the liquid solid interface and where the liquidus, T_L, and solidus, T_S, can be represented by parabolic arcs as a function of liquid and solid compositions, C_L and C_S, as

$$T_L = T_M + \alpha_L(C_L - C_M)^2$$

$$T_S = T_M + \alpha_S(C_S - C_M)^2$$

T_M and C_M are the temperature and composition of the congruent maximum (or minimum) in the liquidus and solidus curves and α_L and α_S are constants. By defining new composition variables,

$$\tilde{C}_L = C_L - C_M$$

$$\tilde{C}_S = C_S - C_M$$

a constant equilibrium partition coefficient, k, can be defined by the usual ratio given by

$$k = \frac{\tilde{C}_S}{\tilde{C}_L} = \left[\frac{\alpha_L}{\alpha_S} \right]^{\frac{1}{2}}$$

and a liquidus slope, m, which is not constant but depends on solid composition as

$$m = 2\tilde{C}_L\alpha_L/k.$$

The results of the Misbah theory for this case can be simply obtained by substituting the new composition variable and values for m and k as defined above into the usual theory for straight liquidus and solidus curves; i.e., for absolute stability the velocity v is given by

$$v > \frac{mD_L(1 - k)\tilde{C}_o}{k^2 T_M \Gamma}$$

where D_L is the liquid diffusion coefficient, $\tilde{C}_o$ is the alloy composition in the new composition coordinate and $T_M\Gamma$ is the capillary constant.

Thus the condition for stability of a planar interface for an intermetallic compound can be calculated in a straightforward manner. One might note that for some phases such as TiAl the congruent maximum would be metastable, but values of T_M, C_M, α_m and α_s could be found to fit the liquidus and solidus data where they exist.

C. Theory of Solute & Disorder Trapping by Rapid Solidification

A model has been developed to predict the long range order parameter and composition of a chemically ordered phase as a function of interface velocity. This theory provides a sound basis for alloy selection and for the interpretation of rapid solidification (atomization) processing results on intermetallic alloys. The model is an extension of the solute trapping model of Aziz and relies on an analysis of the interdiffusion across the liquid solid interface between a liquid phase and a solid composed of two sublattices. The model predicts the transition from solidification of a solid phase with equilibrium long range order parameter and with equilibrium partitioning of composition at low interface velocity to solidification of a disordered crystalline solid with the same composition as the liquid at high solidification velocity. For example, solidification velocities have been determined to form, for example, a BCC phase from the melt when a B2 phase is the stable phase or a FCC phase when a $L1_0$ phase is the stable phase.

Experimental results on rapid solidification of intermetallic compounds suggests that solute trapping and disorder trapping do not occur for line compounds under melt spinning conditions (see section D). Trapping seems only to occur for ordered phases in which the ordering is not so strong; i.e., where the equilibrium composition range is large (~10%). The general theory was explored and a simple result related to this point has been obtained. The critical velocity for the trapping of disorder, V_c; i.e., the velocity above which only the disordered variant of the intermetallic compound can form can be estimated from

$$V_C \approx V_D(\frac{T_c}{T_m} - 1)$$

where V_D is the ratio of the interface diffusivity to the jump distance, T_C is the critical temperature for the order-disorder transition and T_m is the melting point of the compound. When the compound is ordered up to its melting point $T_c/T_m > 1$. One can see that the higher T_c, which relates directly to the strength of the ordering, the higher the velocity required to trap disorder. For line compounds $T_c >> T_m$ and thus V_c may be unattainable in normal rapid solidification methods.

Indeed the predictions of this Eqn. can be crudely compared with two experimental results on melt spinning of phases, which if disordered would be FCC. S. C. Huang and E. L. Hall, (Mat. Res. Soc. Symp. Proc., Symp 133, (1989)) have shown that normally $L1_0$ TiAl with ~60 at% Al solidified as FCC during melt spinning. On the contrary DO_{22} Al_3Nb was not altered by melt spinning as described in Section D. For materials parameters we chose V_D as 200 cm/s ($D_i = 4x10^{-6}$ cm^2s^{-1}, $\lambda = 2x10^{-8}$ cm) and T_c/T_m as 1.3 and 2.0 for TiAl and Al_3Nb respectively (Y. A. Chang and J.-C. Lin, Univ. of Wisconsin-Madison, Madison, WI, U.S.A. (1989), private communication), the larger ratio indicating the highly ordered nature of the line compound Al_3Nb. Estimates of the critical velocity for complete disordering of 60 and 200 cm/s respectively are then obtained. Only the former velocity is easily achieved by melt spinning.

The results of this theory have been also been calculated for solids which have first and second order ordering transitions. Discontinuities in both order parameter and solid composition occur when the growth velocity is increased if the equilibrium ordering reaction is first order. In particular the theory predicts the effect of solidification velocity on the segregation coefficient and state of long range order. A paper detailing this theory has been published and is included in the appendix ("A Theory for the Trapping of Solute & Disorder in Intermatallic Compounds by Rapid Solidification," W.J. Boettinger and M.J. Aziz, Acta. Met. 37, 3379-3392, 1989).

D. Attempts at Solubility Extension of the Line Compound (Al_3Nb)

Alloys of composition Al-22 at% Nb and Al-28 at% Nb were prepared by arc melting. These alloys were ± 3 at% on either side of the compound Al_3Nb. Alloys were melt spun on a Cu wheel in a He atmosphere. The produced ribbons were electropolished and examined by transmission electron microscopy. Neither composition was single phase indicating that solubility extension, if present, was less than 3 at%. The Al-22 at% Nb ribbon microstructure consists of cells of the Al_3Nb phase surrounded by FCC aluminum phase. The

Al-28 at% Nb ribbons consist of cells of the Al_3Nb phase surrounded by the σ(Al,Nb) phase. Both are the expected equilibrium solidification structures given by the phase diagram.

In order to establish more quantitatively whether any slight solubility extension was achieved, x-ray powder diffraction was performed in the melt spun ribbons and on equilibrated samples. The Al-28 at% Nb ribbons were heat treated at 500°C for 24 hrs and water quenched. The Al-22 at% Nb ribbons were heat treated at 600°C for 24 hrs and water quenched. Lattice parameters were obtained by Nelson-Riley extrapolation of values obtained from the 200, 220, 400 and 420 peaks to determine the a-lattice parameters. A single 008 peak was used to determine the c-lattice parameter. Other peaks could not be used because of overlaps with the other phases present. The results are given in Table 1 along with the values from the JCPDF files.

Table 1. Summary of Diffraction Results on Al_3Nb Alloys

	a(A)	c(A)	$a^2c(A^3)$	Volume/atom (A^3)
Al-22 at% Nb ribbons	3.8404	8.6112	127.00	15.88
Al-22 at% Nb annealed	3.8397	8.6104	126.95	15.87
Al-23 at% Nb annealed	3.8448	8.6088	127.26	15.91
Al-28 at% Nb ribbon	3.8458	8.6072	127.30	15.91
Al_3Nb (JCPDF)	3.8445	8.601	127.12	15.89

One can see that the Al_3Nb phase in the melt spun ribbon is essentially identical to that in the annealed sample for each composition. The equilibrium width of the single phase Al_3Nb region is certainly greater than any solubility extension. In order to gain an estimate of this range of equilibrium solubility, a plot given in Figure 1 was constructed. The volume/atom is plotted as a function of composition for the single phase regions in the Al-Nb system. One can see a good linear fit to the data from

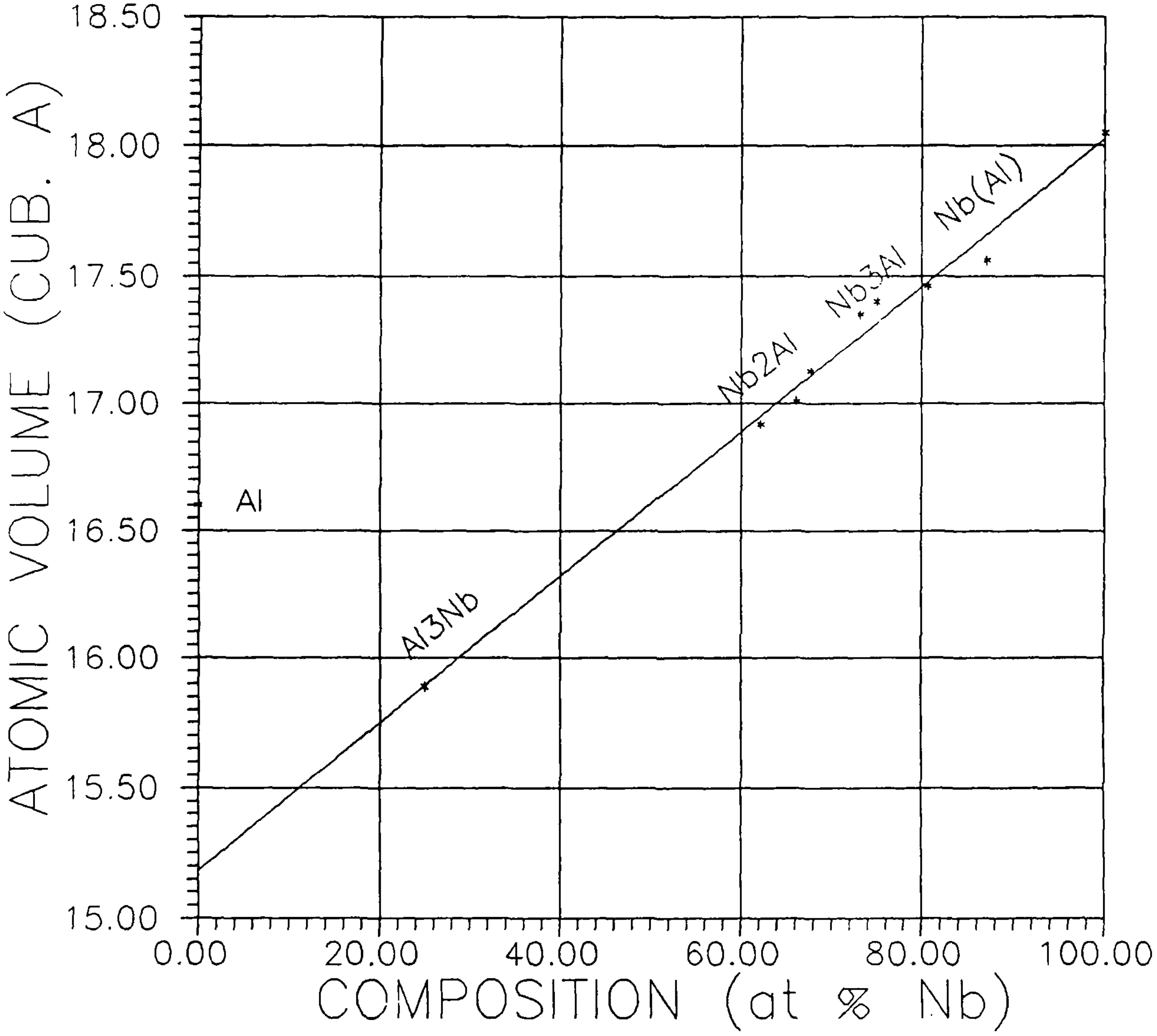

Figure 1 Atomic volume (unit cell volume/number of atoms per unit cell) versus composition for the phases in the Al–Nb system with a linear best fit excluding pure Al.

pure Nb to Al_3Nb. A minimum likely occurs in the plot between Al and Al_3Nb reflecting the change in bonding of the Al atoms. Using the slope obtained from the Nb-rich phases the values in Table 1 can be converted to a composition range of 24.5 to 26.0 at% Nb for the Al_3Nb phase at ~550°C. This estimated for the width of the Al_3Nb single phase field should be a lower bound since any change in slope of the curve in Figure 1 to reach the atomic volume for pure Al would expand the estimate for the range of stoichiometry for Al_3Nb. Thus these initial attempts to extend the solubility of a line compound by rapid solidification (melt spinning) were unsuccessful.

E. Solubility Extension in the NiAl-NiTi Systems

A study of solubility extension by rapid solidification of intermetallic compounds with significant equilibrium ranges of solubility was also undertaken. Alloys belonging to the quasi-binary system containing NiAl, Ni_2AlTi, and NiTi were chosen because the Heusler phase based on the ideal composition Ni_2AlTi(NiAl-NITi) has a crystal structure, $L2_1$ (identical to DO_3), which is an ordered form of the B2 structure. Also this Heusler alloy has demonstrated excellent creep strength (Strutt, Polvani and Ingram, Met. Trans. 7A (1976) 23). Although the solid state B2 to DO_3 transformation satisfies the Landau rules for an allowable higher order transition, the system contains a pair of two phase fields, NiAl + Ni_2AlTi and Ni_2AlTi + NiTi, indicating that the transition is first order at those temperatures. These two-phase fields permit the study of solubility extension by rapid solidification and an exploration of nonequilibrium ordered states and reaction paths.

The results of the rapid solidification experiments are described in detail in the reprint contained in the appendix, ("Rapid Solidification and

Ordering of $L2_1$ and B2 Phases in the NiAl-NiTi Systems," W. J. Boettinger, L. A. Bendersky, F. S. Biancaniello and J. W. Cahn, Mat. Sci. and Eng., 98, 273-276 (1988). Briefly the solubility range of the B2 phases, NiAl and NiTi, were increased. More Ti was forced into the NiAl phase and more Al into NiTi phase than can be obtained by conventional solidification or solution heat treatment. This suggests a kinetic preference for the formation of the B2 phases over the $L2_1$ phase (Ni_2AlTi).

Solid state transformations are quite rapid in this alloy system. The supersaturated B2 orders continuously into single phase $L2_1$ during the solid state cooling of the melt spinning process. Subsequent heat treatment develops two phase microstructures of B2 + $L2_1$. The kinetics of this process has been studied in detail (See Appendix, "The Role of Elastic Energy in the Morphological Development of a Ni-Ti-Al Alloy," L. A. Bendersky, P. W. Voorhees, W. J. Boettinger and W. C. Johnson, Scripta Met., 22, 1029-1034 (1988)). Heat treatment of these microstructures have shown the unique opportunities possible for microstructural control using these ideal starting materials. Cube-shaped strengthening particles of very hard Ni_2TiAl have been produced in the NiAl matrix. Such ideal microstructure can not be produced using ordinary cast material of this and many other alloy compositions.

F. Laser surface melting of Ni_2TiAl

Experimental research on the microstructure of rapidly solidified alloys in the NiAl-NiTi system has continued in collaboration with Professor Mike Aziz of Harvard using pico-second pulse melting. This technique produces solidification rates of 1-5 m/s. Results on alloys with composition Ni_2TiAl show that extremely fine $L2_1$ domains are produced by this technique suggesting that the solidification process produced the B2 phase with subsequent solid state ordering to the $L2_1$ structure. To be certain that a nonequilibrium solidification product was obtained, it was necessary to establish that the $L2_1$ phase exists up to the solidus. Although this is widely accepted in this system, it has never been determined directly. For this purpose we have completed high temperature X-ray diffraction of Ni_2TiAl. A paper, whose abstract is given in the appendix, will be presented at the Seventh International Conference on Rapidly Quenched Metals in Stockholm in August, 1990.

III. Investigation of Phase equilibrium and Transformations in Ti-Al-Nb Alloys

Titanium aluminides (Ti_3Al and TiAl) with ~10 at% Nb additions have received considerable attention as potential low density, high strength and creep resistant materials. However, the phase equilibria in this ternary system is poorly understood. Experimental work has been conducted on ternary alloys in the Ti-Al-Nb system surrounding the composition Ti_2NbAl to determine the phases present at equilibrium at various temperatures and develop an understanding of solid state phase transformations in this system. Extensive TEM investigation and analysis were required to sort out the complex ordering reactions in this important alloy system. Reprints of several papers detailing the results are included in the appendix.

Briefly, results in several areas were obtained. The existence of a broad BCC phase field was found to exist at high temperatures, and for a large range of the phase diagram, the BCC phase is ordered into the B2 or CsCl crystal structure. The extent of this region is given in the paper, Depending on composition, this high temperature B2 phase decomposes during cooling into multiphase alloys involving mixtures of DO_{19} α_2-Ti_3Al, orthorhombic Ti_2AlNb, trigonal ordered ω-phase, hexagonal $B8_2$, or $L1_0$ γ-TiAl.

For an alloy midway between TiAl and Ti_2AlNb (Ti_4Al_3Nb), the formation of an ω-type phase occurs on cooling. This phase transforms at low temperature to a $B8_2$ phase. This transition occurs by a combined dispacive/replacive mechanism with the transformation path following a group/subgroup crystallographic route. Omega phases are brittle and are generally considered deleterious. However fine dispersions created by proper heat treatment may have potential as creep strengthening agents. These transformation results are given in two papers in the appendix, "Omega-related Phases in a Ti-Al-Nb Alloy," L. A. Bendersky & W. J. Boettinger, Proceedings of the 47th Annual Mtg of the Electron Microscope Society of America, G. W. Bailey, ed., San Francisco Press, San Francisco, CA (1989) 324-325, and "The Formation of Ordered ω-Related Phases in Alloys of Composition Ti_4Al_3Nb," L. A. Bendersky, W. J. Boettinger, B. P. Burton, F. S. Biancaniello and C. B. Shoemaker, Acta Met. 38 (1990), in press.

In another investigation, alloys of composition Ti_2AlNb and Ti_4AlNb_3, cooled from 1400°C and equilibrated at 700°C for 26 days, were both found to consist of two phases: the Ti- and Nb-rich bcc phase and the orthorhombic phase based on Ti_2AlNb. Depending on the alloy composition, each phase was observed as a precipitate with a plate morphology in the matrix of the other phase. In both cases the phases share a common direction, $[011]_{bcc} \parallel [001]_{ort}$, and interface (habit) plane, $(2\bar{1}1)_{bcc} \parallel (1\bar{1}0)_{ort}$. Geometrical patterns of plates of the different orientational variants were also observed. Analysis of the orientation relation, habit plane and plate patterns are consistent with the concept of a strain-type transition even though long range diffusion is required. In the Appendix can be found a preprint of a manuscript "Coherent Precipitates in the BCC/Orthorhombic Two Phase Field of the Ti-Al-Nb System," L. A. Bendersky, W. J. Boettinger and A. Roytburd, which has been submitted to Acta Metallurgica.

Results on alloys midway between Ti_3Al and Ti_2AlNb show the equilibrium between α_2 and the orthorhombic phase to be quite difficult to resolve experimentally because the orthorhombic phase is a slightly distorted and more ordered form of α_2. Considerable progress on these alloys was made under this program. Details will follow under a subsequent DARPA program.

These results, combined with those from the University of Wisconsin by J. Perepezko and Y. A. Chang under DARPA sponsorship, will be combined with ternary phase diagram calculations performed under this contract to determine the ternary phase diagrams Ti-Nb-Al.

IV. Phase Diagram Modeling

Good ternary phase diagrams are sorely needed to provide a sound basis for the optimization of processing and microstructure in intermetallic systems. Existing phase diagram and thermodynamic data often exist only in limited composition or temperature ranges. Data can be fit using free energy functions based on reasonable physical models of phases with adjustment of parameters related to these physical models. Diagrams over all composition and temperature ranges can then be calculated. Although phase diagrams based on such modeling can never replace carefully measured diagrams, they do provide a thermodynamically consistent first approximation to the equilibrium diagram. They provide two types of information. Choices of composition and temperature can be determined for critical experiments which minimize the number of alloys prepared. Qualitative features of metastable phase diagrams can be used to guess general processing strategies for specific alloy systems without a knowledge of the precise location of phase boundaries.

As part of an overall objective to produce calculations of the ternary Ti-Al-Nb and Nb-Al-Si systems which are consistent with experimental data, the Nb-Al and Nb-Si binary systems have been reevaluated and modeled thermodynamically. Good binary calculations are necessary for ternary modelling. These ternaries along with Ti-Ta-Al will be completed under future DARPA sponsorship.

A. The Nb-Al (Niobium - Aluminum) System

The Nb-Al System is a relatively simple system with six phases:

- The liquid L

- The bcc (Nb) solid solution, which dissolves up to ~21.5 at.% Al at 2060 °C
- The Nb_3Al phase, with the cubic Cr_3Si structure and a maximum range of homogeneity from 18.6 at.% Al below 1500 °C to 25 at.% Al at 1940 °C, it forms peritectically from the melt and (Nb) at 2060 °C
- The Nb_2Al phase, with the tetragonal σ-CrFe structure and a maximum range of homogeneity from 30 at.% Al below 1500 °C to 42 at.% Al at 1590 °C, it forms peritectically from the melt and Nb_3Al at 1940 °C
- The $NbAl_3$ phase, with the tetragonal $TiAl_3$ structure and a narrow range of homogeneity with a width of ~1 at.%, it forms congruently from the melt at 1680 °C
- The fcc (Al) solid solution with extremely limited solubility of Nb

The assessed phase diagram (Figs 2 - 7) is based on a review of the literature [66Lun, 68Sve, 76Yer, 80Jor, 88Mur]. Although the existence of the three intermediate compounds and the solid-solid phase boundaries of (Nb), Nb_3Al and Nb_2Al are quite well established, the liquidus and reaction temperatures have not been precisely established. Such uncertainties are indicated by dotted lines in the assessed phase diagram.

In splat quenched samples supersaturated solutions of (Nb) (up to 27 at.% Al) and Nb_3Al (27.5 at.% Al) were observed [88Sch]. Supersaturation of the Nb_3Al phase was also obtained using sputter deposited Nb/Al multilayer samples [86Bor, 88Yoo], however there is disagreement whether with this method a supersaturated (Nb) can be obtained.

The Nb_3Al phase is a superconducting compound with a transition temperature of 18.6 K.

Invariant Points of the Assessed Nb-Al Phase Diagram

Reaction	Compositions at.% Al			Temperature °C	Reaction type
(Nb) + L → Nb_3Al	21.5	28	22.5	2060±10	Peritectic
Nb_3Al + L → Nb_2Al	25	32	32	1940±10	Peritectic
L → Nb_2Al + $NbAl_3$	54	42	75	1590±5	Eutectic

L + $NbAl_3$ → (Al)	(99.96)	75	(99.94)	661.4±0.5	Peritectic
L → $NbAl_3$		75		1680±5	Congruent point
L → (Nb)		0		2469	Melting point
L → (Al)		100		660.452	Melting point

Note: Data that are tentative are enclosed in parenthesis

Nb-Al Crystal Structure Data

Phase	Composition at.% Al	Pearson symbol	Space group	Struktur-bericht designation	Proto type
(Nb)	0 - 21.5	cI2	In-3m	A2	W
Nb_3Al	18.6 - 25	cP8	Pm-3n	A15	Cr_3Si
Nb_2Al	30 - 42	tP30	$P4_2/mnm$	...	σ-CrFe
$NbAl_3$	75	tI8	I4/mmm	DO_{22}	$TiAl_3$
(Al)	100	cF4	Fm-3m	A1	Al

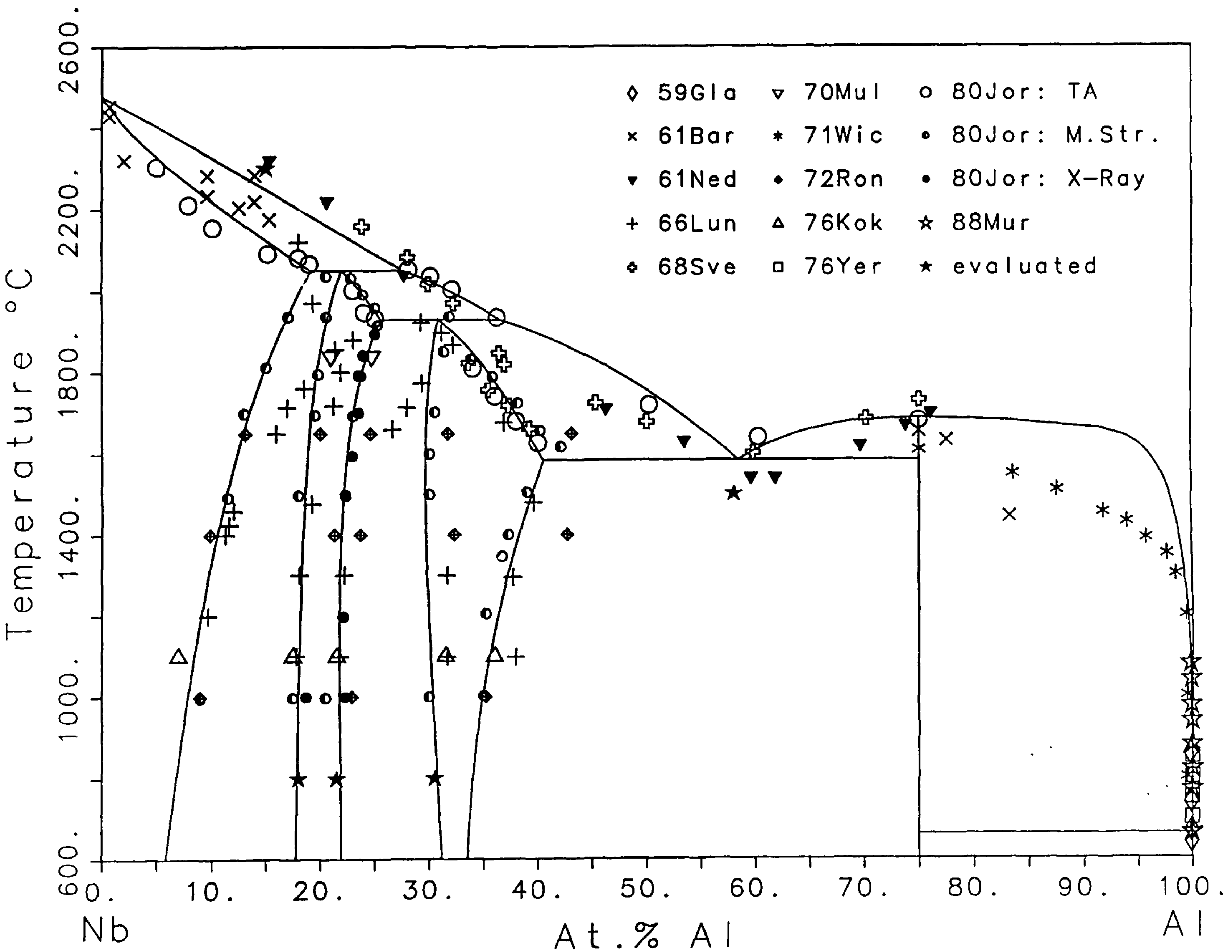

Fig.2: Calculated and measured phase diagram of the Nb-Al system

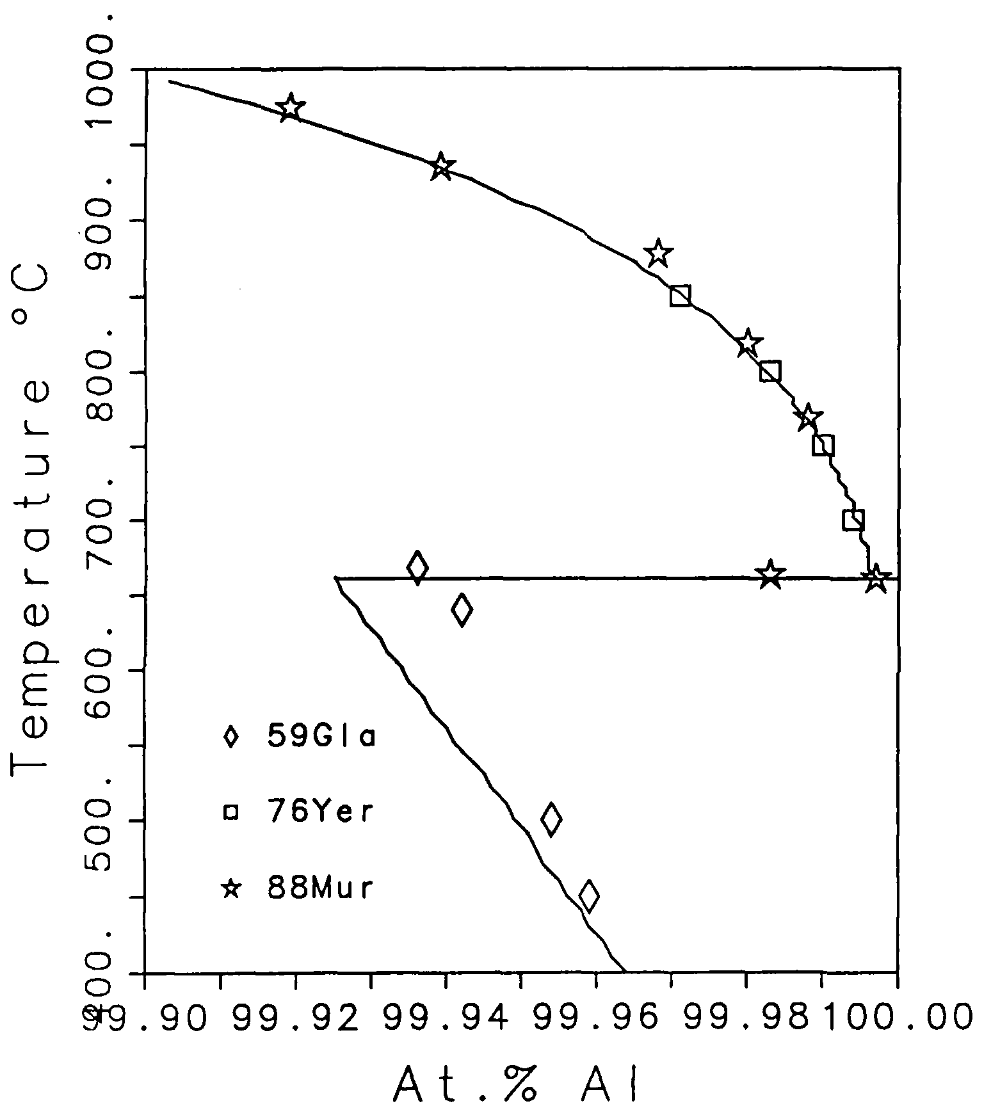

Fig.3: Calculated and measured Al-rich part of the Nb-Al phase diagram

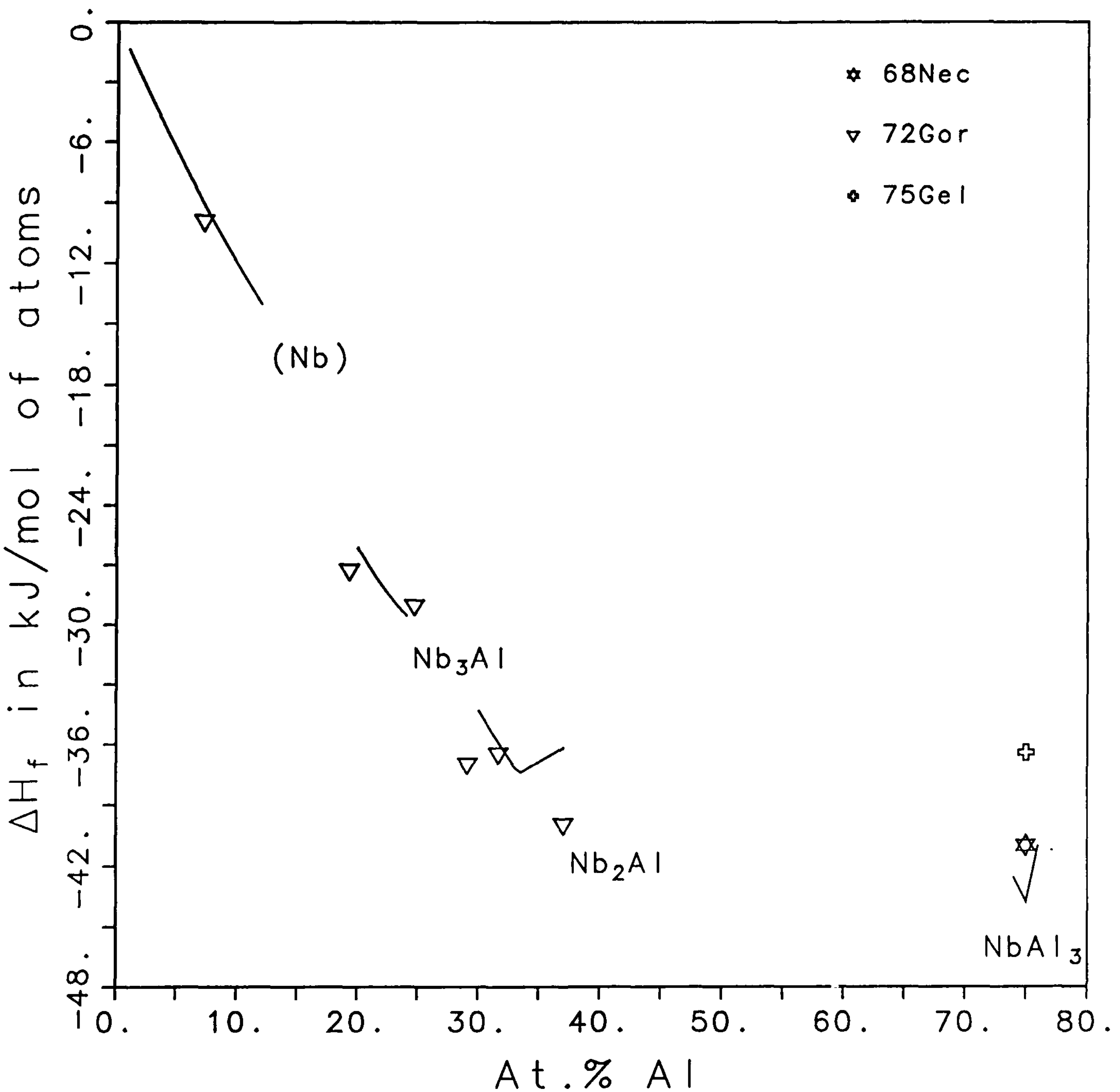

Fig.4: Calculated and measured enthalpies of formation of the solid phases at 25 °C

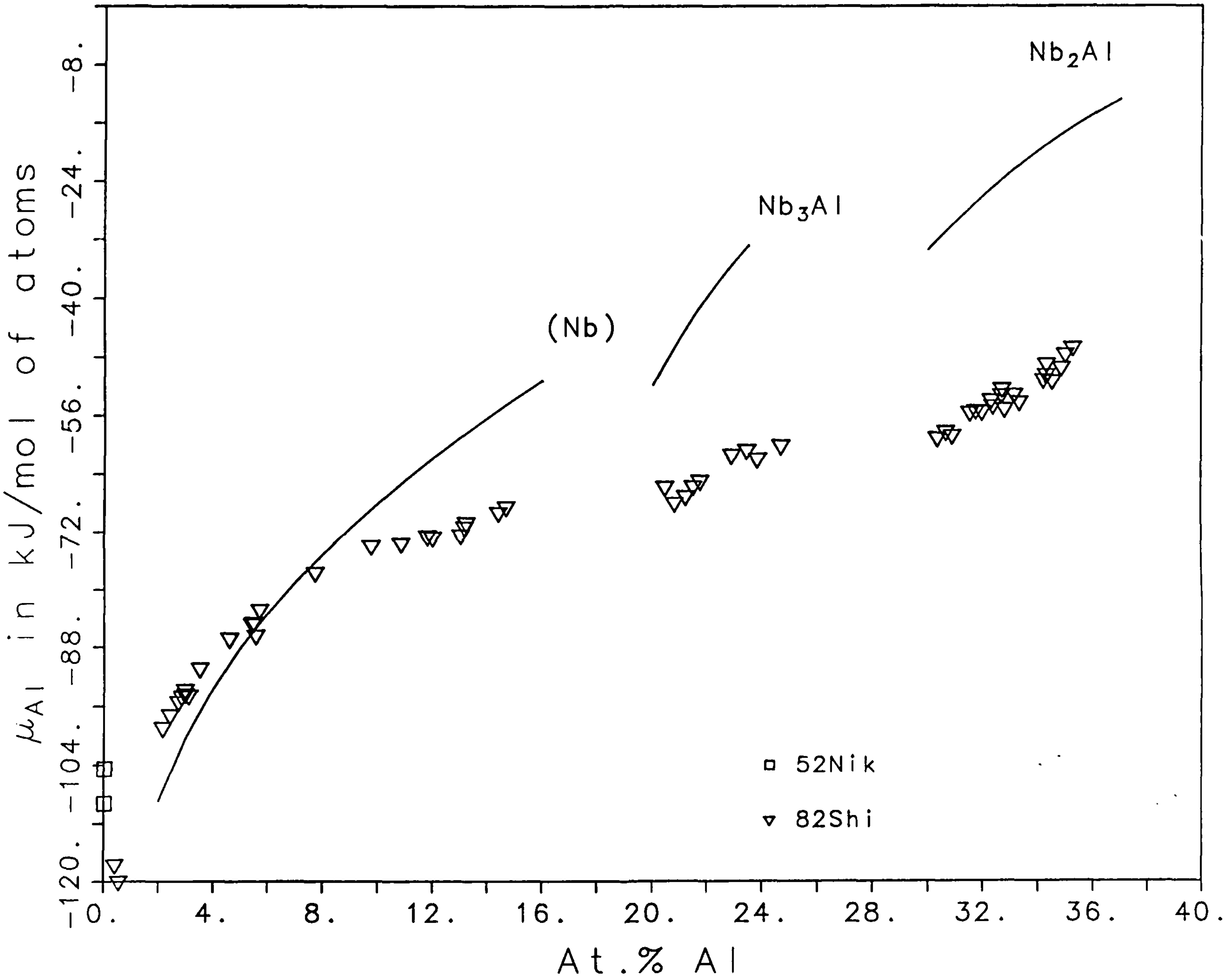

Fig.5: Calculated and measured partial Gibbs energies of Al in the solid phases at 1727 °C (2000 K)

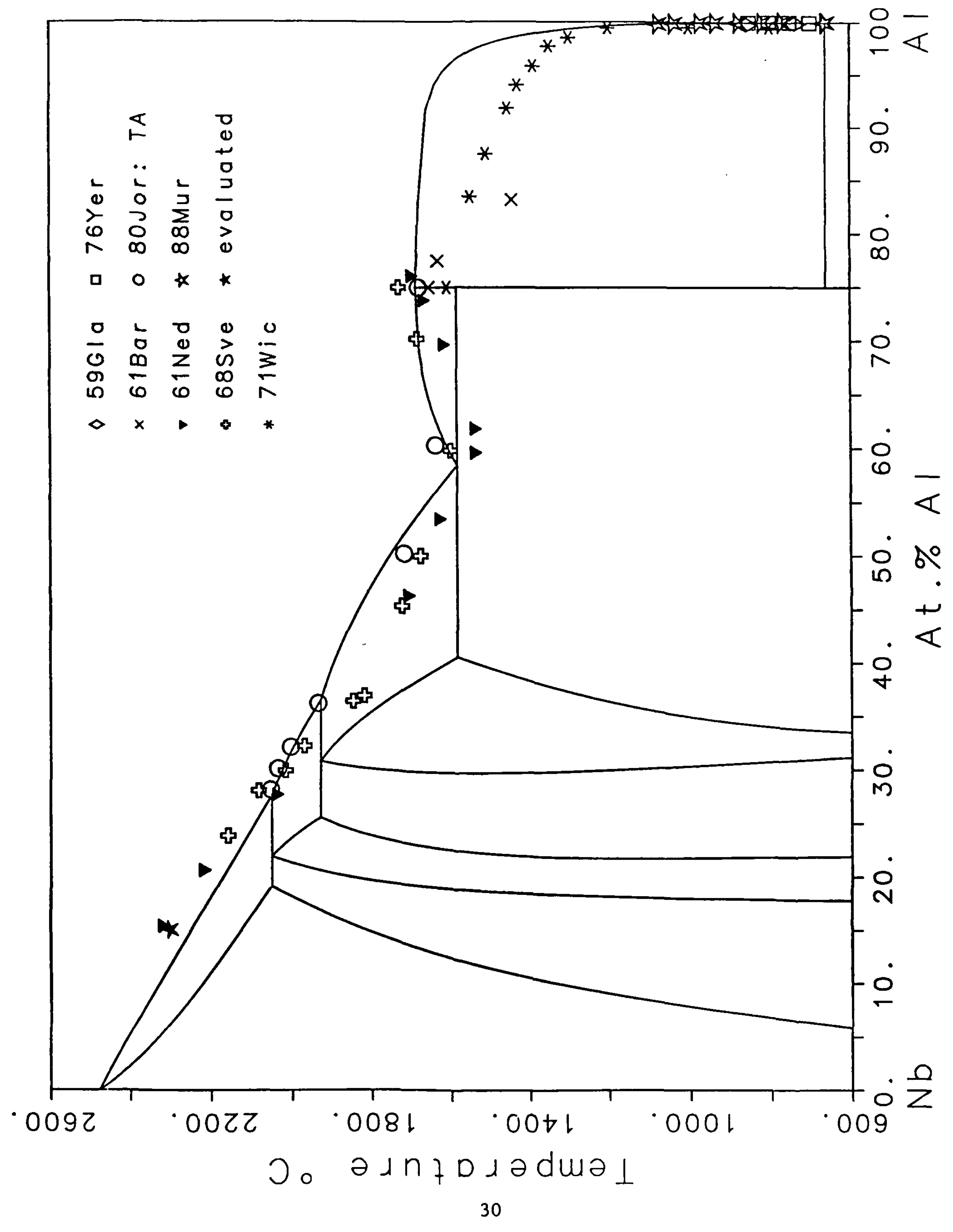

Fig.6: Calculated phase diagram of the Nb-Al system and measured liquidus temperatures

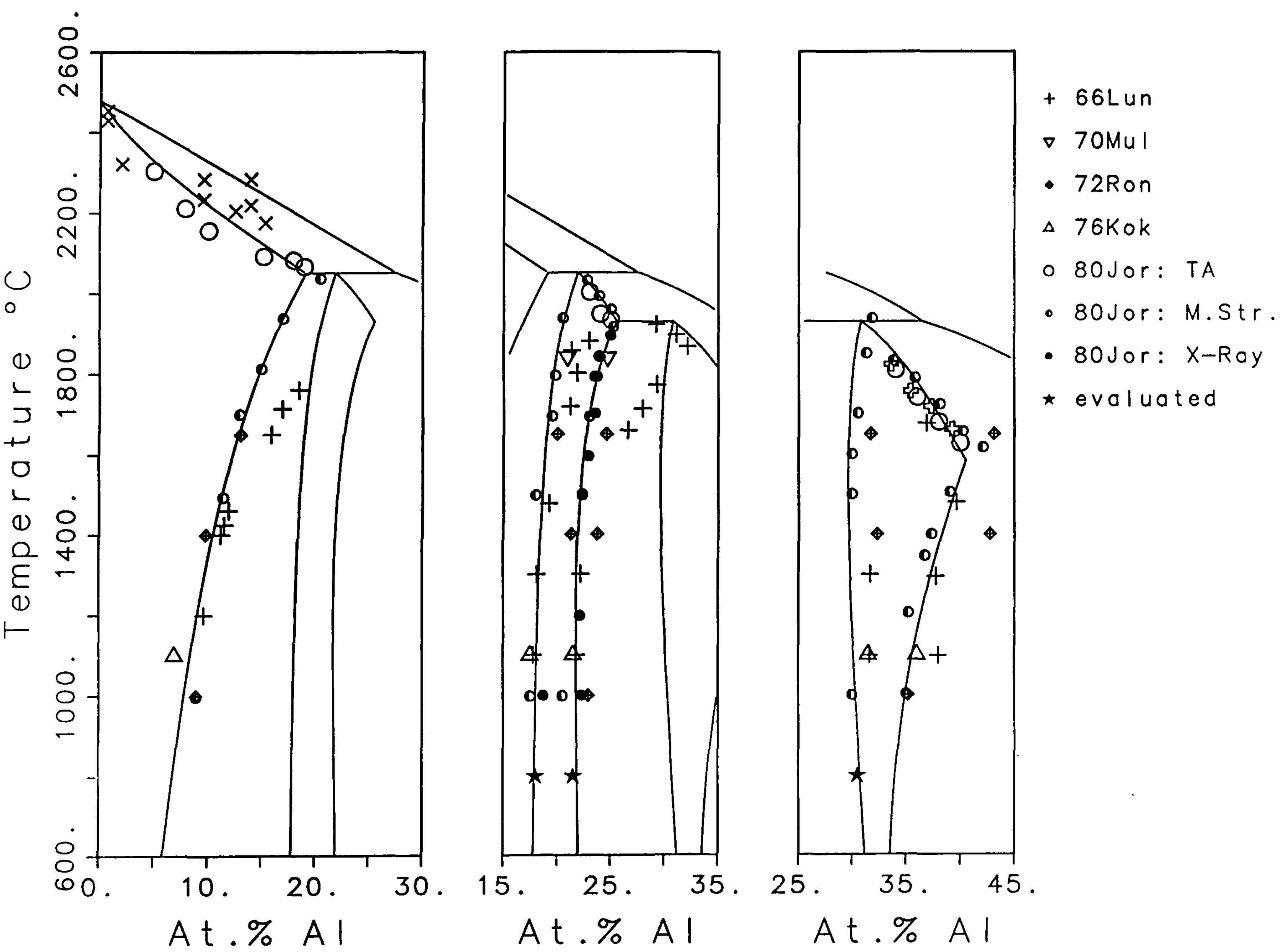

Fig.7: Calculated and measured phases boundaries of the Nb-Al system
a. bcc (Nb) b. Nb_3Al c. Nb_2Al

Thermodynamic Modeling of the Nb-Al System

The equilibrium phase diagram of the Nb-Al system reveals six equilibrium phases, liquid, (Nb), Nb_3Al, Nb_2Al, $NbAl_3$ and (Al). All solid compounds, except (Nb), melt incongruently.

For the calculation of the Nb-Al system the liquid, the bcc (Nb) and fcc (Al) phase were described using regular solution type models. Three polynomial terms for the enthalpy and two for the entropy were used for the liquid, two polynomial terms for the enthalpy and one for the entropy were used for the bcc (Nb) phase and one term for the enthalpy and entropy of fcc (Al) were used. The two intermetallic compounds Nb_3Al and Nb_2Al reveal relatively wide ranges of homogeneity and were therefore modeled with the Wagner-Schottky model. Nb_3Al was described with two sublattices, allowing substitutional solution to occur on each of these sublattices. For the analytical description of this compound four independent and four dependent parameters were used: enthalpy and entropy of formation of the compound without any substitution occurring and enthalpy and entropy of the quasi-regular solution between the regular and substitutional atoms on the Al-sublattice, the enthalpy and entropy of formation of the substitutional atoms were constrained to yield at complete substitution the same Gibbs energy as hcp-Nb and hcp-Al, respectively. Nb_2Al was described with three sublattices of the stoichiometry $Nb_{16}Al_{10}Nb_4$, where substitutional solution was allowed on the first two sublattices. This compound was described using five independent and two dependent parameters: enthalpy and entropy of formation of the compound without any substitution occurring, enthalpy of formation of the substitutional Al-atom on the Nb-sublattice and enthalpy and entropy of the quasi-regular solution between the regular and substitutional atoms on the Al-sublattice, the enthalpy and entropy of formation of the substitutional Nb-atom were constrained to yield at complete substitution the same Gibbs energy as hcp-Nb. $NbAl_3$ was also modeled with the Wagner-Schottky model, because of its narrow range of homogeneity the thermodynamic quantities of the formation of the substitutional atoms were given a high positive enthalpy of formation. The enthalpy and entropy of formation of the compound without any substitution occurring were adjusted.

For the optimization of the Nb-Al system the phase diagram data of [59Gla, 61Bar, 61Ned, 66Lun, 70Mul, 71Wik, 72Ron] were not used, since they are contradictory to the data of [68Sve, 76Yer, 80Jor, 88Mur], which are in relative good agreement. Enthalpies of formation of the solid compounds are reported by [68Nec, 72Gor, 75Gel] and agrre within the experimental error. The partial Gibbs energy data of [74Mal, 78Nik] were also not used for the optimization because they are in disagreement with the data of [82Shi] who measured also the temperature dependence in a wide composition range. The enthalpies of mixing of the liquid phase reported by [85Sud] were omitted during the optimization, since they showed inconsistency with the phase diagram and the other thermodynamic data. During the first steps of the optimization the partial Gibbs energy data derived from [82Shi] were used. The results of the calculation revealed inconsistencies between these partial Gibbs energies and the phase diagram data, as well as the measured enthalpies of formation of the solid compounds, i.e. the attempt to fit these partial Gibbs energies resulted in significant narrower ranges of homogeneity of (Nb), Nb_3Al and Nb_2Al and the enthalpy of formation of $NbAl_3$ was much more negative than observed in experiments. Attempts to optimize the thermodynamic quantities without the data from [82Shi] resulted in an excellent fit to the phase diagram data, the enthalpies of formation and the partial Gibbs energies from [82Shi] for Al-contents up to 10 at.% Al. For higher Al-contents the calculation indicates, that the vapor pressures observed by [82Shi] are by a factor 2, incresing to a factor of 6 too low with increasing Al-contents, this disagreement could be explained by depletion on the sample surface. The fact that [82Shi] observed the phase boundaries at the correct compositions indicates that their measured vapor pressures could have been diffusion controlled.

Analytical Description of the Nb-Al System

General formula for the Gibbs energy: $G = \sum_i X(x,n)_i * (H_i - S_i * T)$

with: $\sum_l n_j^l = x_j$

The reference state for all phases is liquid Nb and Al.

The lattice stabilities for the pure elements are from Saunders et al. [88Sau].

Coefficients adjusted in the optimization are underlined.

Liquid, Substitutional Solution (Nb,Al)

$X(x,n)_i$	H_i	S_i
x_{Nb}	0.00	0.00000
x_{Al}	0.00	0.00000
$\sum_j x_j * \ln(x_j)$	0.00	-8.31451
$x_{Nb} x_{Al}$	-128849.60	-45.97652
$x_{Nb} x_{Al} * (x_{Nb} - x_{Al})$	24739.30	26.72643
$x_{Nb} x_{Al} * (x_{Nb} - x_{Al})^2$	16853.40	0.00000

bcc (Nb), Substitutional Solution (Nb,Al)

$X(x,n)_i$	H_i	S_i
x_{Nb}	-30000.00	-10.90900
x_{Al}	-628.00	-6.66300
$\sum_j x_j * \ln(x_j)$	0.00	-8.31451
$x_{Nb} x_{Al}$	-128591.50	-44.31129
$x_{Nb} x_{Al} * (x_{Nb} - x_{Al})$	-20593.00	0.00000

fcc (Al), Substitutional Solution (Nb,Al)

$X(x,n)_i$	H_i	S_i
x_{Nb}	-8000.00	-8.70900
x_{Al}	-10711.00	-11.47300
$\sum_j x_j * \ln(x_j)$	0.00	-8.31451
$x_{Nb} x_{Al}$	-182673.40	-95.45734

Nb_3Al, Wagner-Schottky Compound $(Nb,Al)_3(Al,Nb)_1$

$X(x,n)_i$	H_i	S_i	Constraint Factor
x_{Nb}	-13000.00	-9.70900	
x_{Al}	-5230.00	-9.67300	
$\sum_l \sum_j n_j^l * \ln(n_j^l)$	0.00	-8.31451	
1	-44227.10	-7.44578	1.0000
n_{Nb}^2	176908.60	29.78315	-4.0000
n_{Al}^1	58969.50	9.91773	-1.3333
$n_{Nb}^2 * n_{Al}$	-544900.30	-94.69727	

Nb_2Al, Wagner-Schottky Compound $(Nb,Al)_{16}(Al,Nb)_{10}(Nb)_4$

$X(x,n)_i$	H_i	S_i	Constraint Factor
x_{Nb}	-13000.00	-9.70900	
x_{Al}	-5230.00	-9.67300	
$\sum_l \sum_j n_j^l * \ln(n_j^l)$	0.00	-8.31451	
1	-50600.50	-9.57270	1.0000
n_{Nb}^2	151804.10	28.71813	-3.0000
n_{Al}^1	46447.10	0.00000	
$n_{Nb}^2 * n_{Al}$	-232792.90	-37.21113	

$NbAl_3$, Wagner-Schottky Compound Nb_1Al_3

$X(x,n)_i$	H_i	S_i
x_{Nb}	-8000.00	-8.70900
x_{Al}	-10711.00	-11.47300
$\sum_l \sum_j n_j^l * \ln(n_j^l)$	0.00	-8.31451
1	-49298.10	-12.82841
n_{Nb}^2	100000.00	0.00000
n_{Al}^1	300000.00	0.00000

References for Nb-Al

59Gla V.M. Glazov, V.N. Vigdorovich and G.A. Korol'kov, Russ. J. Inorg. Chem. 4 (1959) 730-732

61Bar V.V. Baron and E.M. Saviskii, Russ. J. Inorg. Chem. 6 (1961) 90-92

61Ned N.A. Nedumov and V.I. Rabezove, Izv. Akad. Nauk SSSR, Otd. Tekhn. Nauk, Met. Topl. (4) (1961) 68-70

66Lun C.E. Lundin and A.S. Yamamoto, Trans. AIME 236 (1966) 863-872

68Nec A. Neckel and H. Nowotny, Int. Leichmetalltag., 5th Meeting, 1968, 72-76, Aluminium-Verlag, Duesseldorf, F.R. Germany

68Sve V.N. Svechnikov, V.M. Pan and V.I. Latiesheva, Metallofiz. 2 (1968) 54-61

70Mul A. Mueller, Z. Naturforsch. 25a (1970) 1659-1669

71Wik A. Wicker, C. Allibert and J.Driole, C. R. Acad. Sc. Paris 272 (1971) 1711-1713

72Gor O.S. Gorelkin, A.S. Dubrovin, O.D. Kolesnokova, Yu.Ya. Demidov and N.A. Chirkov, Proizvodstvo Ferrosplavov (Celjabinsk) (1972) 123-137

72Ron G.N. Ronami, Kristall und Technik, 7 (1972) 615-638

74Mal G.A. Malets, Vesti. Akad. Nauk B.SSR, Ser. Khim. Nauk (1974) No.6, 127-129

75Gel G.A. Gelashvili and Zh.I. Dzneladze, Soviet Powder Metall. Crem. 14 (1975) 732-737

76Kok L. Kokot, R. Horyn and N. Iliew, J. Less-Common Met. 44 (2976) 215-219

76Yer V.N. Yeremenko, Ya.V. Natanzon and V.I. Dybkov, J. Less-Common Met. 50 (1976) 29-48

78Nik G.I. Nikolaev and N.V. Bodrov, Russ. J. Phys. Chem. 52 (1978) 821-823

80Jor J.L. Jorda, R. Fluekiger and J. Muller, J. Less-Common Met. 75 (1980) 227-239

82Shi I. Shilo, H.F. Franzen and R.A. Schiffman, J. Electrochem. Soc. 129 1608-1613

85Sud V.S. Sudavstova, G.I. Batalin and V.S. Tutevich, Russ. Metall. (1985) No.5, 183-185

88Mur J.L. Murray, private communication of data from L.A. Willey, 1988

88Sau N. Saunders A.P. Miodownik and A.T. Dinsdale, CALPHAD 12 (1988) 351-374

B. The Nb-Si (Niobium - Silicon) System

The Nb-Si system consists of seven phases:

- The liquid L
- The bcc (Nb) solid solution which dissolves only few Si (up to 1.2 at.% Si at 1920 °C
- The Nb_3Si phase with the tetragonal Ti_3P structure. It forms peritectically from the melt and βNb_5Si_3 at 1940 °C and decomposes eutectoidally into (Nb) and αNb_5Si_3 at 1770 °C
- The αNb_5Si_3 phase with the tetragonal Cr_5B_3 structure and forms peritectoidally from Nb_3Si and βNb_5Si_3 at 1980 °C. Its narrow range of homogeneity extends from 37.5 to 39.5 at.% Si at 1650 °C
- The βNb_5Si_3 phase with the tetragonal W_5Si_3 structure. It forms congruently from the melt at 2520 °C and decomposes eutectoidally into αNb_5Si_3 and $NbSi_2$ at 1650 °C. Its maximum range of homogeneity extends from 37.5 to 40.5 at.% Si at 1900 °C
- The $NbSi_2$ phase with the hexagonal $CrSi_2$ structure. It forms congruently from the melt at 1940 °C
- The dia (Si) with the cubic diamond structure and nil solubility for Nb

The liquidus of the Nb-Si system was determined in two experimental studies, [55Kna] measured pyrometrically the temperature of melting and the accuracy of the temperatures reported is estimated to be greater than ±50 °C. [80Koc] used high temperature DTA and give an accuracy of ±20 °C, these data were used for the evaluated phase diagram (Fig. 8).

Invariant Points of the Assessed Nb-Si Phase Diagram

Reaction	Compositions at.% Si			Temperature °C	Reaction type
L → (Nb) + Nb_3Si	17.5	1.2	25	1920±20	Eutectic
L + βNb_5Si_3 → Nb_3Si	~19	~37.5	25	1980±20	Peritectic
Nb_3Si + βNb_5Si_3 → αNb_5Si_3	25	~37.5	~37.5	1940±20	Peritectoid
Nb_3Si → (Nb) + αNb_5Si_3	25	0.5	37.5	1770±20	Eutectoid
L → βNb_5Si_3 + $NbSi_2$	57	40.5	66.7	1900±20	Eutectic
βNb_5Si_3 → αNb_5Si_3 + $NbSi_2$	39.5	~40	66.7	1650±15	Eutectoid
L → $NbSi_2$ + (Si)	98	66.7	100	1400±10	Eutectic
L → βNb_5Si_3		~37.5		2520±25	Congruent point
L → $NbSi_2$		66.7		1940±20	Congruent point
L → (Nb)		0		2469	Melting point
L → (Si)		100		1414	Melting point

Nb-Si Crystal Structure Data

Phase	Composition at.% Si	Pearson symbol	Space group	Strukturbericht designation	Proto type
(Nb)	0 - 1.2	cI2	In-3m	A2	W
Nb_3Si	25	tP32	$P4_2/n$	...	Ti_3P
αNb_5Si_3	~37.5 - 39.5	tI32	I4/mcm	$D8_l$	Cr_5B_3
βNb_5Si_3	~37.5 - 40.5	tI32	I4/mcm	$D8_m$	W_5Si_3
$NbSi_2$	66.7	hP9	$P6_222$	C40	$CrSi_2$
(Si)	100	cF8	Fd-3m	A4	C

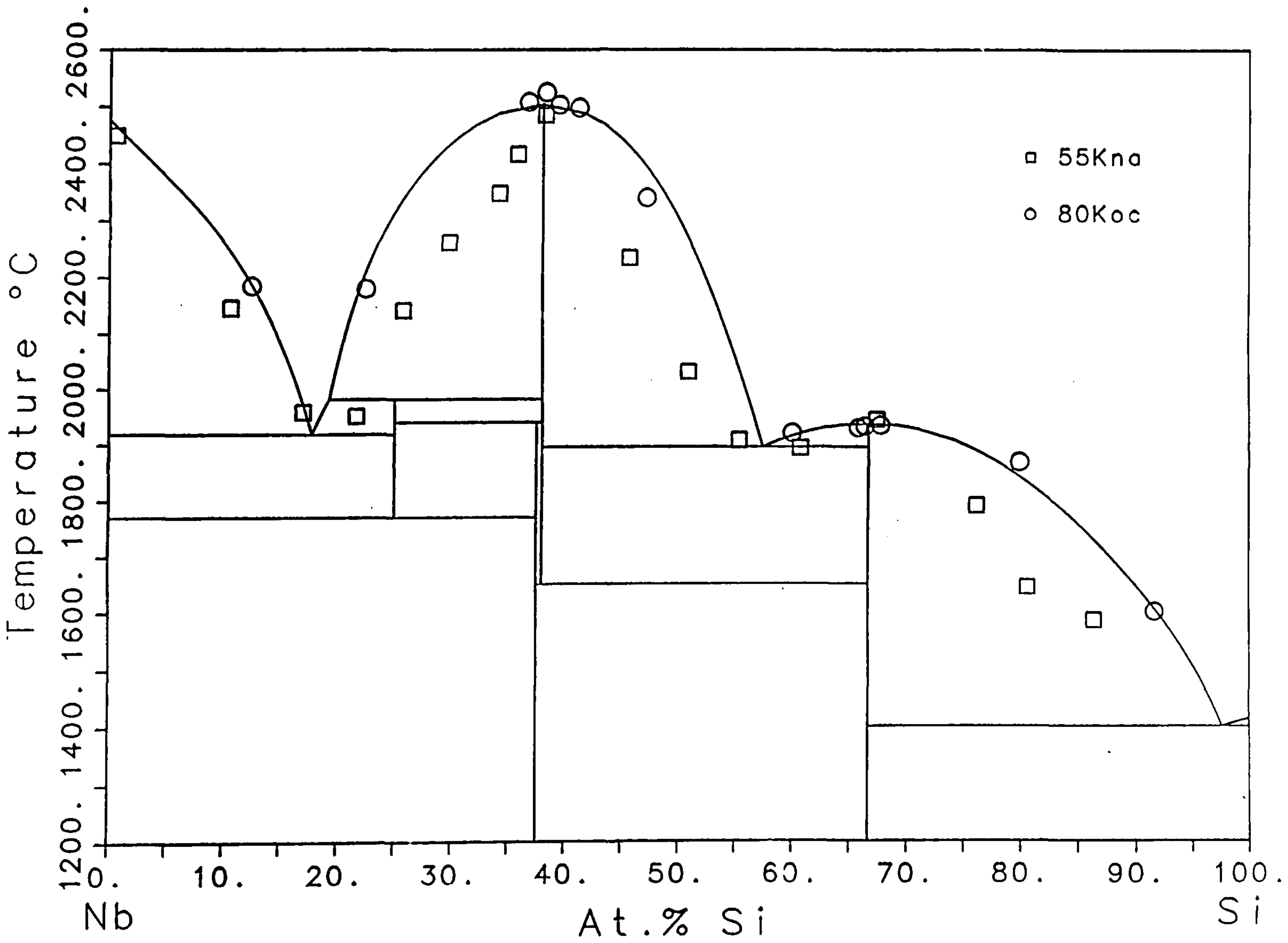

Fig. Calculated and measured phase diagram of the Nb-Si system.

Thermodynamic Modeling of the Nb-Si System

For the calculation of the Nb-Si System the liquid was described using the quasi-subregular model and all the solid phases were assumed to be stoichiometric, since they all reveal no or only very small ranges of homogeneity.

The phase diagram data of [80Koc] and the enthalpies of formation of [72Gor] were used for the least squares optimization of the Nb-Si system. The calculated and the experimental phase diagram agree very well, while the calculated enthalpies of formation of aNb_5Si_3 and $NbSi_2$ differ more the experimental error reported by [72Gor]

Calculated and Measured Enthalpies of Formation at 25 °C

Phase	$\Delta H_{meas.}$ J/mol of atoms	$\Delta H_{calc.}$ J/ mol of atoms
αNb_5Si_3	-63858±11700	-43137
$NbSi_2$	-52000±15000*	-59933

* Enthalpy derived from the value reported for the two-phase equilibrium $\alpha Nb_5Si_3 + NbSi_2$

Analytical Description of the Nb-Si System

General formula for the Gibbs energy: $G = \sum_i X(x,n)_i * (H_i - S_i * T)$

The reference state for all phases is bcc Nb and liquid Si.

The lattice stabilities for the pure elements are from Saunders et al. [88Sau].

Coefficients adjusted in the optimization are underlined.

Liquid, Substitutional Solution (Nb,Si)

$X(x,n)_i$	H_i	S_i
x_{Nb}	30000.00	10.90900
x_{Si}	0.00	0.00000
$\sum_j x_j * \ln(x_j)$	0.00	-8.31451
$x_{Nb} x_{Si}$	$\underline{-197387.10}$	$\underline{-42.33861}$
$x_{Nb} x_{Si} * (x_{Nb} - x_{Si})$	$\underline{-116757.40}$	$\underline{-58.17759}$

(Nb), Stoichiometric Compound Nb_1Si_0

$X(x,n)_i$	H_i	S_i
1	0.00	0.00000

(Si), Stoichiometric Compound Nb_0Si_1

$X(x,n)_i$	H_i	S_i
1	-50208.00	-29.76200

Nb_3Si, Stoichiometric Compound Nb_3Si_1

$X(x,n)_i$	H_i	S_i
1	$\underline{-36991.30}$	$\underline{-5.45877}$

αNb_5Si_3, Stoichiometric Compound Nb_5Si_3

$X(x,n)_i$	H_i	S_i
1	$\underline{-61964.80}$	$\underline{-11.35889}$

βNb_5Si_3, Stoichiometric Compound $Nb_{31}Si_{19}$

$X(x,n)_i$	H_i	S_i
1	$\underline{-58966.70}$	$\underline{-9.78875}$

$NbSi_2$, Stoichiometric Compound Nb_1Si_2

$X(x,n)_i$	H_i	S_i
1	-93405.20	-27.02926

References for Nb-Si

55Kna A.G. Knapton, Nature 175 (1955) 730-730

72Gor O.S. Gorelkin, A.S. Dubrovin, O.D. Kolesnokova, Yu.Ya. Demidov and N.A. Chirkov, Proizvodstvo Ferrosplavov (Celjabinsk) (1972) 123-137

80Koc Yu.A. Kocherzhinskiy, L.M. Yupko and E.A. Shishkin, Russ. Metall. (1980) No.1, 184-188

V. Fiscal Status

Amount provided for contract program

$150,000 for period February 9, 1987 to September 30, 1987.

$200,000 for period October 1, 1987 to September 30, 1988.

$200,000 for period October 1, 1988 to September 30, 1989.

$ 50,000 for period October 1, 1989 to December 31, 1989.

APPENDIX

Materials Science and Engineering, *98* (1988) 265–268

Pathways for Microstructural Development in TiAl*

J. A. GRAVES

Department of Metallurgical and Mineral Engineering, University of Wisconsin, Madison, WI 53706 (U.S.A.)

L. A. BENDERSKY and F. S. BIANCANIELLO

Metallurgy Division, Center for Materials Science, National Bureau of Standards, Gaithersburg, MD 20899 (U.S.A.)

J. H. PEREPEZKO

Department of Metallurgical and Mineral Engineering, University of Wisconsin, Madison, WI 53706 (U.S.A.)

W. J. BOETTINGER

Metallurgy Division, Center for Materials Science, National Bureau of Standards, Gaithersburg, MD 20899 (U.S.A.)

Abstract

Rapid solidification processing (RSP) of intermetallic alloys can provide alternative solidification paths and lead to the formation of metastable products. For the intermetallic TiAl with an equilibrium $L1_0$ *structure, RSP has yielded a metastable hexagonal close packed (h.c.p.)* α*-Ti phase in both fine powder and melt-spun ribbon. Based on transmission electron microscopy observations of a fine antiphase domain structure, the h.c.p. phase orders to the* Ti_3Al *(*DO_{19}*) structure following solidification. A metastable phase diagram analysis indicates that a melt undercooling of about 100 °C is required for partitionless formation of an h.c.p. phase from an equiatomic melt and reveals other possible solidification pathways including the nucleation of metastable disordered body-centered cubic (b.c.c.) and face-centered cubic (f.c.c.) phases. Each of the potential pathways offers further opportunity for microstructural modification by solid-state annealing treatments.*

1. Introduction

Based on the equilibrium phase diagram, the opportunities for the solidification processing of intermetallic compounds appear to be quite limited. With conventional melt processing of intermetallics, one or more peritectic reactions and wide liquidus–solidus separation are encountered and lead to large-scale composition segregation which is difficult to eliminate during post-solidification treatments.

At the same time, the characteristics which make intermetallics unattractive for conventional processing qualify them as suitable candidates for rapid solidification processing (RSP). The high rate of heat extraction and rapid crystal growth rates commonly associated with RSP yield fine-scale microstructures with reduced segregation tendencies or metastable products [1]. Indeed, a recent report on rapid solidification of TiAl alloy powders has demonstrated one of the alternative metastable solidification pathways involving the nucleation of a disordered hexagonal close packed (h.c.p.) α-Ti phase [2]. The current study represents a more detailed examination of RSP microstructures in TiAl.

2. Experimental method

Alloys were arc melted in gettered argon from 99.9% pure components for three compositions: Ti–36wt.%Al, Ti–38wt.%Al and Ti–40wt.%Al. At elevated temperature at equilibrium these alloy compositions should be single-phase TiAl [3]. The composition Ti–38wt.%Al corresponds closely to the break in the liquidus for the peritectic reaction $L + \beta(Ti) \rightarrow TiAl$ at approximately 1480 °C, whereas Ti–40wt.%Al is in the field of primary crystallization of TiAl below approximately 1480 °C.

Ribbons were prepared by melt spinning on a copper wheel in helium. Powders were produced by a rotating electrode process [4] under a helium atmosphere. Ribbon samples were prepared for transmission electron microscopy (TEM) examination by twin-jet electropolishing in a 92% acetic acid and 8% perchloric acid electrolyte at room temperature. Internal sections were etched with Kroll's reagent.

---

*Paper presented at the Sixth International Conference on Rapidly Quenched Metals, Montréal, August 3–7, 1987.

0025-5416/88/$3.50

© Elsevier Sequoia Printed in The Netherlands

3. Results

3.1. Powders

X-ray diffraction analysis of the finest powder size fraction revealed the presence of two crystal structures: the equlibrium TiAl, $L1_0$ phase and a metastable hexagonal structure which was indexed according to the ordered Ti_3Al (DO_{19}) α_2 phase [5]. As shown in Fig. 1, the finest powder predominantly comprised the α_2 phase, with only a minor fraction of the total volume (less than 10%) represented by TiAl. The relative abundance of the two phases varied with powder size, with the metastable product decreasing in amount as the particle size increased. Microstructural examination of the fine powder revealed that approximately 30% of the particles were single phase and the remainder were dual phase. The morphology of the dendritic structure in dual-phase powders, as illustrated in Fig. 2, showed a consistent tendency for primary arms to have a sixfold rotational symmetry, with secondary arms maintaining growth angles of approximately 60° with respect to primary dendrite arms. This growth pattern is indicative of an h.c.p. structure for which the preferred growth directions are of the $\langle 10\bar{1}0 \rangle$ type [6]. Thus, solidification of the finest powder occurred by the formation of an h.c.p. structure from the melt. Droplets which nucleate at reduced undercoolings form an initial single-phase h.c.p. region; however, as recalescence raises the particle temperature, a two-phase structure develops which has a dendritic h.c.p. phase with TiAl in the interdendritic regions. Ordering in the solid state to the α_2 structure can occur as the h.c.p. phase cools.

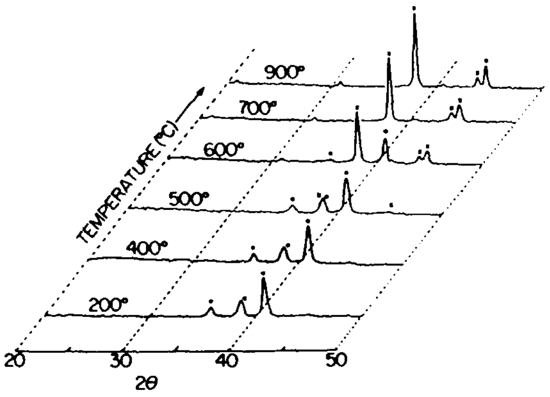

Fig. 1. X-ray diffraction patterns showing decomposition of metastable DO_{19} structure (●) to equilibrium $L1_0$ phase (×) in $-44\ \mu m$ powder during step-scan annealing at indicated temperatures.

3.2. Ribbons

The as-solidified microstructures of the Ti–38wt.%Al and Ti–40wt.%Al alloys after melt spinning are very similar and can be seen in Fig. 3. The dark regions tend to be convex, suggesting that this phase forms from the melt first, and share a common crystallographic orientation. These regions were identified as the hexagonal DO_{19} structure by convergent beam electron diffraction (CBED) as shown in Fig. 4(a), whereas the phase shown in light contrast in Fig. 3 is identified in Fig. 4(b) *as having the tetragonal* $L1_0$ (TiAl) structure. The DO_{19} phase contains a fine distribution of antiphase domains which are shown in dark field in Fig. 5 using a superlattice reflection. These fine antiphase domains indicate that the DO_{19} order was established in the solid state from a disor-

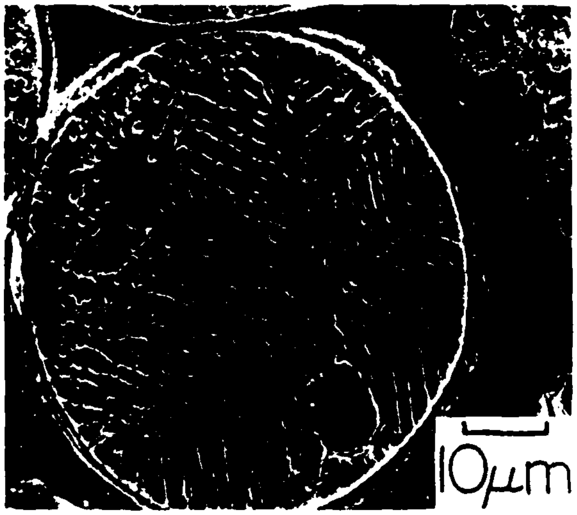

Fig. 2. Ti 36wt.%Al particle showing h.c.p. growth morphology.

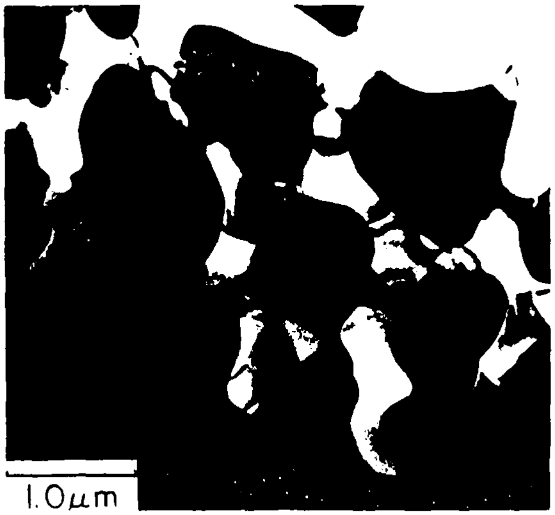

Fig. 3. As-solidified microstructure of Ti-40wt.%Al melt-spun ribbon.

the α_2–γ transformation interface and is consistent with the relatively wide temperature range for the decomposition of α_2 in TiAl.

4. Discussion

The microstructural development that has been observed following rapid solidification of TiAl alloys identifies one metastable pathway for processing reactions. For both melt-spun ribbon and powder, the pathway begins with the solidification of disordered h.c.p. α-Ti phase from an undercooled liquid, with the interdendritic regions solidifying as an $L1_0$ TiAl phase. Rapid solid-state transformations change the h.c.p. into the DO_{19} structure during quenching. Because the DO_{19} is supersaturated with respect to the $L1_0$ phase, solid-state decomposition proceeds with the DO_{19} phase transforming into a mixture of alternating, parallel plates of DO_{19} and $L1_0$ phases and by thickening of the plates to a single-phase $L1_0$.

In evaluating potential rapid solidification pathways and phase selection, metastable phase diagrams and the relevant T_0 curves provide valuable guidance [9, 10]. For the Ti–Al alloy system, T_0 curves can be calculated using thermodynamic data supplied by Murray [3] for the body-centered cubic (b.c.c.) and h.c.p. product structures, as illustrated in Fig. 7. Based on these T_0 curves, an equiatomic alloy would require an undercooling of only about 100 °C to provide a driving force for formation of the h.c.p. solid from the melt. It is interesting to note, however, that at the equiatomic composition the $L1_0$ and b.c.c. solids have T_0 temperatures above that of the h.c.p. phase. This indicates the importance of kinetics in controlling product phase selection in an undercooled melt. As the aluminum content is increased beyond the equiatomic composition, either f.c.c.-based ordered phases or a disordered f.c.c. phase can become more favored among the metastable products from a driving force (*i.e.* undercooling) standpoint. A complete analysis of alternative solidification pathways [11] would include other product structures involving both disordered and ordered phases such as a CsCl ordered structure. Overall, it is clear that rapid solidification can offer several intriguing microstructural options different from conventional casting for the processing of high temperature ordered intermetallic alloys.

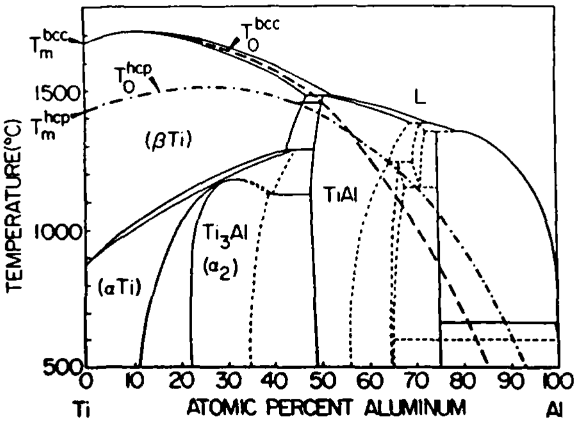

Fig. 7. Ti–Al phase diagram showing equilibrium phase fields and calculated T_0 curve estimates for b.c.c. and h.c.p. structures [3].

Acknowledgment

The support of ARO (DAAL03-86-K-0164) and DARPA/URI (N0014-86-K-0753/P.O. VB38640-0) for JAG and JHP and DARPA (6065) for LAB, FSB and WJB for the study of intermetallic compounds is gratefully acknowledged.

References

1 C. C. Koch, *Mater. Res. Soc. Symp. Proc., 39* (1985) 397.
2 J. A. Graves, J. H. Perepezko, C. H. Ward and F. H. Froes, *Scr. Metall., 21* (1987) 567.
3 J. L. Murray, submitted to *Metall. Trans.*
4 E. J. Kosinski, in J. G. Bewley and S. W. McGee (eds.), *Progress in Powder Metallurgy*, Vol. 38, MPIF–APMI, Princeton, NJ, 1982, p. 491.
5 A. J. Goldak and J. G. Parr, *Trans. Metall. Soc. AIME, 221* (1961) 639.
6 B. Chalmers, *Principles of Solidification*, Wiley, New York, 1964, p. 117.
7 E. Votava, *Acta Metall., 8* (1960) 901.
8 M. J. Blackburn, in R. J. Jaffee and N. E. Promisel (eds.), *The Science, Technology and Application of Titanium*, Pergamon, Edinburgh, 1970, p. 633.
9 J. H. Perepezko and W. J. Boettinger, *Mater. Res. Soc. Symp. Proc., 19* (1983) 223.
10 W. J. Boettinger and J. H. Perepezko, in S. K. Das, B. H. Kear and C. M. Adam (eds.), *Rapidly Solidified Crystalline Alloys*, TMS–AIME, Warrendale, PA, 1985, p. 21.
11 L. A. Bendersky, J. A. Graves, J. H. Perepezko and W. J. Boettinger, to be published.

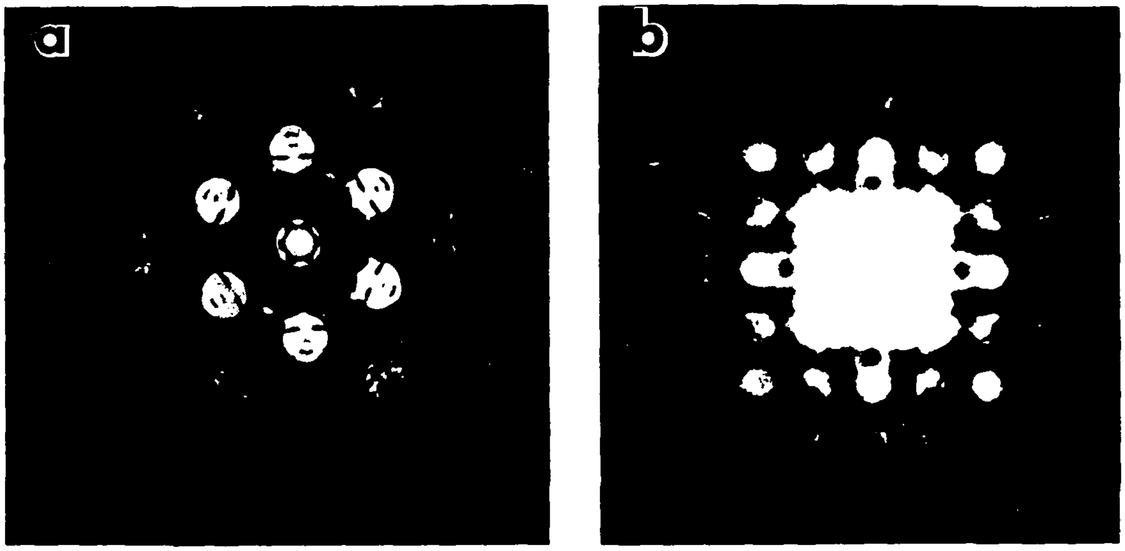

Fig. 4. CBED patterns identifying the (a) [0001] zone axis of the DO_{19} structure and (b) [001] zone axis of the $L1_0$ structure in Ti 40wt.%Al melt-spun ribbon.

dered h.c.p. phase originally produced from the melt, which is consistent with the observations of dendrite morphology in powders.

3.3. Thermal stability

To assess the thermal stability of the metastable α_2 structure, the finest powder for the Ti-36wt.%Al alloy was subjected to a controlled heating cycle during X-ray diffraction under a helium atmosphere (Fig. 1). Significant decomposition of the metastable α_2 phase begins at temperatures above 500 °C, with the transformation to TiAl being completed at approximately 700 °C. The microstructural changes during decomposition that are illustrated in Fig. 6 revealed a plate-like morphology within the α_2 phase consisting of alternating parallel plates of α_2 and TiAl. In some regions of the as-solidified ribbons, the DO_{19} phase has begun to decompose by the same mechanism. With continued annealing, the TiAl plates thicken at the expense of α_2. This pattern resembles very closely the microstructural morphology that develops in cobalt during the face-centered cubic (f.c.c.) ⇆ h.c.p. transformation [7]. Indeed, from TEM analysis the orientation relationship between the phases confirms that reported by Blackburn [8] as

$$(0001)_{DO_{19}} \| (111)_{L1_0}$$

$$[2\bar{1}\bar{1}0]_{DO_{19}} \| \langle 110 \rangle_{L1_0}$$

so that the decomposition of α_2 to TiAl represents the ordered phase counterpart to the allotropic transformation in cobalt. The observed crystallography indicates a low index relationship and a low mobility for

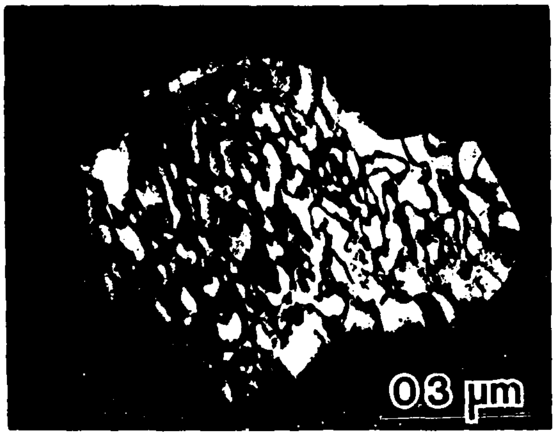

Fig. 5. Dark field image of the DO_{19} phase using a superlattice reflection. The fine antiphase domains can be seen.

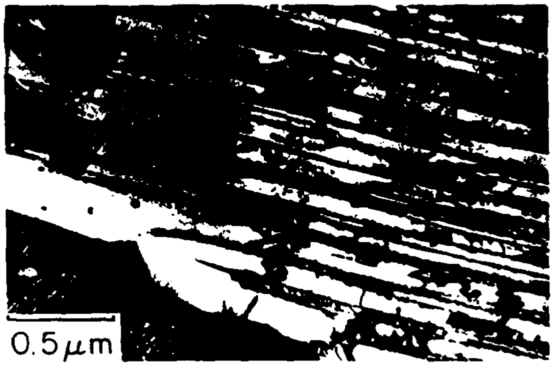

Fig. 6. Alternating plate structure of DO_{19} and $L1_0$ phases in melt-spun Ti-40wt.%Al ribbon.

Materials Science and Engineering, 98 (1988) 273–276

Rapid Solidification and Ordering of B2 and L2$_1$ Phases in the NiAl–NiTi System*

W. J. BOETTINGER, L. A. BENDERSKY, F. S. BIANCANIELLO and J. W. CAHN

Institute for Materials Science and Engineering, National Bureau of Standards, Gaithersburg, MD 20899 (U.S.A.)

Abstract

Evidence is presented for the direct solidification of the B2 phase in the NiAl–NiTi system at some compositions where the L2$_1$ phase is stable at the melting point. Subsequent continuous ordering produces the equilibrium phase. The metastable continuous ordering curve is used to discuss this result.

1. Introduction

Rapid solidification of intermetallic compounds may result in a reduction in microsegregation, an extension of solubility and a manipulation of long-range order or antiphase domain (APD) size. The mechanisms responsible for observed variations in the domain size [1–3] are not well understood. The microstructural modifications made possible by rapid solidification can permit the development of new and unusual two-phase structures during subsequent heat treatment.

Many technologically important ordered phases are closely related to disordered cubic or hexagonal structures which also occur in the same system. This crystallographic relationship between phases has important implications for the thermodynamics of these phases and the mechanisms of phase formation that must be considered to determine the various options which are available during processing.

In the present paper we report the microstructure of melt-spun alloys with compositions between the B2 phases, NiAl and NiTi. This system was chosen for study because of the existence of a ternary Heusler phase based on the ideal composition Ni_2TiAl (NiAl·NiTi) [4]. Its crystal structure, L2$_1$ (identical to DO$_3$), is an ordered form of the B2 structure. Although the solid state B2-to-L2$_1$ transformation satisfies the Landau rules for an allowable higher order transition, the system contains a pair of two-phase fields, NiAl plus Ni_2TiAl and Ni_2TiAl plus NiTi [4–6], indicating that the transition is first order at those temperatures. These two-phase fields permit the study of solubility extension by rapid solidification and an exploration of non-equilibrium ordered states and reaction paths.

2. Experimental procedure

Alloys were prepared by the arc melting of 99.99% pure components. All alloys contained 50 at.% Ni and the following titanium contents (in atomic per cent) with the balance being aluminum: 7.5, 12.5, 15, 17.5, 20, 25, 37.5 and 45. Arc-melted ingots were examined by standard optical metallography and by scanning electron microscopy. Rapidly solidified samples were prepared by melt spinning in helium on a copper wheel. Transmission electron microscopy (TEM) samples were prepared by twin-jet electropolishing in 8% perchloric acid in acetic acid at room temperature.

3. Phase diagram

Kaufman and Nesor [7] calculated the Ni–Al–Ti ternary phase diagram assuming the Heusler phase was a line compound. Nash and Liang [6] give an isothermal section at 900 °C showing a significant solubility range for Ni_2TiAl and a liquidus projection. According to the calculation of Kaufman and Nesor, only the region between NiTi and Ni_2TiAl is quasi-binary (this section contains all tie lines). The liquidus of Nash and Liang implies that only the region between NiAl and Ni_2TiAl is quasi-binary.

4. Results

4.1. *Arc-melted samples*

Of particular interest for the interpretation of the rapid solidification results are the character of the invariant reactions (eutectic or peritectic) and the equilibrium solubility limits of the NiAl, Ni_2AlTi and NiTi phases. Microprobe and TEM analysis was used

---

*Paper presented at the Sixth International Conference on Rapidly Quenched Metals, Montréal, August 3–7, 1987.

0025-5416/88/$3.50

© Elsevier Sequoia/Printed in The Netherlands

TABLE 1 **Phases present in arc-melted samples**

Alloy composition (at.% Ti)	*Primary phase*	*Secondary phase*
7.5	NiAl	Heusler
12.5	NiAl	Heusler
15	NiAl	Heusler
17.5	Heusler	Not determined
20	Heusler	NiAl
25	Heusler	Not determined
37.5	Heusler	NiTi, $NiTi_2$
45	NiTi	Not determined

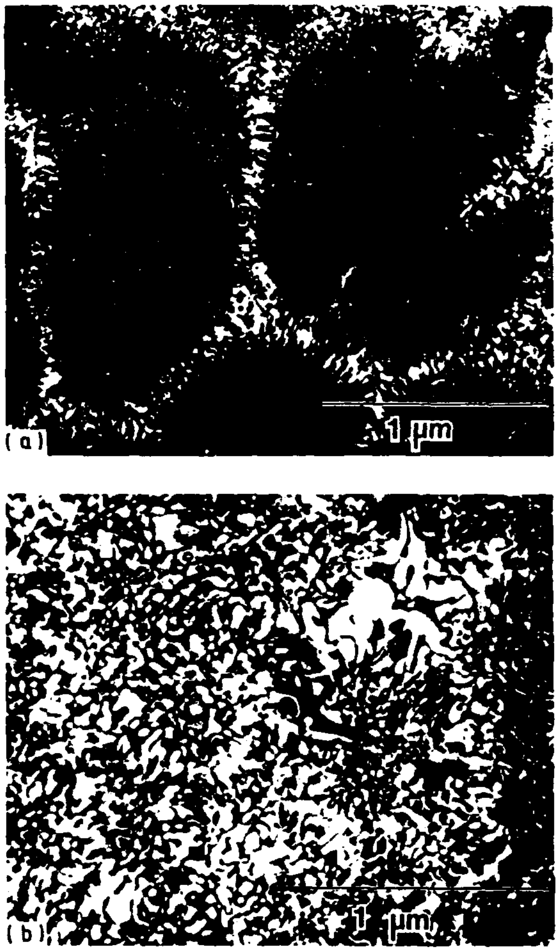

Fig. 1. Dark field transmission electron micrographs using the $L2_1(111)$ superlattice reflection for melt-spun ribbons of (a) Ni-12.5at.%Ti-37.5at.%Al and (b) Ni-17.5at.%Ti-32.5at.%Al.

to determine the primary and secondary phases in the arc-melted samples. These results are summarized in Table 1. Microprobe results were also interpreted to give the solid solubility limits of the phases near their respective invariants: NiAl, 0-11 at.% Ti; Ni_2TiAl, 18-29 at.% Ti; NiTi, 42-50 at.% Ti. Our results are consistent with the notion of a quasi-binary region, except at high titanium contents where we found $NiTi_2$.

4.2. *Ribbons*

The microstructure of the ribbons generally consists of columnar grains with diameters between 1 and 5 μm which extend across the ribbons. Figure 1(a) shows a non-uniform cored structure within a grain in a 12.5 at.% Ti alloy. The centers have the B2 structure, are low in titanium and contain fine $L2_1$ precipitates; the outsides have the $L2_1$ structure, are high in titanium and contain fine APDs. A 7.5 at.% Ti alloy is similar except that the centers are free of precipitates. This non-uniform structure is the result of cellular solidification and the resulting microsegregation of titanium to the cell boundaries expected for the crystallization of NiAl according to the phase diagram to be described below. Alloys containing 17.5 at.% Ti sometimes contained cells with similar segregation but also appeared with a relatively uniform APD size as shown in Fig. 1(b).

In alloys with intermediate levels of titanium (20 and 25 at.%) the structure is $L2_1$ with no cells but with a significantly larger APD size (Fig. 2(a)). At 37.5 at.% Ti the microstructure again consists of $L2_1$ grains but with a much smaller domain size (Fig. 2(b)). A ribbon with 45 at.% Ti contained grains of the B2 phase without any APDs.

The displacement *u* associated with the antiphase boundaries (APBs) was determined. In the B2 structure *u* can only be along [111] whereas in the $L2_1$ phase *u* can also be along [100]. Only [100] boundaries were found. The B2 regions and the $L2_1$ regions were free of [111] boundaries. Where $L2_1$ regions with *fine* domains occur, we infer that the B2 phase formed from the melt, with the [100] APBs forming during solid state ordering to the $L2_1$ phase. Samples free of APBs are likely to result from direct solidification of the $L2_1$ phase. The coarse domains found in the 20 and 25 at.% alloys could have resulted either from direct solidification of $L2_1$ or from such a high temperature ordering of the B2 phase that much domain growth occurred during the quench.

5. Discussion

The results from the arc-melted buttons as well as preliminary thermal analysis were used to estimate the quasi-binary diagram in Fig. 3, even though we have some evidence of segregation outside the quasi-binary region. The ribbon results indicate that rapid solidification increases the metastable range of compositions over which the B2 phase solidified directly from the

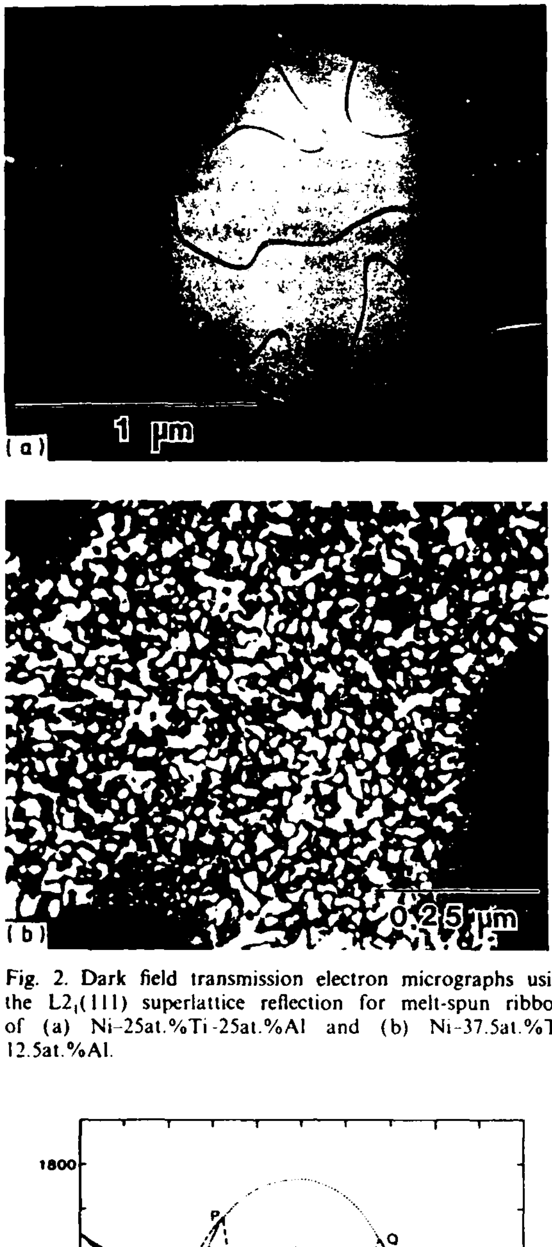

Fig. 2. Dark field transmission electron micrographs using the L2$_1$(111) superlattice reflection for melt-spun ribbons of (a) Ni–25at.%Ti–25at.%Al and (b) Ni–37.5at.%Ti–12.5at.%Al.

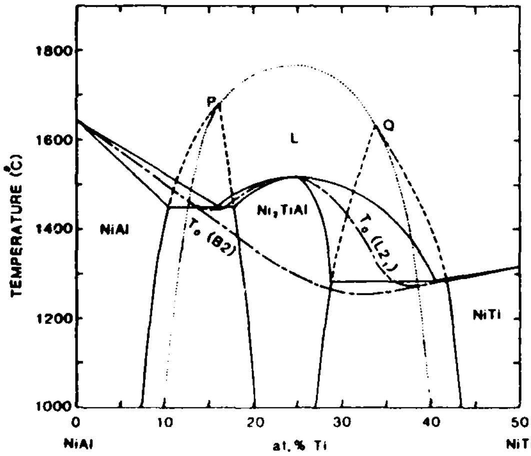

Fig. 3. Estimated equilibrium phase diagram (— — - -) for the NiAl–NiTi quasi-binary system with schematic metastable boundaries and liquid–solid T_0 curves: , metastable extensions of the L2$_1$ plus B2 two-phase fields (points P and Q are the tricritical points); · · ·, the B2 → L2$_1$ continuous ordering curve; - , the T_0 curves.

melt to include compositions where the L2$_1$ phase is the equilibrium phase at the melting point. The formation of the more disordered phase by rapid solidification in a system of this type is surprising and requires further study.

Figure 3 includes curves for the metastable extensions of the B2 plus L2$_1$ two-phase fields above the liquidus and a curve for continuous ordering without a composition change. Such continuous ordering requires only short-range diffusion and should be fast compared with all other solid state diffusional processes. The reader should refer to Allen and Cahn [8] for a full discussion of continuous ordering within a two-phase field. One of the important questions in the present work is whether this line also defines which solid phase forms directly from the melt. With our present knowledge of the phase diagram, very little is known about the location of this curve, but it must be confined within the stable and metastable two-phase fields. The 17.5 at.% Ti composition should be clearly on the L2$_1$ side at all temperatures where solid is stable. Therefore the observation of a fine domain size in a non-cellular region of the 17.5 at.% ribbons seems to indicate a solidification to B2 under conditions where L2$_1$ had to be the more stable phase, followed by subsequent ordering to L2$_1$. A similar situation may occur for the 37.5 at.% Ti alloy.

In the study of the NiAl–Cr eutectic, rapid solidification produced the ordered B2 phase instead of the disordered b.c.c. phase [9]. The metastable construction using a tricritical point to locate the continuous ordering curve had indicated that the metastable range of the ordered phase should expand much more than that of the b.c.c. phase. The construction for the NiAl–NiTi system is depicted in Fig. 3. The T_0 curve for the partitionless solidification of L2$_1$ terminates at the two points where it intersects the continuous ordering curves. In between, T_0 for the L2$_1$ phase lies everywhere at a higher temperature than the T_0 curve for solidification to B2. In this range of compositions during cooling, direct partitionless solidification to L2$_1$ becomes thermodynamically possible before it becomes possible to form B2 without partitioning. However, in the 17.5 and 37.5 at.% Ti alloys, as judged by the fine domains, B2 forms by partitionless solidification rather than L2$_1$ even though B2 requires greater undercooling.

For the alloys containing 7.5 and 12.5 at.% Ti, the centers of the cells have lower titanium contents. Thus in the 7.5 at.% alloy after quenching to room temperature these centers may lie in the single-phase NiAl region and can be retained. For the 12.5 at.% Ti alloy, the cell centers probably have somewhat higher titanium levels and may fall just within the equilibrium NiAl plus Ni_2TiAl two-phase field but outside the ordering curve after quenching. Thus decomposition of the B2 phase must occur by nucleation and growth of $L2_1$ precipitates, causing the fine $L2_1$ particles in the cell centers in Fig. 2(b).

Acknowledgments

We thank C. Brady and A. Shapiro for analysis of the cast samples, R. S. Polvani for providing the aluminum-rich samples and B. Burton for helpful discussions. The support of the Defense Advanced Project Research Agency is appreciated.

References

1 A. Inoue, T. Masumoto, H. Tomioka and N. Yano, *Int. J. Rapid Solidification*, *1* (1984) 115.

2 C. C. Huang, E. L. Hall, K. M. Chang and R. P. Laforce, *Metall. Trans. A*, *17* (1986) 1685.

3 C. C. Koch, J. A. Horton, C. T. Liu, O. B. Cavin and J. O. Scarbrough, in R. Mehrabian (ed.), *Rapid Solidification Processing: Principles and Technologies*, Vol. 3, National Bureau of Standards, Washington, DC, 1982, p. 264.

4 A. Taylor and R. W. Floyd, *J. Inst. Met.*, *80* (1952–1953) 25.

5 R. S. Polvani, W. S. Tzeng and P. R. Strutt, *Metall. Trans. A*, *7* (1976) 33.

6 P. Nash and W. W. Liang, *Metall. Trans. A*, *16* (1985) 319.

7 L. Kaufman and H. Nesor, *Metall. Trans.*, *5* (1974) 1623.

8 S. M. Allen and J. W. Cahn, *Acta Metall.*, *24* (1976) 425.

9 W. J. Boettinger, D. Shechtman, T. Z. Kattamis and F. S. Biancaniello, *Acta Metall.*, *32* (1984) 749.

Scripta METALLURGICA Vol. 22, pp. 1029-1034, 1988 Pergamon Press plc
Printed in the U.S.A.

THE ROLE OF ELASTIC ENERGY IN THE MORPHOLOGICAL DEVELOPMENT OF A Ni-Ti-Al ALLOY

L. A. Bendersky, P. W. Voorhees[*], W. J. Boettinger, and W. C. Johnson[#]
Metallurgy Division, National Bureau of Standards, Gaithersburg, MD 20899
[*]Department of Materials Science and Engineering, Northwestern University, Evanston, IL 60201
[#]Department of Metallurgical Engineering and Materials Science, Carnegie-Mellon University, Pittsburgh, PA 15213-3890

(Received February 26, 1988)
(Revised April 21, 1988)

Introduction

Recently there has been renewed interest in the development of alloys based on intermetallic phases. One approach is to develop alloy systems consisting of two ordered phases (1). The processing of these systems necessary to obtain optimum microstructures requires an understanding of phase instabilities involving both order parameter and composition (2) as well as the coarsening behavior of these two-phase mixtures.

In this paper we describe the late-stage microstructural development of a rapidly solidified $Ni_{50}Al_{12.5}Ti_{37.5}$ alloy. Under ordinary processing conditions this alloy contains nearly equal volume fractions of a Ti-rich B2 phase based on NiTi and a Heusler ($L2_1$) phase based on Ni_2TiAl (3). Following melt spinning the alloy is essentially metastable single phase Heusler, except for the possibility of the antiphase domain boundaries (APB's) being wet by a thin layer of the B2 phase (4). During heat treatment, the isotropic APB structure disappears and is replaced by an array of cuboidal precipitates of the Heusler phase in the B2 matrix. At very long aging times, the formerly distinct precipitates disappear and an isotropic interconnected structure appears. The appearance of the highly interconnected structure is linked to the nearly equal volume fractions of each phase and the loss of coherence at the Heusler-B2 interface. The change in microstructure associated with loss of coherence indicates that the transformation sequence is strongly influenced by stress. The lattice parameter difference between the B2 and Heusler phases (~1.6%) introduces large elastic strains when the system is coherent. We suggest that the effects of elastic energy can dominate the effects of interfacial energy and determine the precipitate shape, and that the elastic interaction energy between precipitates leads to the aligned structures. These elastically driven effects are reduced as the system loses coherency. We believe that the evolution of microstructure in this system can be understood on the basis of these strain effects.

Experimental Procedure

The alloy was prepared by arc melting 99.99% pure components. Rapidly solidified samples were prepared by melt spinning in a He atmosphere on a Cu wheel. The evolution of the microstructure was studied by heat treating samples at 800°C for 10 min., 1 h, 10 h, and 100 h. TEM samples were prepared by twin jet electropolishing in 8% perchloric in acetic acid at room temperature.

The analyzed microstructures are either the Heusler ($L2_1$) phase with APB's or a mixture of Heusler and B2, with a common cubic lattice. Therefore imaging of microstructural detail is possible only in dark-field with a superlattice reflection. For imaging the Heusler phase and its APB's, we used the 111_H reflection at a foil orientation close to the <011> zone axis. For imaging the B2 phase, we used the 100_{B2} reflection (almost overlapping with 200_H) at a foil orientation close to the [100] zone axis. Even though both reflections operate in dark-field imaging, the unexpected stronger scattering factor for 100_{B2} enabled us to image the B2 phase clearly.

In the following discussion, the results are analyzed in terms of a quasibinary NiTi-Ni_2TiAl phase diagram (tie lines lie in the section). However, this is not completely correct since in addition to major transitions involving B2 and $L2_1$, a small fraction of grain boundary and volume precipitation of a third phase was also observed. Also, both B2 and Heusler phases have additional diffuse scattering localized at (110_H), similar to that observed in CuMnAl alloys (5). These effects will be discussed elsewhere since they do not

0036-9748/88 $3.00 + .00

affect the major conclusions of this work.

Results and Discussion

The microstructure of the as-solidified melt-spun ribbon consists of 1-2 μm diameter columnar grains of an essentially single-phase Heusler structure. This is to be contrasted with arc melted buttons which are two phase (4). Figure 1 shows a typical grain where a relatively large density of antiphase domain boundaries is imaged. The boundaries are basically isotropic, although observation of foils at <001> zone axis orientation shows some alignment of APB's along {100} planes with signs of possible wetting by the B2 phase.

After annealing for 10 min. at 800°C, the Heusler phase decomposes into the two-phase structure shown in Figure 2. The alignment of the B2 phase along the elastically soft <100> directions is clear. The structure is most likely a result of chemical spinodal *decomposition of the s*upersaturated Heusler phase into Al-rich regions and Ti-rich regions, with a characteristic wavelength of ~10 nm. The Ti-rich regions subsequently continuously disorder into the B2 structure in a manner similar to that described by Allen and Cahn [2]. Consistent with a spinodal decomposition process is the interconnectedness of the microstructure and the absence of readily identifiable "matrix" and "precipitate" phases. In addition, the interfaces between the precipitates and matrix appear diffuse, in contrast to those seen in long time anneals. The alignment of the structure is due to an orientational dependence of the elastic energy of the spinodal waves. This orientational dependence results in composition waves along the elastically soft <100> crystallographic directions (6).

The microstructure after a one hour anneal at 800°C is shown in Figure 3. In contrast to the microstructure shown in Figure 2, the precipitate and matrix phases are now readily identifiable as the Heusler and B2 phases, respectively, (using additional observation in a <011> zone axis orientation). We believe that the elastic field generated by the large precipitate-matrix misfit contributes to both the cuboidal morphology of the individual precipitates and the crystallographic alignment of the precipitates. A misfitting precipitate with a cuboidal morphology may possess a lower total energy than an ellipsoid when elastic effects are included even when the interfacial energy is isotropic (7). This view is reinforced when later we see the loss of the cuboidal morphology when the strain fields are relaxed. The elastic interaction between precipitates can also strongly affect the spatial distribution of the precipitates. Elastic energy calculations of cubes in isotropic media with different elastic constants than the matrix (7) and cubes in anisotropic media with the same elastic constants as the matrix (8) show that the elastic interaction energy between misfitting cuboids results in *an effective force which is attractive at long* distances and repulsive at short distances. As a result, the cubes tend to align face to *face with a small distance of separation* and do not coalesce. It is the repulsive force which is a result of the elastic interaction that prevents the cubes from touching. That the *system* is largely coherent is substantiated by Figure 4 where the widely spaced bulk dislocations are imaged in weak beam dark field with the fundamental 400_H reflection. There is no evidence of interface dislocations associated with a semi-coherent interface.

Aging for 10 hours at 800°C produces no radical change in the microstructure, other than an increase in the size of the precipitates. As shown in Figure 5, the cubes are still aligned along the crystallographically soft directions with small interparticle separations. However, there has been a change in the structure of the two-phase interface. Figure 6 shows a square net of interfacial dislocations. The dislocations are of edge type with Burgers vector $1/2a_o^H\{100\}$. *The dislocation spacing, about 35 nm, is not enough to accommodate the* misfit. Thus, despite the loss of coherency, the elastic energy is still sufficient to *maintain the cuboidal morphology of the precipitates and the alignment* of the individual precipitates.

Figure 7 shows the microstructure after 100 hours of aging. The aligned microstructure of cuboidal precipitates has disappeared entirely and an isotropic, interconnected microstructure has appeared. The cause of the microstructural change is related to the relaxation of the misfit strains by interfacial dislocations. This is illustrated in Figure 8 using dark-field weak-beam imaging to show the interphase structure. Clearly evident is the square network of interfacial dislocations of the $1/2a_o^H<100>$ edge type with a spacing of about 20 nm. This spacing of interfacial dislocations is sufficient to relax most of the misfit strain. Thus, the elastic interaction between the precipitates is now negligible and the raft-like arrangement of the precipitates is destabilized. As there is little barrier to coalescence, since the ordered nature of the phases implies that the touching of two Heusler precipitates will result in the presence of a low energy APB only 50% of the time, an interconnected structure results which is characteristic of two phases with approximately equal volume fractions. The isotropy of the observed interconnected structure is likely a result of the nearly isotropic interfacial energy in this system.

We believe that these micrographs present conclusive evidence that the elastic strain energy is important in determining the morphological evolution in this system.

Acknowledgements

PWV and WCJ acknowledge the support of the Office of Naval Research under contract number NOOK1-85-F-0066 and LB and WJB acknowledge the support of the Defense Advanced Research Projects Agency under order number 6065.

References

1. R. S. Polvani, W. S. Tzeng and P. R. Strutt, Met. Trans. 7A (1976) 33.
2. S. M. Allen and J. W. Cahn, Acta Met. 24 (1976) 425.
3. A. Taylor and P. W. Floyd, J. Inst. Metals 80 (1952-3) 25.
4. W. J. Boettinger, L. A. Bendersky, F. S. Biancaniello and J. W. Cahn, Mats. Sci. and Eng. (in press).
5. M. Bouchard and G. Thomas, Acta Met., 23, 1485 (1975).
6. J. W. Cahn, Trans. TMS-AIME, 242, 166 (1968).
7. William C. Johnson and P. W. Voorhees, J. Appl. Phys. 61, 1610 (1987).
8. A. G. Khachaturyan, S. V. Semenovskaya and J. W. Morris, Jr., Center for Advanced Materials Report, LBL, preprint #22472 (1986).

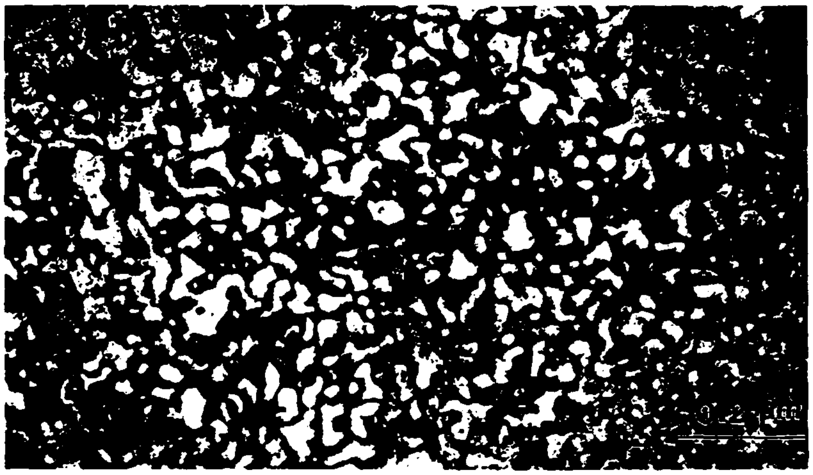

Figure 1. 111_H dark-field micrograph of the as-solidified melt spun alloy showing relatively isotropic orientation of 1/2 a$<100>_H$ APB's of the Heusler phase.

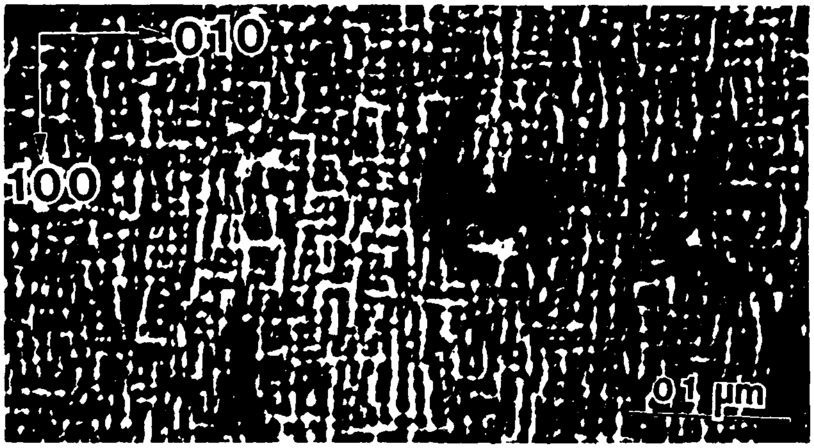

Figure 2. $200_H/100_{B2}$ dark-field micrograph of the alloy annealed for 10 min. at 800°C showing anisotropic modulation of the precipitated B2 phase (white contrast) and the Heusler phase along <100> directions.

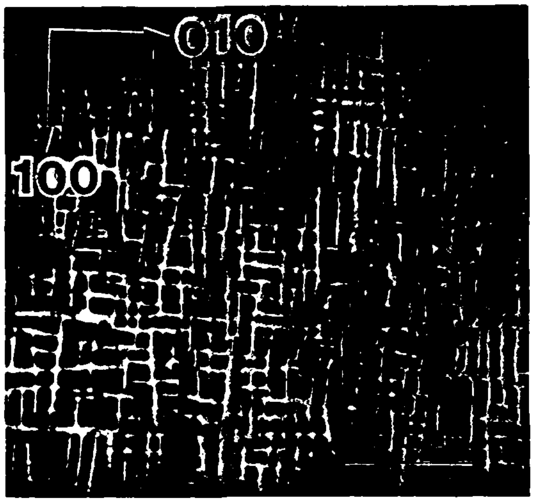

Figure 3. $200_H/100_{B2}$ dark-field micrograph of the 1 h annealed alloy showing interconnected B2 phase (matrix) and cuboidal particles of the Heusler phase.

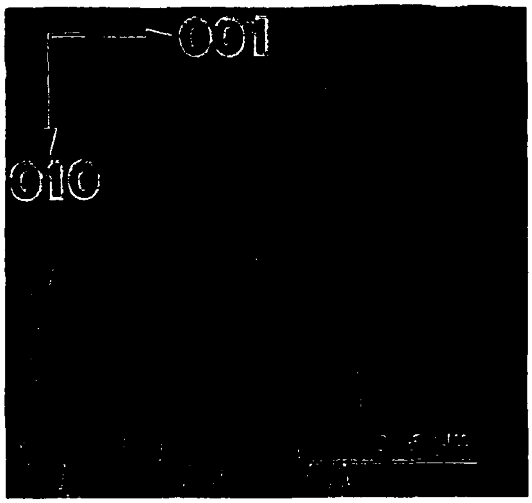

Figure 4. Weak-beam dark-field micrograph (004_H fundamental reflection) showing only bulk dislocations and no stress-accommodating dislocations. Same specimen as Figure 3.

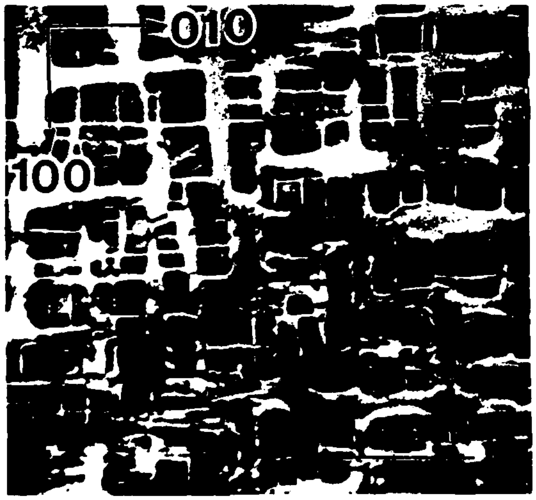

Figure 5. $200_H/100_{B2}$ dark-field micrograph of the 10 h annealed alloy showing essentially the same microstructure as for 1 h (Figure 3).

Figure 6. Bright-field image showing square net of interfacial dislocations in the alloy annealed for 10 h.

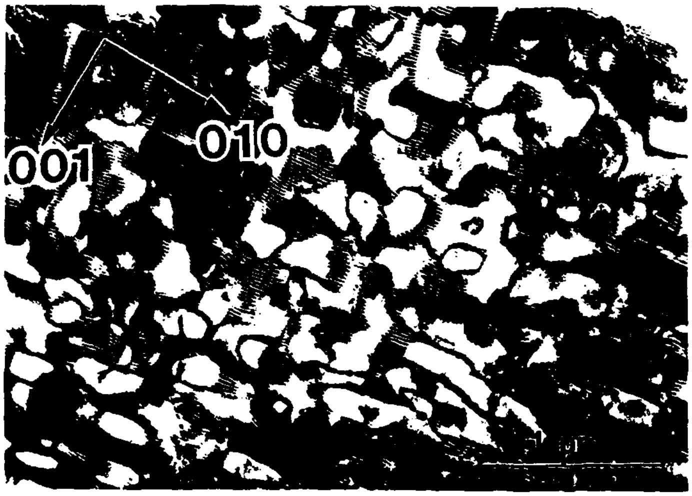

Figure 7. Dark-field micrograph (with $002_B/001_{B2}$ reflection) showing the almost isotropic two-phase interconnected structure, after 100 h annealing.

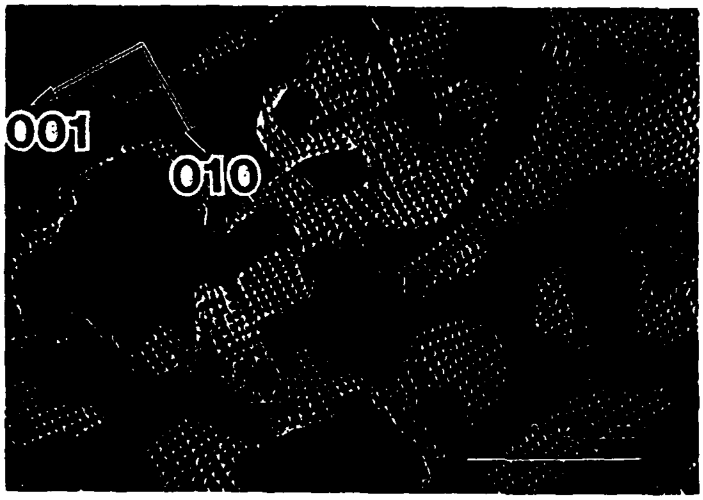

Figure 8. Weak-beam dark-field image of interfacial dislocations (b = a/2 <001>) with spacing small enough to reduce greatly misfit strain. Same sample as Figure 7.

Acta metall. Vol. 37, No. 12, pp. 3379–3391, 1989
Printed in Great Britain

0001-6160/89 $3.00 + 0.00
Pergamon Press plc

THEORY FOR THE TRAPPING OF DISORDER AND SOLUTE IN INTERMETALLIC PHASES BY RAPID SOLIDIFICATION

W. J. BOETTINGER[1] and M. J. AZIZ[2]

[1]Metallurgy Division, National Institute of Standards and Technology, (formerly National Bureau of Standards), Gaithersburg, MD 20899, and [2]Division of Applied Sciences, Harvard University, Cambridge, MA 02138, U.S.A.

(*Received* 15 *March* 1989)

Abstract—A theory is developed to predict the long range order parameter, composition and temperature at the interface of a chemically ordered phase as a function of interface velocity and liquid composition during rapid crystal growth. It extends the solute trapping theory of Aziz to a solid phase consisting of two sublattices. The engulfment of atoms randomly on the two sublattices by the rapidly moving liquid–solid interface is balanced against the interdiffusion across the interface that attempts to restore local equilibrium. With increasing interface velocity the theory predicts a progression from the solidification of a phase with equilibrium long range order parameter and with equilibrium solute partitioning to the solidification of a disordered crystalline phase with the same composition as the liquid. Predictions for solids with free energy functions in which the order disorder transition is first or second order show that the decrease of order parameter to zero with increasing interface velocity will be discontinuous or continuous respectively. Also solute trapping can occur at either a higher or a lower growth rate than disorder trapping depending on the free energy function.

Résumé—On développe une théorie pour prédire le paramètre d'ordre à longue distance, la composition et la température à l'interface d'une phase ordonnée chimiquement, en fonction de la vitesse de l'interface et de la composition du liquide pendant la croissance cristalline rapide. Cette théorie étend la théorie du piégeage de soluté d'Aziz à une phase solide constituée de deux sous-réseaux. L'engouffrement des atomes au hasard sur les deux sous-réseaux, grâce au déplacement rapide de l'interface liquide–solide, est équilibré par l'interdiffusion à travers l'interface qui tend à restaurer l'équilibre local. Lorsque la vitesse de l'interface augmente, la théorie prédit le passage de la solidification d'une phase—avec un paramètre d'ordre à longue distance à l'équilibre et un répartition du soluté à l'équilibre—à la solidification d'une phase cristalline désordonnée de même composition que le liquide. Les prédictions qui concernent les solides dont les fonctions d'énergie libre sont telles que la transition ordre–désordre est du premier ou du second ordre montrent que la décroissance du paramètre d'ordre vers zéro pour une vitesse d'interface croissante sera respectivement discontinue ou continue. En outre, le piégeage du soluté peut se produire à une vitesse de croissance supérieure ou inférieure à celle de piégeage dans l'état désordonné selon la fonction d'énergie libre.

Zusammenfassung—Es wird eine Theorie entwickelt, um den Parameter der Fernordnung, die Zusammensetzung und die Temperatur an der Grenzfläche einer chemisch geordneten Phase in Abhängigkeit von der Geschwindigkeit der Grenzfläche und der Zusammensetzung der Flüssigkeit während des raschen Kristallwachstums zu berechnen. Die Theorie erweitert die Theorie von Aziz zum Einfangen von Dotierstoffen auf die Festkörperphase, die aus zwei Untergittern besteht. Die von der sich rasch bewegenden fest-flüssigen Phasengrenze verursachte zufällige Verteilung der Atome auf die Gitterplätze wird verglichen mit der Diffusion durch die Grenzfläche, welche das lokale Gleichgewicht wieder herstellen möchte. Mit zunehmender Geschwindigkeit der Grenzfläche ergibt sich, daß das System von der Erstarrung einer Phase mit dem Gleichgewichts-Ordnungsparameter und mit der Gleichgewichtsverteilung der gelösten Atome auf die Erstarrung einer entordneten kristallinen Phase mit derselben Zusammensetzung wie die Flüssigkeit übergeht. Voraussagen der Theorie für Festkörper mit Funktionen der freien Energie zeigen für den Fall, daß des Ordnungs-Entordnungsübergang von erster Ordnung ist, einen diskontinuierlichen Abfall des Ordnungsparameters auf Null. Im Falle eines Übergangs zweiter Ordnung ist dieser Abfall auf Null kontinuierlich. Außerdem kann der gelöste Stoff bei einer höheren oder einer niedrigeren Wachstumsrate eingefangen werden, als beim Einfang im entordneten Festkörper, dies hängt von der Funktion der freien Energie ab.

1. INTRODUCTION

Over the years, considerable attention has been paid to the kinetics of motion of the interface separating two phases, especially to the kinetics of solidification of a melt. Recent interest in the rapid solidification processing of alloys and other materials using transformations far from equilibrium has renewed interest in these kinetics. Theories of nonequilibrium incorporation of solute into rapidly growing crystals [1–9] are currently the focus of experimental tests [10, 11]. An interesting additional possibility occurs for intermetallic compounds or other crystals with long range chemical order. Rapid growth can also cause the formation of crystals with nonequilibrium long range order in addition to nonequilibrium solute incorporation. Because ordering in the solid state during post-solidification cooling can mask events at the liquid–solid interface, quantitative experiments to measure the state of long-range order of the solidifying material are difficult to design. However, the observation of solidified phases with high densities of antiphase domains when the phase is normally ordered to the melting point is a clear indication that disorder has been trapped by the process of rapid solidification [12–16]. Thus a theory to treat this situation is appropriate.

A brief review of kinetic theories for trapping indicates the existence of two categories, diffuse and sharp interface theories. Baker [6] solved the dilute solution continuum diffusion equation in a moving reference frame across a diffuse interface to predict solute trapping by rapid growth. More recently the Cahn–Hilliard equation has been solved in a moving frame across a diffuse interface to predict in a formal way that certain kinds of disorder can be induced into a growing phase by rapid interface motion [17–20]. Many sharp interface theories are typified by the approach of Chernov [21]. This approach has been applied to both solute trapping during rapid solidification of disordered solid solutions [7] and disorder trapping during solidification of stoichiometric compounds [22]. Analytic and Monte-Carlo models of trapping based on very similar principles to Chernov's have been developed by others [4, 5, 8, 9, 23–25]. Probabilities are assigned for *each* species to hop into or out of the crystal based on the temperature and the chemical (and structural, e.g. location at a kink) environment; the net hopping rates are summed to yield the growth velocity. The flux of *each* species across the interface is a function of the chemical potential difference across the interface for *that species only*, being independent of the chemical potential differences for the other species. According to these models, for an atom to be incorporated into a high energy site, it must actively hop into such a site. In general these models do not predict incorporation in excess of the equilibrium amount (to obtain solute trapping) without additional assumptions about processes occurring at the interface, such as a preferential adsorption of solute at the interface.

In the contrasting approach of Aziz [1], if the impurity does nothing it may end up on a high energy site by virtue of the formation by its neighbors of a regular lattice around it. Hence to *avoid* incorporation onto a high energy lattice site, at atom must diffuse away†. Since the maximum speed of diffusion can be rather slow compared to the speed with which crystal–melt interfaces have been observed to move [26–28], the atom may be trapped on a high energy site by a rapidly moving interface. This implies a strong cross-coupling between the fluxes and driving forces of the individual species [29]. These assumptions have been shown experimentally to be much more reasonable, at least for solute trapping during rapid solidification [10, 11], than that requiring each atom to actively hop into its final site in the crystal.

In this paper we develop a sharp interface theory using the latter approach for the kinetics of crystallization of an ordered phase at an atomically "rough" interface, i.e. there are no special sites such as ledges, kinks, or dislocations. The interface temperature (undercooling) and the composition and order parameter of the solid will be predicted as functions of the interface velocity and composition of the liquid at the interface. It is the first theory to treat the simultaneous trapping of solute and disorder. This is carried out by modelling solute trapping of the undesirable species on each sublattice. The mean of the sublattice compositions yields the overall solid composition; their difference yields the long range order parameter. First, the conditions for equilibrium between a liquid and a solid phase consisting of two equivalent sublattices are developed in a form required for the kinetic theory. Second, the kinetic theory is presented; and third, numerical results are presented for the growth of solid phases normally ordered to the solidus temperature. This is done for two cases for free energy functions in which the order–disorder transitions (that would occur if the solid did not melt) are first and second order.

2. THERMODYNAMICS OF THE PHASES AT EQUILIBRIUM

We assume for simplicity that the solid phase consists of two equivalent sublattices α and β with no vacancies and that a total free energy function for the solid, G^{T} is a function of n_i^j the number of moles of component $i (i = \mathrm{A, B})$ on sublattice $j (j = \alpha, \beta)$. The constraint of equal number of lattice sites of the two sublattices requires that $n_{\mathrm{A}}^{\alpha} + n_{\mathrm{B}}^{\alpha} = n_{\mathrm{A}}^{\beta} + n_{\mathrm{B}}^{\beta}$. One can formally define the chemical potential of component i on the j sublattice as

$$\mu_i^j = \frac{\partial G^{\mathrm{T}}}{\partial n_i^j}. \tag{1}$$

Minimizing G^{T} subject to the constraint leads to the conditions for equilibrium in the solid phase given by

$$\mu_{\mathrm{B}}^{\alpha} - \mu_{\mathrm{A}}^{\alpha} = \mu_{\mathrm{B}}^{\beta} - \mu_{\mathrm{A}}^{\beta}. \tag{2}$$

If we assume that the constraint on the number of moles of each sublattice also holds in the solid at an interface with a liquid phase then one also obtains at equilibrium

$$\begin{aligned} \tfrac{1}{2}(\mu_{\mathrm{A}}^{\alpha} + \mu_{\mathrm{A}}^{\beta}) &= \mu_{\mathrm{A}}^{\mathrm{L}} \\ \tfrac{1}{2}(\mu_{\mathrm{B}}^{\alpha} + \mu_{\mathrm{B}}^{\beta}) &= \mu_{\mathrm{B}}^{\mathrm{L}} \end{aligned} \tag{3}$$

---

† For growth of intermetallic compounds some of the atoms, of course, will by chance by incorporated onto the right sublattice even if they do no hopping.

where μ_A^L and μ_B^L are the chemical potentials in the liquid phase. As a consequence of (2) and (3), the conditions

$$\mu_B^\alpha - \mu_A^\alpha = \mu_B^L - \mu_A^L$$

$$\mu_B^\beta - \mu_A^\beta = \mu_B^L - \mu_A^L \qquad (4)$$

also hold at equilibrium. These conditions must be satisfied at the zero growth velocity limit of any kinetic theory. It is important to note that the conditions for equilibrium involve only sums and differences of the sublattice chemical potentials, which individually can be defined only formally.

The free energy of the solid phase is more conveniently written on a molar basis, G_m^S in terms of the compositions of A and B atoms on the α and β sublattices, x_A^α, x_B^α, x_A^β, x_B^β with $x_i^j = n_i^j/(n_A^j + n_B^j)$.

Then

$$x_A^\alpha = x_A^S + \tfrac{1}{2}\eta$$

$$x_A^\beta = x_A^S - \tfrac{1}{2}\eta$$

$$x_B^\alpha = x_B^S - \tfrac{1}{2}\eta$$

$$x_B^\beta = x_B^S + \tfrac{1}{2}\eta \qquad (5)$$

if the long range order parameter, η is given by

$$\eta = x_A^\alpha - x_A^\beta = x_B^\beta - x_B^\alpha \qquad (6)$$

and the solid compositions, x_A^S, x_B^S, are given by

$$x_A^S = \tfrac{1}{2}(x_A^\alpha + x_A^\beta)$$

$$x_B^S = \tfrac{1}{2}(x_B^\alpha + x_B^\beta). \qquad (7)$$

Clearly $x_A^\alpha + x_B^\alpha = 1$, $x_A^\beta + x_B^\beta = 1$ and $x_A^S + x_B^S = 1$. With these definitions of composition, the molar free energy G_m^S is given by

$$G_m^S = \tfrac{1}{2}(\mu_A^\alpha x_A^\alpha + \mu_B^\alpha x_B^\alpha + \mu_A^\beta x_A^\beta + \mu_B^\beta x_B^\beta). \qquad (8)$$

If G_m^S is treated as a function of independent variables x_B^α and x_B^β then

$$\mu_B^\alpha - \mu_A^\alpha = 2\frac{\partial G_m^S}{\partial x_B^\alpha} \qquad (9)$$

$$\mu_B^\beta - \mu_A^\beta = 2\frac{\partial G_m^S}{\partial x_B^\beta} \qquad (10)$$

and

$$\tfrac{1}{2}(\mu_A^\alpha + \mu_A^\beta) = G_m^S - x_B^\alpha \frac{\partial G_m^S}{\partial x_B^\alpha} - x_B^\beta \frac{\partial G}{\partial x_B^\beta} \qquad (11)$$

$$\tfrac{1}{2}(\mu_B^\alpha + \mu_B^\beta) = G_m^S + (1 - x_B^\alpha)\frac{\partial G_m^S}{\partial x_B^\alpha} + (1 - x_B^\beta)\frac{\partial G_m^S}{\partial x_B^\beta}. \qquad (12)$$

If on the other hand independent variables, x_B^S and η, are used

$$\mu_B^\alpha - \mu_A^\alpha = \frac{\partial G_m^S}{\partial x_B^S} - 2\frac{\partial G_m^S}{\partial \eta} \qquad (9')$$

$$\mu_B^\beta - \mu_A^\beta = \frac{\partial G_m^S}{\partial x_B^S} + 2\frac{\partial G_m^S}{\partial \eta} \qquad (10')$$

and

$$\tfrac{1}{2}(\mu_A^\alpha + \mu_A^\beta) = G_m^S - x_B^S \frac{\partial G_m^S}{\partial x_B^S} - \eta \frac{\partial G_m^S}{\partial \eta} \qquad (11')$$

$$\tfrac{1}{2}(\mu_B^\alpha + \mu_B^\beta) = G_m^S + (1 - x_B^S)\frac{\partial G_m^S}{\partial x_B^S} - \eta \frac{\partial G_m^S}{\partial \eta}. \qquad (12')$$

Using equations (9′–10′) it can be seen that equation *(2) is equivalent to the ordinary condition for equilibrium order*, $\partial G_m^S/\partial\eta = 0$.

3. THERMODYNAMIC CONSTRAINT ON SOLID COMPOSITION AND ORDER PARAMETER DURING CRYSTALLIZATION

The solidification process must always involve a decrease in free energy ΔG. Baker and Cahn [30] have described the domain of possible solid compositions that can form for various liquid compositions at a given temperature by requiring that $\Delta G \leqslant 0$ where

$$\Delta G = G_m^S - (\mu_A^L x_A^S + \mu_B^L x_B^S) \qquad (13)$$

which is equation (15) of Ref. [30] in a different form. Equation (13) is the basis for the usual "tangent to curve rule" to graphically show the change in free energy for a given phase change. Here G_m^S is evaluated for the composition of the solid phase and μ_A^L and μ_B^L are evaluated for the composition of the liquid phase. Application of this principle to the present case where G_m^S also depends on η *will yield domains of allowable* order parameter and solid composition that can solidify from various liquid compositions at a given temperature. Any prediction of a kinetic model must yield values of η, solid composition, and temperature for each liquid composition and growth velocity that will give $\Delta G \leqslant 0$. Furthermore it can be easily shown that the conditions for equilibrium given by the three equations (2) and (3) are equivalent to the condition $\Delta G = 0$ when combined with equation (4). This latter set will be satisfied in the zero velocity limit of the kinetic theory presented below.

Figure 1 shows *schematically* the domain of allowable order parameter that can form at various temperatures for a congruently melting compound if the liquid composition is equal to the solid composition. These domains as well as the detailed kinetic results described later in this paper depend on whether the ordered phase differs from the disordered phase by a second or first order transition depicted in (a) and (b), respectively. At the top of Fig. 1(a) and (b) are shown the free energies of the solid and liquid at three temperatures. At the equilibrium melting temperature T_1, only one value of η is possible. Below T_1, $\Delta G \leqslant 0$ defines a range of allowable η shown in the cross hatched region in the bottom of the figures. Note that only when the $T \leqslant T_3$ in (a) or $T \leqslant T_2$ in (b) can a solid with $\eta = 0$ form. If the liquid and solid compositions are not assumed equal, ranges of solid composition and η allowable at each temperature for a given liquid composition are described by the condition $\Delta G \leqslant 0$ (not shown).

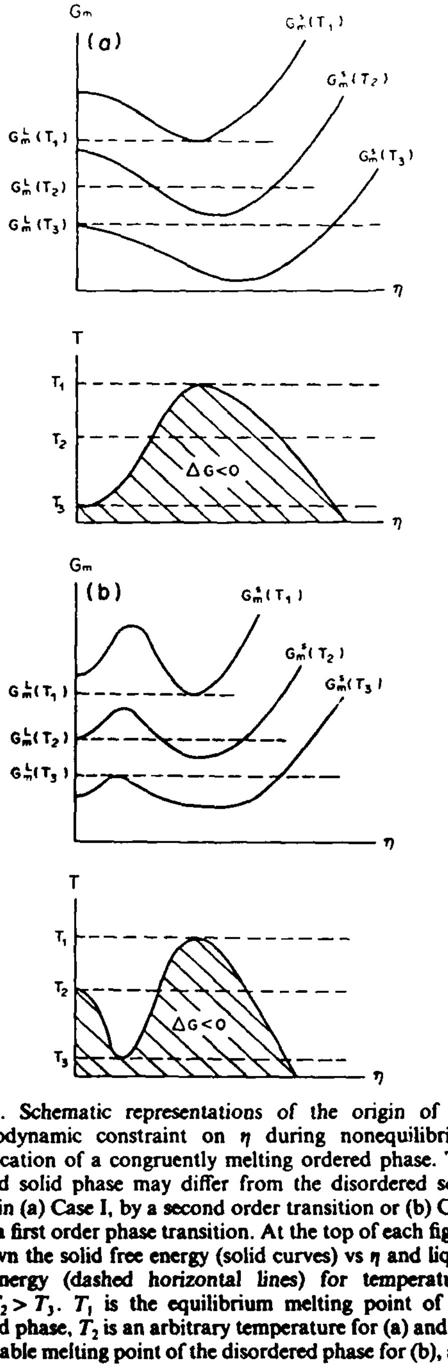

Fig. 1. Schematic representations of the origin of the thermodynamic constraint on η during nonequilibrium solidification of a congruently melting ordered phase. The ordered solid phase may differ from the disordered solid phase in (a) Case I, by a second order transition or (b) Case II, by a first order phase transition. At the top of each figure is shown the solid free energy (solid curves) vs η and liquid free energy (dashed horizontal lines) for temperatures $T_1 > T_2 > T_3$. T_1 is the equilibrium melting point of the ordered phase, T_2 is an arbitrary temperature for (a) and the metastable melting point of the disordered phase for (b), and T_3 is the unstable melting point of the ordered phase. The condition, $G_S - G_L < 0$, defines a range of η as a function of solidification temperature where solidification is possible as shown at the bottom of each figure.

4. A KINETIC THEORY FOR THE INTERFACE

A kinetic theory for the interface establishes a relationship among the variables of state at the liquid solid interface and the interface velocity and perhaps also orientation, curvature etc. These relationships become the boundary conditions for solution of the entire problem of crystal growth that includes long range heat and diffusion transport. In the present case we restrict attention to so-called continuous growth where the interface is atomistically rough so that orientation and special sites such as kinks and ledges play no role. We seek three expressions that will give the interface temperature, solid composition, and order parameter as functions of the velocity and the interface liquid composition. The choice of the two independent variables out of the five is arbitrary.

This theory follows the general formulation developed by Aziz [1]. Solidification is treated as a superposition of two distinct reactions: crystallization via the advance of the interface across a monolayer of liquid alloy, and solute–solvent redistribution via interdiffusion of the two species between liquid and solid monolayers. The rate of each reaction is written separately.

4.1. Crystallization

We will assume that the solidification velocity V is related to the free energy change for crystallization ΔG according to

$$V = V_c\left[1-\exp\left(\frac{\Delta G}{RT}\right)\right] \tag{14}$$

where V_c is a kinetic rate parameter for crystallization and ΔG, defined by equation (13), is negative for solidification. This expression is a generalization of the classical model of continuous growth of a single component material [31]. The single component model is derived from chemical rate theory by assuming that the barrier to crystallization remains a fixed height above the liquid free energy. Equation (14) is consistent with a wide variety of data for growth in high viscosity melts and correspondingly low mobility interfaces [32]. V_c in these systems is approximately the speed of liquid interdiffusion (D_L/λ) where D_L is the liquid diffusion coefficient and λ is the jump distance. However in simple molecular systems such as metals and alloys, Turnbull has suggested [26, 31], and experiments on pure systems tend to support [26–28], that the rate of interface advance may be limited only by the rate at which atoms collide with the interface. In such cases V_c is of the order of the speed of sound, which is typically three orders of magnitude greater than D_L/λ.

From a purely phenomenological point of view the form of equation (14) maintains the thermodynamic constraint on the temperature, composition and order parameter described in Section 3, produces a linear relation between velocity and ΔG for small deviation from equilibrium and limits the growth to finite rates at infinite driving force.

4.2. Solute redistribution

We consider a pair of reactions between liquid and each sublattice from initial states (of B in an α or β site in the solid adjacent to A in the liquid) over a barrier to final states (where the two atoms have exchanged positions) as shown in Fig. 2. Written as

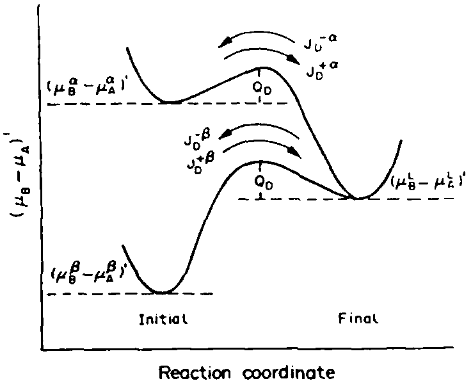

Fig. 2. Redistribution potential diagram for interface redistribution reaction. Initial states: *B* on α or β site in solid, *A* in liquid. Final states: *A* on α or β site in solid, *B* in liquid. The barrier height is assumed to be Q_D above the higher potential.

chemical reactions,

$$B_\alpha + A_L = A_\alpha + B_L$$

$$B_\beta + A_L = A_\beta + B_L.$$

In a reference frame fixed on the crystal lattice the forward reactions can be characterized by atomistic interdiffusion fluxes designated $J_D^{+\alpha}$ and $J_D^{+\beta}$, and the reverse reactions by fluxes $J_D^{-\alpha}$ and $J_D^{-\beta}$, expressed in *exchanges per unit time per unit area of* α (or β) sublattice. These interdiffusion fluxes between adjacent liquid and solid monolayers must have specific values, dependent on the growth rate and the compositions of the monolayers, in order to maintain the steady state.

The fluxes will be written as the product of an attempt frequency *v*, the sublattice and liquid compositions, and a Boltzman factor in the barrier height. When fluxes are written using composition variables, the potential for the barrier must be the non-ideal part of the chemical potential, $\mu' \equiv \mu - RT \ln x$ [33]. In addition since we will consider only the direct interchange of *A* and *B* atoms, the relevant potential for interdiffusion is $(\mu_B - \mu_A)'$, which we will call the redistribution potential. Because interchanges between liquid and solid are being considered, potentials for the liquid phase, $(\mu_B^L - \mu_A^L)'$ and the α and β sublattices of the solid phase, $(\mu_B^\alpha - \mu_A^\alpha)'$ and $(\mu_B^\beta - \mu_A^\beta)'$ are required. They will be obtained from a specific thermodynamic model of the phases.

We assume the barrier to redistribution remains a constant height Q_D, independent of temperature and composition, above the state (initial or final) with the higher redistribution potential. Although other assumptions are possible for the barrier height, this choice is consistent with that used above for crystallization. Phenomenologically this assumption also prevents the disappearance of the barrier at high potential difference. Fluxes from a higher to a lower redistribution potential are written with a Boltzman factor, $\exp(-Q_D/RT)$. Fluxes from a lower to a higher redistribution potential are written with a Boltzman factor

$$\exp\{-[Q_D + |(\mu_B^j - \mu_A^j)' - (\mu_B^L - \mu_A^L)'|]/RT\}$$

with $j = \alpha, \beta$. The potential that is higher or lower depends on the values of order parameter and compositions at the interface. The identical assumption regarding the barrier heights was made by Aziz and Kaplan [2] for the growth of disordered solid solutions. It implies that the exchanges are governed by the properties of the interface and not the bulk solid or liquid phases. We will also assume that Q_D for the exchanges from the two sublattices to the liquid are the same. The consequences of relaxing this assumption will be described in the discussion section of this paper.

Due to the above assumptions regarding the barrier heights it is necessary to introduce parameters $A_j (j = \alpha, \beta)$ with

$$A_j = \begin{bmatrix} 0 & \text{if} & (\mu_B^j - \mu_A^j)' - (\mu_B^L - \mu_A^L)' \geqslant 0 \\ 1 & \text{if} & (\mu_B^j - \mu_A^j)' - (\mu_B^L - \mu_A^L)' < 0. \end{bmatrix} \tag{15}$$

The interdiffusion fluxes are then given by

$$\boxed{\begin{aligned} J_D^{+\alpha} &= \frac{f\nu\lambda}{\Omega} x_B^\alpha(1 - x_B^L)\exp\left[\frac{-[Q_D + A_\alpha|(\mu_B^\alpha - \mu_A^\alpha)' - (\mu_B^L - \mu_A^L)'|]}{RT}\right] \\ J_D^{-\alpha} &= \frac{f\nu\lambda}{\Omega} x_B^L(1 - x_B^\alpha)\exp\left[\frac{-[Q_D + (1 - A_\alpha)|(\mu_B^\alpha - \mu_A^\alpha)' - (\mu_B^L - \mu_A^L)'|]}{RT}\right] \\ J_D^{+\beta} &= \frac{f\nu\lambda}{\Omega} x_B^\beta(1 - x_B^L)\exp\left[\frac{-[Q_D + A_\beta|(\mu_B^\beta - \mu_A^\beta)' - (\mu_B^L - \mu_A^L)'|]}{RT}\right] \\ J_D^{-\beta} &= \frac{f\nu\lambda}{\Omega} x_B^L(1 - x_B^\beta)\exp\left[\frac{-[Q_D + (1 - A_\beta)|(\mu_B^\beta - \mu_A^\beta)' - (\mu_B^L - \mu_A^L)'|]}{RT}\right]. \end{aligned}} \tag{16}$$

The parameter *f* is the fraction of sites at the interface where jumps can occur, λ is the jump distance, and Ω is the atomic volume (assumed independent of component or phase)

The net diffusive fluxes, J_D^α and J_D^β, are then

$$J_D^\alpha = J_D^{+\alpha} - J_D^{-\alpha} = [D_i/(\lambda\Omega)][x_B^\alpha(1 - x_B^L)K_\alpha^{A_\alpha} - x_B^L(1 - x_B^\alpha)K_\alpha^{(1-A_\alpha)}] \tag{17}$$

and

$$J_D^\beta = J_D^{+\beta} - J_D^{-\beta} = [D_i/(\lambda\Omega)][x_B^\beta(1 - x_B^L)K_\beta^{A_\beta} - x_B^L(1 - x_B^\beta)K_\beta^{(1-A_\beta)}] \tag{18}$$

where

$$K_\alpha = \exp\left[\frac{-|(\mu_B^\alpha - \mu_A^\alpha)' - (\mu_B^L - \mu_A^L)'|}{RT}\right]$$

$$K_\beta = \exp\left[\frac{-|(\mu_B^\beta - \mu_A^\beta)' - (\mu_B^L - \mu_A^L)'|}{RT}\right] \quad (19)$$

and

$$D_i = f\nu\lambda^2 \exp\left\{-\frac{Q_D}{RT}\right\} \quad (20)$$

which we call the interface diffusivity.

To maintain steady state conditions at the moving interface a mass balance must be satisfied. In order to extract a simple model for the present we will assume that interdiffusion in the liquid is fast enough to prevent lateral composition variations in the first liquid monolayer and that interdiffusion in the solid is slow enough that lateral exchanges (ordering) in the first solid monolayer do not occur. In this case mass balance requires that

$$J_D^\alpha = \frac{V}{\Omega}(x_B^L - x_B^\alpha)$$

$$J_D^\beta = \frac{V}{\Omega}(x_B^L - x_B^\beta) \quad (21)$$

where V is the interface velocity. Equating expressions for the net diffusive fluxes we obtain

$$x_B^\alpha(1 - x_B^L)K_\alpha^{A_\alpha} - x_B^L(1 - x_B^\alpha)K_\alpha^{(1-A_\alpha)} = \frac{V}{V_D}(x_B^L - x_B^\alpha)$$

$$x_B^\beta(1 - x_B^L)K_\beta^{A_\beta} - x_B^L(1 - x_B^\beta)K_\beta^{(1-A_\beta)} = \frac{V}{V_D}(x_B^L - x_B^\beta) \quad (22)$$

where $V_D = D_i/\lambda$. V_D is a kinetic rate parameter for redistribution and has been called the interface diffusive speed.

The three equations (14) and (22) completely describe the interface conditions. One may choose to solve these equations for a given V and x_B^L in order to find the temperature and compositions of the α and β sublattices. This would yield the average solid composition and the long range order parameter at the interface. At $V = 0$ these three equations reduce to $\Delta G = 0$ and the two conditions given by equation (4), which define the interface at equilibrium. To obtain kinetic predictions we require values for the kinetic parameters V_C and V_D as well as the redistribution potentials, which depend on temperature and the various compositions through a specific thermodynamic model of the liquid and solid phases.

5. CHOICE OF THERMODYNAMIC POTENTIALS

The predictions of this theory will be examined for phase diagrams having a congruently melting ordered phase at $x_B = 0.5$. Thus the order–disorder temperature of the solid phase must be chosen to be higher than the congruent melting temperature. The following form of the solid free energy, G_m^S, will also permit the comparison of the predictions when this order–disorder transition is first order or second order

$$\begin{aligned} G_m^S = {} & G_A^S(1 - x_B^S) + G_B^S x_B^S \\ & + \Omega_1\{x_B^S(1 - x_B^S) + \tfrac{1}{4}\eta^2\} + \Omega_2\eta^4 \\ & + \tfrac{1}{2}RT\{(x_B^S - \tfrac{1}{2}\eta)\ln(x_B^S - \tfrac{1}{2}\eta) \\ & + (x_B^S + \tfrac{1}{2}\eta)\ln(x_B^S + \tfrac{1}{2}\eta) \\ & + (1 - x_B^S - \tfrac{1}{2}\eta)\ln(1 - x_B^S - \tfrac{1}{2}\eta) \\ & + (1 - x_B^S + \tfrac{1}{2}\eta)\ln(1 - x_B^S + \tfrac{1}{2}\eta)\} \end{aligned} \quad (23)$$

where G_A^S and G_B^S are the free energies of pure solid A and B and Ω_1 and Ω_2 are constants. If $\Omega_2 = 0$ and $\Omega_1 < 0$, equation (23) describes a Bragg–Williams phase with near neighbor interaction Ω_1 and ideal entropy. The η-dependence of the free energy curve for $x_B^S = 0.5$ is shown schematically in Fig. 1(a). The transition between the ordered and disordered phase is a second order phase transition, i.e. the equilibrium order parameter goes to zero continuously as temperature is increased. If $\Omega_2 < 0$ and $\Omega_1 \gtrsim 12\Omega_2$ the η-dependence of the free energy curve for $x_B^S = 0.5$ is shown schematically in Fig. 1(b). The transition between ordered and disordered phase is a first order phase transition, i.e. the equilibrium order parameter has a discontinuous drop to zero.

For the choice of G_m^S given in equation (23), equations (9′–12′) give

$$\begin{aligned} \mu_B^\alpha - \mu_A^\alpha = {} & G_B^S - G_A^S + \Omega_1(1 - 2x_B^S - \eta) - 8\Omega_2\eta^3 \\ & + RT[\ln(x_B^S - \tfrac{1}{2}\eta) - \ln(1 - x_B^S + \tfrac{1}{2}\eta)] \\ \mu_B^\beta - \mu_A^\beta = {} & G_B^S - G_A^S + \Omega_1(1 - 2x_B^S + \eta) + 8\Omega_2\eta^3 \\ & + RT[\ln(x_B^S + \tfrac{1}{2}\eta) - \ln(1 - x_B^S - \tfrac{1}{2}\eta)] \end{aligned} \quad (24)$$

$$\begin{aligned} \tfrac{1}{2}(\mu_A^\alpha + \mu_A^\beta) = {} & G_A^S + \Omega_1\{(x_B^S)^2 - \tfrac{1}{4}\eta^2\} - 3\Omega_2\eta^4 \\ & + \tfrac{1}{2}RT\{\ln[(1 - x_B^S)^2 - \tfrac{1}{4}\eta^2]\} \\ \tfrac{1}{2}(\mu_B^\alpha + \mu_B^\beta) = {} & G_B^S + \Omega_1\{(1 - x_B^S)^2 - \tfrac{1}{4}\eta^2\} - 3\Omega_2\eta^4 \\ & + \tfrac{1}{2}RT\{\ln[(x_B^S)^2 - \tfrac{1}{4}\eta^2]\} \end{aligned} \quad (25)$$

and redistribution potentials

$$(\mu_B^\alpha - \mu_A^\alpha)' = G_B^S - G_A^S + \Omega_1(1 - 2x_B^S - \eta) - 8\Omega_2\eta^3$$

$$(\mu_B^\beta - \mu_B^\beta)' = G_B^S - G_A^S + \Omega_1(1 - 2x_B^S + \eta) + 8\Omega_2\eta^3. \quad (26)$$

For the liquid phase we will employ a regular solution model with

$$\mu_A^L = G_A^L + \Omega^L(x_B^L)^2 + RT\ln(1 - x_B^L)$$

$$\mu_B^L = G_B^L + \Omega^L(1 - x_B^L)^2 + RT\ln x_B^L \quad (27)$$

where Ω^L is a constant and G_A^L and G_B^L are free energies of pure liquid A and B. The redistribution potential is given by

$$(\mu_B^L - \mu_A^L)' = G_B^L - G_A^L + \Omega^L(1 - 2x_B^L). \quad (28)$$

Furthermore to obtain a phase diagram that is symmetric about $x_B = 0.5$, we must assume that

$$G_A^L - G_A^S = G_B^L - G_B^S = S(T_m - T) \qquad (29)$$

where S and T_m are the entropy of fusion and melting point of the pure components (assumed equal).

6. APPROXIMATE RESULT FOR DEPENDENCE OF ORDER PARAMETER ON VELOCITY AT A CONGRUENT MELTING MAXIMUM

A simple expression can be obtained from equations (22) for $x_B^L = 0.5$, which will provide some insight into the numerical results described in Section 7. Both equations are satisfied if $x_B^S = 0.5$ and if the order parameter satisfies

$$\frac{\Omega_1\eta + 8\Omega_2\eta^3}{RT} = \ln\left[\frac{(1-\eta) - 2\dfrac{V}{V_D}\eta}{1+\eta}\right] \qquad (30)$$

for $\eta \geqslant 0$†. Note that $\eta = 0$ is always a solution. A second solution with $\eta \neq 0$ may also exist. For $V = 0$ this equation gives the equilibrium order parameter of a single phase solid as a function of T for $x_B^S = 0.5$, which is identical to that obtained from equation (2). As a kinetic equation for solidification, T represents the interface temperature, which can only be determined using equation (14) in combination with equation (30). However, if we consider that the interface temperature may be approximated by the melting point of the ordered phase T_m^0, then equation (30), after rearrangement, becomes

$$\frac{V}{V_D} \simeq \frac{1}{2\eta}\left\{(1-\eta) - (1+\eta)\exp\left[\frac{\Omega_1\eta + 8\Omega_2\eta^3}{RT_m^0}\right]\right\}. \qquad (31)$$

This approximation predicts that η goes to zero as V/V_D goes to $(-\Omega_1/2RT_m^0 - 1)$. For the case where $\Omega_2 = 0$, the critical temperature T_C for the order-disorder transition at $x_B^S = 0.5$ is equal to $(-\Omega_1/2R)$. Therefore the critical value of V/V_D where the long range order parameter goes to zero is given by

$$\left(\frac{V}{V_D}\right)_{\eta=0} \simeq \frac{T_C}{T_m^0} - 1. \qquad (32)$$

Hence the rather intuitive result is obtained that the critical velocity for complete disorder trapping is high when T_C is much higher than the melting point, i.e. when the solid is highly ordered at the melting point. When $\Omega_2 \neq 0$, the critical velocity follows the same trend but is not so simply estimated.

7. NUMERICAL RESULTS

We will examine in parallel the calculated phase diagrams and results of the non-equilibrium interface theory for the two cases with thermodynamic parameters given in Table 1. The kinetic results will be shown as functions of dimensionless growth velocity V/V_D. However a numerical value for V_C/V_D must be chosen. A value of 10^3, independent of temperature and composition, is consistent with the notion that the crystallization reaction is collision limited but the redistribution reaction is short-range diffusion limited.

Table 1. Choice of thermodynamic parameters

	T_m(K)	S/R	Ω^L/R(K)	Ω_1/R(K)	Ω_2/R(K)
Case I	1000	2	0	−3000	0
Case II	1000	2	0	−2000	−566.2

7.1. *Equilibrium phase diagram*

Figure 3(a) and (b) show the equilibrium order parameter, η_e, of the solid as a function of T for the two cases for $x_B^S = 0.5$, obtained using equation (2). In *I*, the order–disorder (OD) temperature is 1500 K $(-\Omega_1/2R)$. In II, the OD temperature is 1583 K and is obtained by finding the temperature where G_S for $\eta = 0$ is equal to G_S for $\eta = \eta_e$. The dashed curve represents states where the ordered phase is metastable whereas the dotted curve represents states where the ordered phase is unstable. Cases I and II

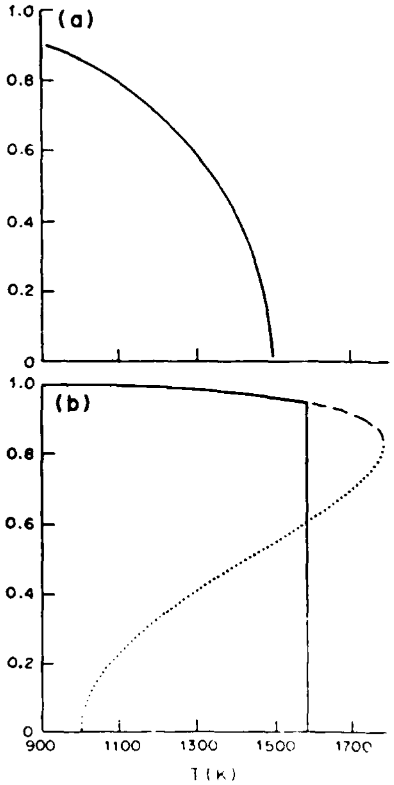

Fig. 3. Calculated equilibrium long range order parameter in the solid, η_e, as a function of temperature for $x_B^S = 0.5$. (a) Case I, order–disorder temperature is 1500 K. (b) Case II, order–disorder temperature is 1583 K. The dashed curve shows metastable ordered states, while the dotted curve shows unstable ordered states.

---

†For $\eta < 0$, equation (30) is modified due to the A_j factors and the theory predicts the same behavior for $\pm\eta$.

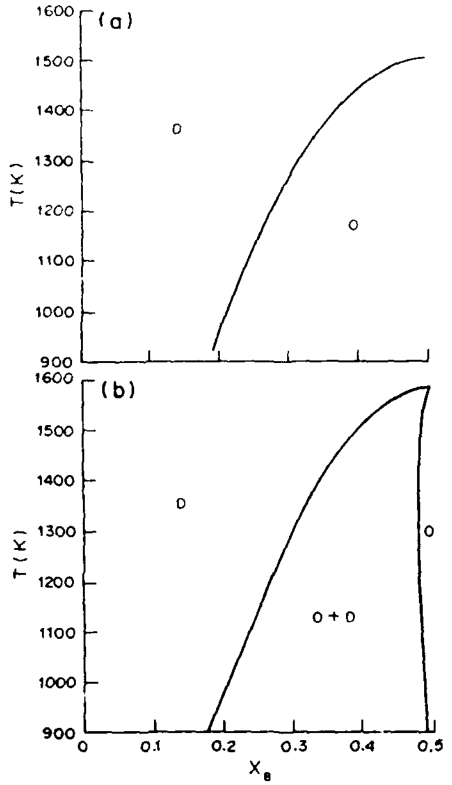

Fig. 4. Calculated phase diagram for solid phases only for (a) Case I and (b) Case II. Diagram is symmetric about $x_B = 0.5$. D and O represent the disordered and ordered phases respectively.

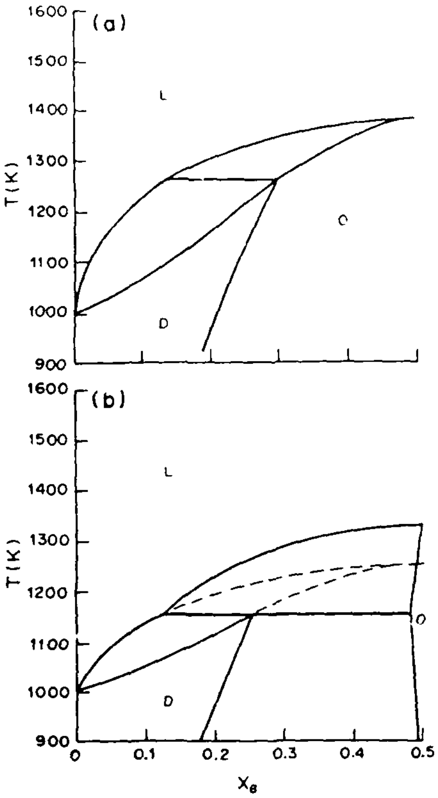

Fig. 5. Calculated equilibrium phase diagram for (a) Case I and (b) Case II. In (b) the dashed curve corresponds to the metastable liquidus and solidus for the disordered phase. L represents the liquid phase.

are respectively second and first order transitions. In this and the following figures, Case I (second order) and Case II (first order) are shown in (a) and (b) respectively.

Figure 4(a) and (b) show half of the phase diagrams for the solid phases only. In Fig. 4(a) no two-phase field exists between the ordered and disordered phase, characteristic of the second order transition. The curve is obtained from equation (2) by letting $\eta \to 0$. In Fig. 4(b) a two-phase field exists. The boundaries are obtained by equating the values of $(\mu_A^{\alpha} + \mu_A^{\beta})/2$ for $\eta = 0$ and $\eta = \eta_e$ obtained from equation (2) and by similarly equating the values of $(\mu_B^{\alpha} + \mu_B^{\beta})/2$.

Figures 5(a) and (b) show the equilibrium diagrams using equation (3) in combination with equation (2) to generate the liquid–solid equilibrium. In both cases the melting point of the composition $x_B = 0.5$ is below the OD temperature. The diagrams contain "peritectic reactions", $L + O \to D$; however, in Fig. 5(a) no discontinuity in slope occurs at the liquidus at the "peritectic temperature" due to the second order nature of the OD reaction. For case II a metastable liquidus and solidus are shown dashed for the disordered phase. For case I such curves would represent unstable thermodynamic equilibrium and are not shown.

7.2. *Non equilibrium interface conditions for a congruently melting ordered phase*

In general there are two solutions to equations (14) and (22) for the non-equilibrium interface conditions: one for $\eta = 0$ and one for $\eta \neq 0$. The $\eta \neq 0$ solution only exists below some critical value of V/V_D. Different parts of each solution are mathematically stable or unstable in the sense that small fluctuations in the order parameter during steady state growth will either be damped or amplified, respectively. Unstable portions will be shown dotted in the following figures. The details of this stability analysis will be deferred until the discussion.

For $x_B^S = 0.5$ equations (14) and (22) are satisfied for $x_B^L = 0.5$ and values of η and T as a function of V/V_D shown in Figs 6 and 7. In Fig. 6(a) for case I, the order parameter goes to zero continuously as a critical value of V/V_D is reached. The $\eta = 0$ solution is unstable below the critical velocity and stable above it. In Fig. 6(b) for case II the order parameter exhibits a turning or limit point at a critical value of V/V_D. If the velocity is increased above the limit point, the order parameter must jump discontinuously to the $\eta = 0$ solution, which is stable for all V in case II. In Fig. 6(b) the branch below the turning point is dotted and represents unstable solutions. At $V = 0$ this unstable branch corresponds to the

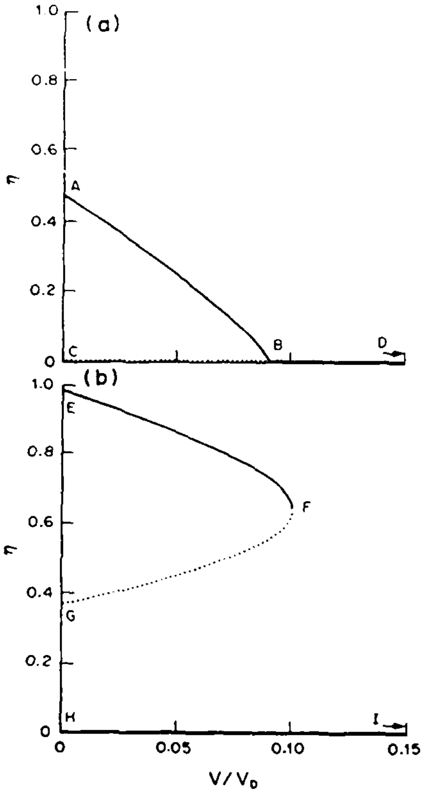

Fig. 6. Long range order parameter of the solid at the interface, η, as a function of dimensionless growth velocity, V/V_D for the congruently melting compound at $x_B^S = 0.5$ for (a) Case I, (b) Case II. Common interface conditions are denoted by the same capital letter in Figs 6–8. Solid and dotted curves are mathematically stable and unstable solutions to the kinetic equations respectively. Only the solid curves represent physically possible steady state interface conditions. The $\eta \approx 0$ solution in (a) is unstable between C and B but stable between B and D and in (b) is always stable.

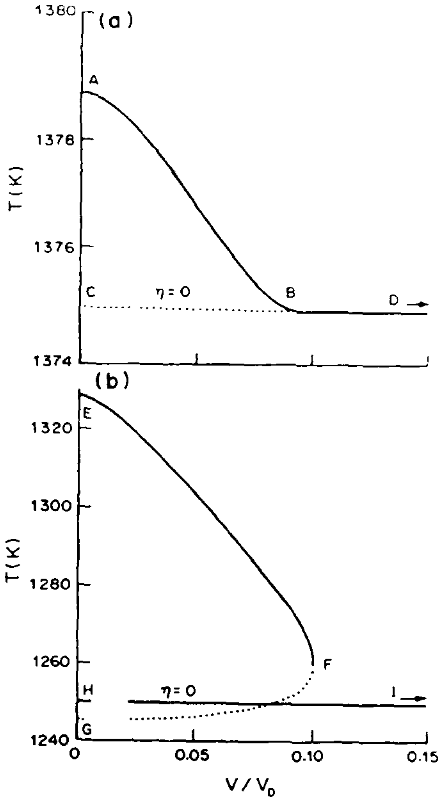

Fig. 7. Interface temperature T as a function of dimensionless growth velocity, V/V_D for the congruently melting compound at $x_B^S = 0.5$. (a) Case I, (b) Case II.

thermodynamically unstable equilibrium between the liquid and solid [see $T = T_3$ in Fig. 1(b)].

In Fig. 7, the interface temperatures for the $\eta = 0$ and $\eta \neq 0$ solutions are shown. Again the dotted portions are unstable. For case I, the $\eta = 0$ solution is only stable above the critical velocity. For case II the $\eta = 0$ solution is always stable and at $V = 0$ corresponds to metastable equilibrium between the melt and the disordered phase.

Figure 8 shows cross plots of η and T that occur for the various values of V/V_D in Figs 6 and 7. Also included in the figure are the equilibrium order parameter, η_e vs temperature as shown originally in Fig. 3. The points labelled A and E correspond to $V = 0$ (equilibrium). Point H corresponds to $V = 0$ for metastable equilibrium between liquid and disordered solid.

7.3. *Simultaneous disorder and solute trapping*

For compositions away from the congruent maximum of the ordered phase, the possibility of non-equilibrium incorporation of solute (solute trapping) as well as disorder trapping is possible. Figures 9 and 10 show the order parameter and liquid composition at the interface as a function of V/V_D for $x_B^S = 0.48$ for the two cases. The behavior of the order parameter is quite similar to that for $x_B^S = 0.5$†. Figure 10 is shown with a logarithmic scale for velocity to permit comparison to previous theory [1, 2] on solute trapping of disordered solids. In both cases I and II the composition of the liquid approaches the composition of the solid at high velocity.

Near the velocity where η goes to zero in case I (point B) or where the turning point occurs in case II (F) in Fig. 9, the liquid compositions shown in Fig. 10 have abrupt changes. In case I the lower curve for the $\eta \neq 0$ solution merges with that for the $\eta = 0$ solution. Below this merge point the $\eta = 0$ solution is unstable and is shown dotted. In case II, the liquid composition curve (H to I) for the $\eta = 0$ solution is stable for all velocities and corresponds to solute trapping in the disordered phase. This curve could have been obtained from results of [2]. For the $\eta \neq 0$ solution however, the liquid composition exhibits a turning point at the same velocity where η has a turning point in Fig. 9(b). In this case the lower

---

†For Case I, the slope at B is finite for $x_B^S = 0.5$ but infinite for $x_B^S = 0.48$. This difference is due to the A_i factors which change at $\eta = 0$ and $\eta \simeq 0.03$ for the two compositions respectively.

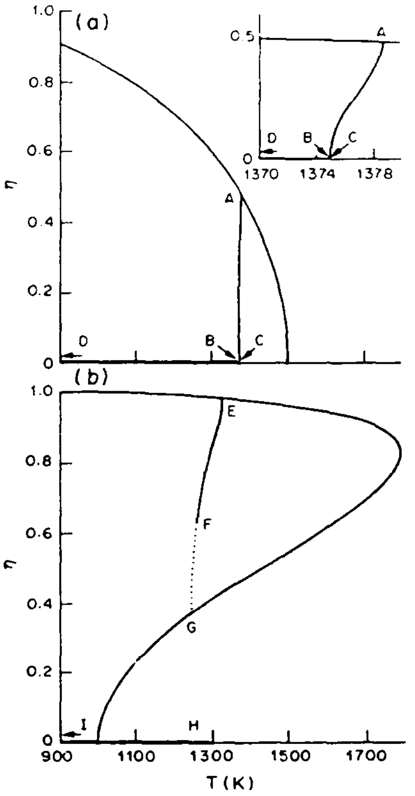

Fig. 8. Cross plot of order parameter and interface temperature parameterized by V/V_D for (a) Case I and (b) Case II. Also shown are the equilibrium order parameter at the various temperatures taken from Fig. 3. The $\eta = 0$ solution in (a) is unstable along a very short segment between C and B but stable between B and D and in (b) exists between H and I and is stable.

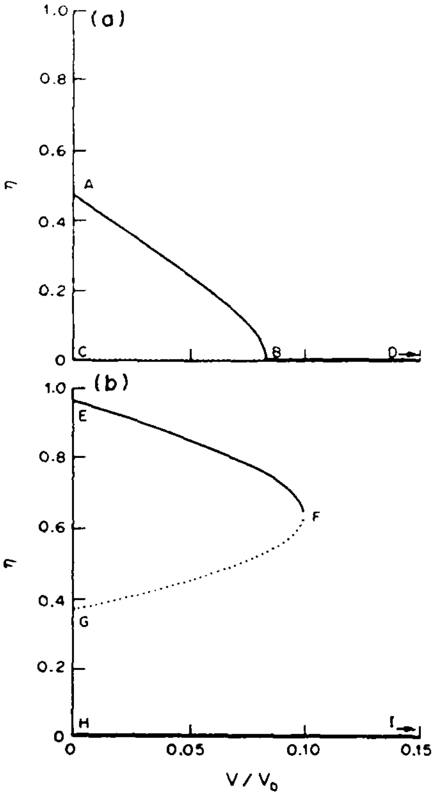

Fig. 9. Long range order parameter of the solid at the interface, η, as a function of dimensionless growth velocity, V/V_D for (a) Case I with $x_B^S = 0.48$, and (b) Case II with $x_B^S = 0.48$. Identical interface conditions are denoted by the same capital letter in Figs 9 and 10. The $\eta = 0$ solution in (a) is unstable between C and B but stable between B and D and in (b) is always unstable.

branch (E to F) is stable and the upper branch (F to G) is unstable. Thus for case II the theory predicts that with increasing velocity a jump in liquid composition at the interface occurs when η goes to zero. As shown, the size of the jump is small, but it of course depends on the thermodynamic potentials used.

It is also interesting to note in case I, η goes to zero at a velocity where solute redistribution remains significant; whereas in case II, η goes to zero at a velocity where solute trapping is practically complete ($x_B^L \simeq x_B^S$). Numerical results for other values of Ω_1 and Ω_2 not described here suggest that the relative ease of solute vs disorder trapping depends mostly on the curvature of the solid free energy function in the directions of order parameter and composition rather than whether the ordering transition for the solid phase is first or second order. It seems that non-equilibrium interface states that tend to minimize the free energy increase from equilibrium are favored for trapping at lower velocities.

8. DISCUSSION

8.1. *Assumptions*

While there are a considerable number of assumptions used to construct the present theory, a basis has been provided for examining the response of intermetallic compounds to rapid solidification processing. The theory permits crystal growth at speeds high enough that both solute and disorder can be trapped into growing crystals consistent with the few observations available. This is a direct consequence of the fact that the theory separates the crystallization step from the redistribution step allowing the crystallization rate parameter, V_C, to be set much higher than the redistribution rate parameter, V_D.

One of the major assumptions involves the choice of reference state for the construction of the barrier height Q_D used to calculate the interdiffusion fluxes. This required the introduction of the "A" parameters to monitor the side of the interface with the higher redistribution potential. It is important to point out however that the location of the interesting transitions points, for example points B and F in Fig. 10 do not occur where the "A" factors change. Similar transitions would occur for other definitions of the reference state not requiring the introduction of the "A" factors.

The validity of the assumptions regarding complete mixing in the first liquid monolayer and the absence of lateral atomic rearrangements in the first solid

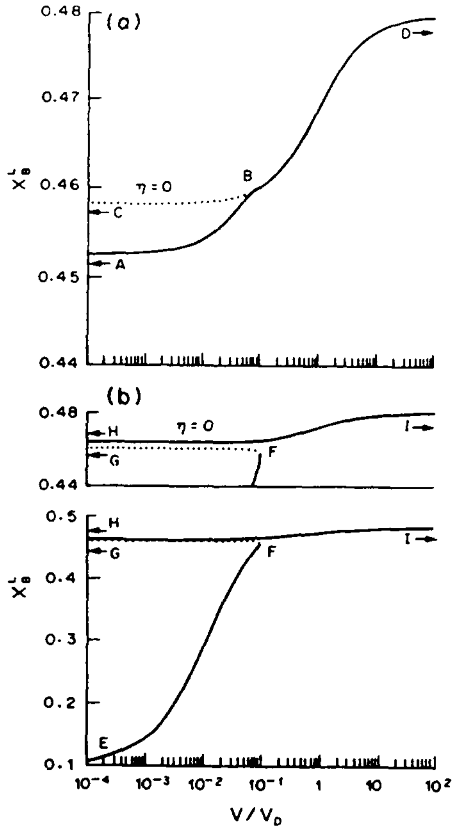

Fig. 10. Liquid composition at the interface x_B^L, as a function of dimensionless growth velocity V/V_D for $x_B^S = 0.48$ corresponding to Fig. 9.

monolayer are ultimately tied to the values of the diffusion coefficients in the solid (D_S), interface (D_i), and liquid (D_L). In general it is reasonable to assume that $D_S < D_i < D_L$. The present theory applies best when these differ by orders of magnitude. However, even if D_i approaches D_L, the assumption of complete mixing in the first liquid monolayer may only become suspect if the atom positions of each sublattice stays fixed laterally on the liquid–solid interface during growth. This could happen in some crystallographic orientations of some crystal structures, e.g. growth of a chemically layered structure edgewise into the melt. In this case one would expect disorder trapping at lower solidification rates then predicted by this theory. Relaxation of the assumption regarding the absence of lateral exchanges (ordering) in the first solid monolayer would increase the state of order at any velocity over that predicted by the theory. Ordering of the surface layer could be added to that which occurs in the bulk during solid state cooling to predict the state of order in a final (cold) solid. We have also assumed that at equilibrium the state of order of the surface layer is the same as the bulk solid. This assumption could be relaxed if necessary. The theory also has assumed that $Q_D^\alpha = Q_D^\beta$ or that the interdiffusion between the liquid and solid do not depend on the sublattice. This condition can easily be relaxed. One result of such a change would be that for solidification of a composition at a congruent melting maximum, x_B^L would not equal x_B^S except at $V = 0$ and $V = \infty$.

8.2. *Stability of solutions*

We next turn to a discussion of the mathematical stability of the solutions of the equations for the interface conditions. Solutions may be unstable in the sense that a small fluctuation in η at the interface during steady state growth will not decay back to the solution. Such unstable solutions cannot represent physically meaningful situations. This stability may be viewed in the context of bifurcation theory [34], which describes the change in the mathematical stability of solutions near intersections and turning points. For example the two solutions $\eta = 0$ and $\eta \neq 0$ always intersect at $V/V_D \approx -\Omega_1/2RT_m^0 - 1$, which is a positive and negative value of V/V_D for case I and II respectively. At this intersection point the stability of the $\eta = 0$ solution must change. The stability of the various solutions can be inspected by replacing equation [21], which applies only for the steady state, with the time dependent form of the flux balance. For $x_B = 0.5$

$$\frac{d\eta}{dt} = -\frac{V_D}{2\lambda}\left\{2\frac{V}{V_D}\eta - (1-\eta) + (1+\eta) \times \exp\left[\frac{\Omega_1\eta + 8\Omega_2\eta^3}{RT}\right]\right\} \quad (33)$$

which is the correct form for $\eta \geqslant 0$ only. The results already presented are for the steady state where the *LHS* is zero. If at constant V a positive perturbation of n away from the steady state solution makes the *RHS* of equation (33) negative, then $d\eta/dt < 0$, the perturbation decays, and that portion of the solution is stable. Using this method the $\eta = 0$ solution can be shown to be stable only if $V/V_D > -1 - \Omega_1/2RT_m^0$. Similarly the stability of the $\eta \neq 0$ solutions were inspected. In case I the $\eta \neq 0$ solution is always stable whereas the $\eta \neq 0$ solution for case II changes from stable to unstable at the turning point. The stable branch has negative slope in the η vs V/V_D plot.

The existence of the turning point for the solidification of an ordered phase that differs from its disordered phase by a first order transition is directly related to the shape of the free energy curve shown schematically in Fig. 1(b), particularly the maximum at non-zero η.The turning point leads to the prediction that η, as well as compositions (for $x_B^S \neq 0.5$), at the interface would suffer a discontinuous jump as the growth rate increases.

8.3. *Interface mobility*

The slope of the curves for the congruent composition in Fig. 7, dT/dV are worthy of some discussion The slope relates a simple measure of the departure from equilibrium required to cause growth at various rates. It can be seen that the slope is small near $V = 0$

and whenever $\eta = 0$. At velocities where η is changing, the slope is much steeper, i.e. the interface becomes more "sluggish". An expression for dT/dV can be found for $x_B = 0.5$ for Case I by differentiation of equations (14) and (22). An approximate expression for the slope is $-(RT^2/\Delta H)(1/V_C + \phi(\eta)/V_D)$ where ΔH is the enthalpy difference between the melt and the solid that is forming and ϕ is a complicated function of η. The function ϕ changes from zero when $\eta = \eta_e$, to order unity for intermediate η, and back to zero when $\eta = 0$. Thus the growth kinetics are controlled by V_C when the solid is disordered or when the solid has near equilibrium order at small V. For intermediate η, the growth kinetics are controlled by V_D if $V_C/V_D = 10^3$. Thus the overall growth kinetics for an intermetallic can be short-range diffusion controlled (and thus more sluggish) in some velocity ranges even when the crystallization reaction is collision limited.

8.4. Applications

The present theory can provide some guidance in selecting intermetallic compounds that respond to rapid solidification to produce phases with non-equilibrium composition or state of order. The former may be useful to provide the supersaturation necessary to form a controlled scale of precipitation by subsequent heat treatment. Non-equilibrium order produced by solidification will often be followed by rapid ordering during solid state cooling. The fine antiphase domains structures produced by this process can provide unusual starting materials for subsequent heat treatment [35].

Indeed the predictions of equation (32) can be crudely compared with two experimental results on melt spinning of phases, which if disordered would be f.c.c. Huang and Hall [16] have shown that normally $L1_0$ TiAl with ~60 at.% Al solidified as f.c.c. during melt spinning. On the contrary $D0_{22}$ Al_3Nb was not altered by melt spinning [36]. For materials parameters we chose V_D as 200 cm/s ($D_i = 6 \times 10^{-6}\,cm^2\,s^{-1}$, $\lambda = 3 \times 10^{-8}$ cm) and T_C/T_m^0 as 1.3 and 2.0 for TiAl and Al_3Nb respectively [37], the latter indicating the highly ordered nature of the line compound Al_3Nb. Estimates of the critical velocity for complete disordering of 60 and 200 cm/s respectively are then obtained. Only the former velocity is easily achieved by melt spinning. Strictly one needs the result for the critical velocity for solids with an order disorder transition that is first order and for 3 to 1 ideal stoichiometry for this case.

Quantitative predictions by this theory require good thermodynamic models for the phases of interest as well as values for the kinetic parameters V_C and V_D. Unfortunately, measurements of equilibrium order parameter are often not available, especially for materials of technological interest with high melting points. Thus the data base of thermodynamic modelling is poor. Additionally *separate* thermodynamic free energy functions are often used for the ordered and the disordered phases in many phase diagram evaluations. The present theory required a single potential that represents both the ordered and disordered phase. It is important to note that many complex ordered phases such as σ phases bear no resemblance to simple disordered structures and thus no single solid free energy can represent both ordered and disordered phases. The elimination of such phases by rapid solidification and replacement by a simpler disordered phase is not an example where this theory is applicable. Classical concepts of nucleation and growth competition must be applied to these situations. Values of V_C and V_D can only be crudely estimated at present. Experiments on combined solute trapping and disorder trapping by pulsed laser melting using the transient conductance method to measure interface velocities [38] may provide insight into these parameters. Ordering during solid state cooling must be subtracted from final values to obtain the values produced by the interface itself.

Three features are amenable to measurement. Extremely fine antiphase domains should be present if the critical velocity has been exceeded. Also the abrupt behavior of the composition shown in Fig. 10 when η goes to zero may produce unusual microstructural features. Finally, a transient conductance measurement of the resistivity of the solid within nanoseconds of solidification [38] may be a ready indicator of its order parameter before solid state changes can occur.

Acknowledgements—Discussions with S. R. Coriell and J. W. Cahn are greatly appreciated. This research was supported by DARPA (Order No. 6065) for W.J.B. and ONR (Contract No. N00014-88-K-0548) and a grant from B.P. America for M.J.A.

REFERENCES

1. M. J. Aziz, *J. appl. Phys.* **53,** 1158 (1982).
2. M. J. Aziz and T. Kaplan, *Acta metall.* **36,** 2335 (1988).
3. L. M. Goldman and M. J. Aziz, *J. Mater. Res.* **2,** 524 (1987).
4. K. A. Jackson, in *Surface Modification and Alloying by Laser Ion and Electron Beams* (edited by J. M. Poate, G. Foti and D. C. Jacobson), p. 62. Plenum, New York (1983).
5. G. H. Gilmer, *Mater. Res. Soc. Symp. Proc.* **13,** 249 (1983).
6. J. C. Baker, *Interfacial partitioning during solidification*, Ph.D. thesis, MIT (1970). See also J. W. Cahn, S. R. Coriell and W. J. Boettinger, in *Laser and Electron Beam Processing of Materials* (edited by C. W. White and P. S. Peercy), p. 89. Academic Press, New York (1980).
7. V. V. Voronkov and A. A. Chernov, *Soviet Phys. Crystallogr.* **12,** 186 (1967).
8. H. Pfeiffer, *Physica status solidi (a)* **99,** 139 (1980).
9. D. E. Temkin, *Soviet Phys. Crystallogr.* **17,** 405 (1972).
10. M. J. Aziz, J. Y. Tsao, M. O. Thompson, P. S. Peercy and C. W. White, *Phys. Rev. Lett.* **56,** 2489 (1986).
11. M. J. Aziz and C. W. White, *Phys. Rev. Lett.* **57,** 2675 (1986).
12. C. C. Koch, J. A. Horton, C. T. Liu, O. B. Cavin and

J. O. Scarbrough, in *Rapid Solidification Processing: Principles and Technologies* (edited by R. Mehrabian), Vol. 3, p. 264. National Bureau of Standards, Washington, D.C. (1982).
13. A. Inoue, T. Masumoto, H. Tomioka and N. Yano, *Int. J. Rapid Solidif.* **1**, 115 (1984).
14. S. C. Huang, E. L. Hall, K. M. Chang and R. P. Laforce, *Metall. Trans.* **A17**, 1685 (1986).
15. W. J. Boettinger, L. A. Bendersky, F. S. Biancaniello and J. W. Cahn, *Mater. Sci. Engng* **8**, 273 (1988).
16. S. C. Huang and E. L. Hall, *Mater. Res. Soc. Symp. Proc.* **133**, 373 (1989).
17. J. S. Langer and R. F. Sekerka, *Acta metall.* **23**, 1225 (1975).
18. E. A. Brener and D. E. Temkin, *Soviet Phys. Crystallogr.* **28**, 7 (1983).
19. T. Meister and H. Muller-Krumbhaar, *Phys. Rev. Lett.* **51**, 1780 (1983).
20. P. R. Harrowell and D. W. Oxtoby, *J. chem. Phys.* **86**, 2932 (1987).
21. A. A. Chernov, *Soviet Phys. Uspekhi* **13**, 101 (1970).
22. A. A. Chernov, *Soviet Phys. JETP* **26**, 1182 (1968).
23. T. A. Cherepanova, A. Y. Shirin and Y. T. Borisov, *Soviet Phys. Crystallogr.* **22**, 147 (1977).
24. P. Bennema and J. P. Yan der Eerden, *J. Cryst. Growth* **42**, 201 (1977).
25. T. A. Cherepanova, J. P. Yan der Eerden and P. Bennema, *J. Cryst. Growth* **44**, 537 (1978).
26. S. R. Coriell and D. Turnbull, *Acta metall.* **30**, 135 (1982).
27. C. A. MacDonald, A. M. Malvezzi and F. Spaepen, *J. appl. Phys.* **65**, 129 (1988).
28. J. Q. Broughton, G. H. Gilmer and K. A. Jackson, *Phys. Rev. Lett.* **49**, 1496 (1982).
29. T. Kaplan, M. J. Aziz and L. J. Gray, *J. chem. Phys.* **90**, 1133 (1989).
30. J. C. Baker and J. W. Cahn, in *Solidification*, p. 23. Am. Soc. Metals, Metals Park, Ohio (1971).
31. D. Turnbull, *J. Phys. Chem.* **66**, 609 (1962).
32. P. J. Vergano and D. R. Uhlmann, *Phys. Chem. Glasses* **11**, 30 (1970).
33. J. R. Manning, *Diffusion Kinetics for Atoms in Crystals*, p. 180. Van Nostrand, Princeton, N.J. (1968).
34. see for example, G. Iooss and D. D. Joseph, *Elementary Stability and Bifurcation Theory*. Springer, Berlin (1980).
35. L. A. Bendersky, P. W. Voorhees, W. J. Boettinger and W. C. Johnson, *Scripta metall.* **22**, 1029 (1988).
36. W. J. Boettinger, L. A. Bendersky and F. S. Biancaniello, Nat. Inst. Stnds Tech., Gaithersburg, Md (1988), unpublished research.
37. Y. A. Chang and J.-C. Lin, Univ. of Wisconsin-Madison, Madison, Wis. (1989), private communication.
38. J. Y. Tsao, S. T. Picraux, P. S. Peercy and M. O. Thompson, *Appl. Phys. Lett.* **48**, 278 (1986).

INVESTIGATION OF B2 AND RELATED PHASES IN THE Ti-Al-Nb TERNARY SYSTEM

LEONID A. BENDERSKY AND WILLIAM J. BOETTINGER
Metallurgy Division, National Institute of Standards and Technology, Gaithersburg, MD 20899, USA

ABSTRACT

Alloy compositions around Ti_2AlNb were studied to establish phase equilibria and transformations during cooling from 1100°C and 1400°C. In addition to general results obtained on a wide range of compositions, which include evidence for a broad B2 phase field, transformation of BCC Ti_4Al_3Nb to a phase with an omega-type structure is reported. Detailed analysis indicates that this phase has the $B8_2$ structure after annealing at 700°C.

INTRODUCTION

Titanium aluminides (Ti_3Al and TiAl) with Nb additions have received considerable attention as potential low density, high strength and creep-resistant materials for high temperature application. Because the presence of BCC and BCC-related phases in these alloys seems to have an important role in their mechanical properties, in-depth studies of the BCC phase field are necessary. Surprisingly, the phase equilibria in this ternary system are poorly understood. The only detailed studies are for alloys of Ti_3Al with Nb substitution for Ti up to 20 at% by Strychor et al.[1] and Banerjee et al. [2,3]. Both show the existence of a high temperature BCC or B2 phase which generally transforms during cooling to an ordered hexagonal DO_{19} phase. The variety of observed microstructures reported shows extreme sensitivity of the alloys to the details of heat treatment. Probably because of this, the two studies have reported quite different results. Banerjee et al.[3] found that upon slow cooling both B2 and DO_{19} phases transform partially to an orthorhombic phase with symmetry Cmcm. They suggest a structural relationship between this phase and the hexagonal DO_{19} phase. No such phase was observed by Strychor et al. [1]. Instead, an ordered omega phase was observed. The phase precipitates from the retained B2 phase during low temperature annealing. Arguments about further transformation of the omega phase to a $B8_2$ (Zr_2Al) phase were also presented.

Recently we have begun an experimental study on phase equilibria and phase transformations in the ternary Ti-Al-Nb system. In order to cover a wide range of compositions, five different alloys including and surrounding Ti_2AlNb were chosen for study. In this paper we present preliminary results on possible equilibrium phases at 1400°C and 1100°C for these alloys. The focus of the paper is on the alloy with the Ti_4Al_3Nb composition for which a complex transformation of BCC to an omega-type structure was observed.

EXPERIMENTAL PROCEDURE

Alloys with compositions Ti_5Al_2Nb(alloy #3), Ti_2AlNb(#30), Ti_4Al_3Nb(#4), $Ti_3Al_2Nb_3$(#2) and Ti_4AlNb_3(#1) were prepared by arc melting. In excess of ten remelts were necessary to ensure mixing of the components. Cast buttons were homogenized at 1400°C for three hours in a furnace under 2/3 atm gettered Ar. It was found necessary to rest the samples on a Y_2O_3 coated Al_2O_3 substrate to prevent reaction with Al_2O_3. Heat treatments at 1100°C for 4 days were performed after the 1400°C treatment by lowering the furnace temperature. Cooling to room temperature was performed by lowering the samples out of the hot zone of the furnace into a lower chamber. The cooling rate was estimated to be about 400°C/min.

Mat. Res. Soc. Symp. Proc. Vol. 133 ©1989 Materials Research Society

RESULTS

Microstructure of Samples Heat Treated at 1400°C

Optical metallography of all samples cooled from 1400°C reveals the elimination of the dendritic microsegregation of the cast structure and the presence of very coarse grains (~2 mm) of an apparent single phase. As TEM examination shows, however, the high temperature phase is transformed to other phases during cooling. The resultant microstructures are fine and not resolved by optical metallography except for alloy #3.

For alloy #3 (Fig.1a) the microstructure consists of a martensite-type morphology with plates of the DO_{19} phase related to each other by the Burgers orientation relationship. This microstructure is well known for Ti alloys [1] and indicates a transformation from the high temperature BCC phase to the DO_{19} phase during cooling. The presence of a high density of APBs (anti-phase boundaries) in the DO_{19} phase suggests that the first step of the transformation was the formation of the disordered hexagonal phase.

For alloy #30 the microstructure consists of a B2 matrix phase with a small fraction transformed to polydomain plates of the DO_{19} phase (Fig.1b). The microstructure appears similar to the initial stage of the same transformation for the #3 alloy. The BCC phase has B2 ordering and strong diffuse streaking along 110 directions (Fig.2a). No APBs due to the B2 ordering were observed. In two-beam imaging the matrix shows strain contrast referred to in the literature as "tweed"[1].

Alloy #2 has large grains of the B2 phase showing diffraction effects similar qualitatively to that of the alloy #30 matrix. No APBs due to the BCC/B2 ordering or other phases were observed.

Alloy #1 also has a single phase B2 microstructure. The only difference compared to the #2 and #30 alloys is that the B2 ordering reflections are noticeably weaker (Fig.2b).

Alloy #4 has a microstructure consisting of small (~0.2 μm) domains (Fig.3a) which are clearly the result of solid state transformation from a high temperature BCC (or B2) phase during cooling. Selected area diffraction with a large aperture from a large number of domains shows patterns with strong fundamental and superlattice reflections of the B2 phase - e.g. <110> and <111> cubic orientations in Fig.4a,b. Reflections in addition to those of the B2 phase can be identified as belonging to four rotational domains of an omega phase (hexagonal Bravais lattice: a=0.46 nm, c≈0.58 nm) with $\langle 111\rangle_{bcc}//[0001]_h$ and $(110)_{bcc}//(1120)_h$. The omega phase is ordered and has a "c" parameter twice that of the disordered phase. This transformation will be discussed in more detail in the Discussion.

Microstructure of Samples Heat Treated at 1100°C

The microstructure of samples cooled from a 4 day heat treatment at 1100°C observed by optical metallography show that specimens #3, 30 and 1 are in a single phase region at 1100°C. According to TEM observation, the phase is similar to that at 1400°C. For the other two specimens, #2 and 4, precipitates coarse enough to be considered at equilibrium at 1100°C were observed. The second phases were identified by electron diffraction as the sigma phase (tetragonal $AlNb_2$) for specimen #2, and the DO_{19} phase (hexagonal Ti_3Al) for specimen #4. The compositions of these phases and the matrix were measured by SEM microprobe and shown by the tie-lines in Fig.5b. According to TEM observation, the matrix phases are similar to those observed for the 1400°C annealed alloys.

DISCUSSION

According to the results presented in the previous section, the BCC or B2 phase is the high temperature phase at both 1400°C and 1100°C. Fig.5 shows the estimated single phase field of this phase for the temperatures studied using our data and the general shape of the BCC field obtained from preliminary thermodynamic calculation of the Ti-Al-Nb ternary diagram [4]. For all five alloys, B2 order can not be ruled out at temperature. For alloys #1, 2 and 30 the ordered B2 phase was observed after cooling. Since no APBs from B2 ordering were observed for these specimens, it is possible that the B2 phase is an equilibrium phase at both temperatures. We have thus sketched a region of the BCC field in which B2 order exists in Fig.5. However it is also possible that the APBs were annealed out during the relatively slow cooling in our experiments, and the ordering temperature is lower than 1100°C. Estimates of the antiphase domain coarsening rate are too slow to support this conjecture. High cooling rate quenching or high temperature X-ray diffraction experiments are now in progress to establish the ordering temperature.

For the composition of alloy #3, the equilibrium phases at 1100°C have been reported as B2 and DO_{19}[3]. Our results suggest that the equilibrium is single phase BCC. In our alloy #3 the DO_{19} phase forms only during cooling from 1100°C and has a high density of APBs. The transformation path is thus BCC to hex.(disord.) to DO_{19}. Our results also suggest that the BCC/B2 ordering only occurs in the absence of the BCC to HEX transformation and thus is metastable at this composition and occurs below 1100°C. Possibly small differences in composition or heat treatment temperature may have caused our discrepancy with [3].

For alloy #4 the following arguments about the nature of BCC phase ordering and phase transformation could be applied. According to Strychor et al. [1], the B2 phase transforms by collapse of (111) planes to the ordered omega phase which subsequently orders to the hexagonal $B8_2$ phase (actually it is disordering since the space group of the $B8_2$ ($P6_3/mmc$) is a supergroup of the omega phase(P3m1)). The arguments of [1] are based on the presence of 1100 reflections of omega at $1/3\langle 112\rangle_{bcc}$ which have zero structure factor for both the ordered and disordered omega phase. These reflections are also observed for our alloy #4 (see Fig.4b). Dark-field imaging with the 1100 reflection shows only one rotational variant which includes three translational variants separated by well-imaged interfaces (Fig.3). No BCC or B2 phase was observed between the domains. The dark-field imaging plus tilting to an orientation where only a hh00 row of reflections is excited shows that the observed non-zero 1100 structure factor is not the result of double diffraction.

However the 1100 reflection is not forbidden by the P3m1 space group symmetry [5], and has zero structure factor only for particular states of order inherited from the BCC or B2. Deviations from that order (e.g. different occupancy on sites 1b and 2d) will change the 1100 structure factor to non-zero. An example can be a ternary structure of the Ti_3Al_2Nb stoichiometry with Ti on 1a and 2d, Nb on 1b and Al on 2d sites. Therefore information additional to that presented by [1] is required to confirm the existence of the $B8_2$ structure in the Ti-Al-Nb system. For this purpose, convergent beam electron diffraction (CBED) could be used in order to distinguish between the P3m1 and the $P6_3/mmc$ (of the $B8_2$ phase) space groups. This was applied for alloy #4 which was annealed for 26 days at 700°C to produce domains large enough for good CBED. Results from a single domain show that the [0001] zone axis has the 6mm whole pattern symmetry, and that the [1120] zone axis has the 2mm whole pattern symmetry (Fig.6). These results are in agreement with the hexagonal $P6_3/mmc$ space group of the $B8_2$ phase rather than with the trigonal P3m1 space group (for this group for the same zone axes the whole pattern symmetry is 3m and 2, respectively [6]). Additional confirmation of this result was obtained by showing that the 0001 reflection is kinematically forbidden. This was shown by tilting along the 000ℓ row and observation of the disappearance of 000ℓ (with odd ℓ) reflections.

CONCLUSIONS

1. A large BCC phase field was confirmed to exist at 1100°C and 1400°C.
2. B2 order was found for a large composition range and appears to be the equilibrium at 1100°C and 1400°C.
3. A hexagonal $B8_2$ phase, which is structurally related to ordered omega, is probably a low temperature equilibrium phase (700°C) with composition close to Ti_4Al_3Nb. It is questionable if the formation of athermal omega precedes the BCC to $B8_2$ transformation.
4. The existence of high temperature BCC to B2 ordering for this composition remains an open question.

ACKNOWLEDGEMENT

The support of the Defense Advanced Project Research Agency under Order #6065 is appreciated. We thank F.S.Biancaniello and M. Williams for the alloy and TEM specimen preparation and Dr. A. Shapiro for the microprobe analysis.

REFERENCES

1. R.Strychor, J.C.Williams and W.A.Soffa, Met. Trans., 19A, 225 (1988).
2. D.Banerjee, T.Nandi and A.K.Gogia, Scripta Met., 21, 597 (1987).
3. D.Banerjee, A.K.Gogia, T.K.Nandi and V.A.Joshi, Acta Met., 36, 871 (1988).
4. U.R.Kattner, NIST, Gaithersburg, MD, 1988, unpublished research.
5. Inter. Tables for Cryst., Vol.A, T. Hahn (ed.), D. Reidel Publishing Co., Dodrecht (1987).
6. B.F.Buxton, J.A.Eades, J.W.Steeds and G.M.Rackham, Phil. Trans., 281, 171 (1976).

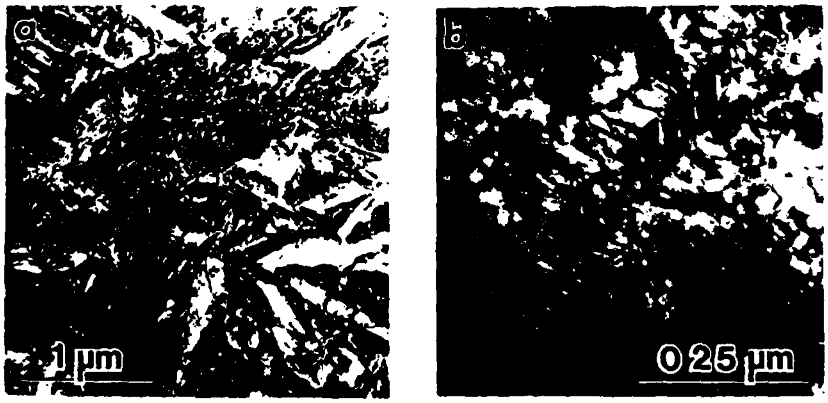

FIG.1 TEM micrographs of the microstructure of specimens cooled from 1400°C temperature. a) alloy #3 with martensite-type morphology of the DO_{19} phase. b). alloy #30 with the B2 phase matrix and a polydomain plate of the DO_{19} phase. Similar microstructures are observed for specimens cooled from 1100°C.

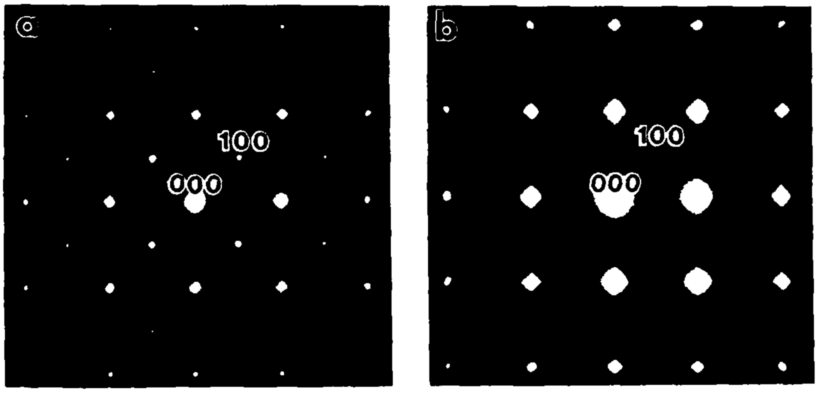

FIG.2 SAD patterns from alloys #2 (a) and #1 (b) cooled from 1400°C showing B2 order and <110> diffuse streaks. Specimens cooled from 1100°C are similar.

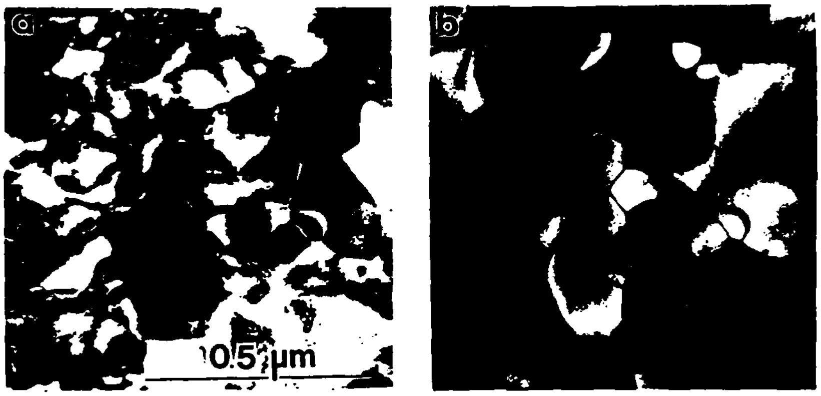

FIG.3 TEM bright-field (a) and dark-field (b) of #4 alloy cooled from 1400°C. Dark-field shows only one (out of four rotational domains of the omega-type phase. Interfaces within the domains separate translational domains.

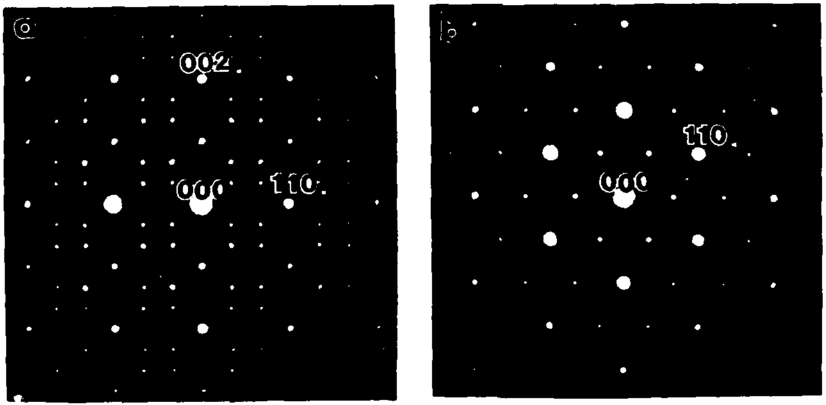

FIG.4 SADP patterns typical for the alloy #4 cooled from either 1400°C or 1100°C. a) $[110]_{bcc}$ zone axis; b) $[111]_{bcc}$ zone axis.

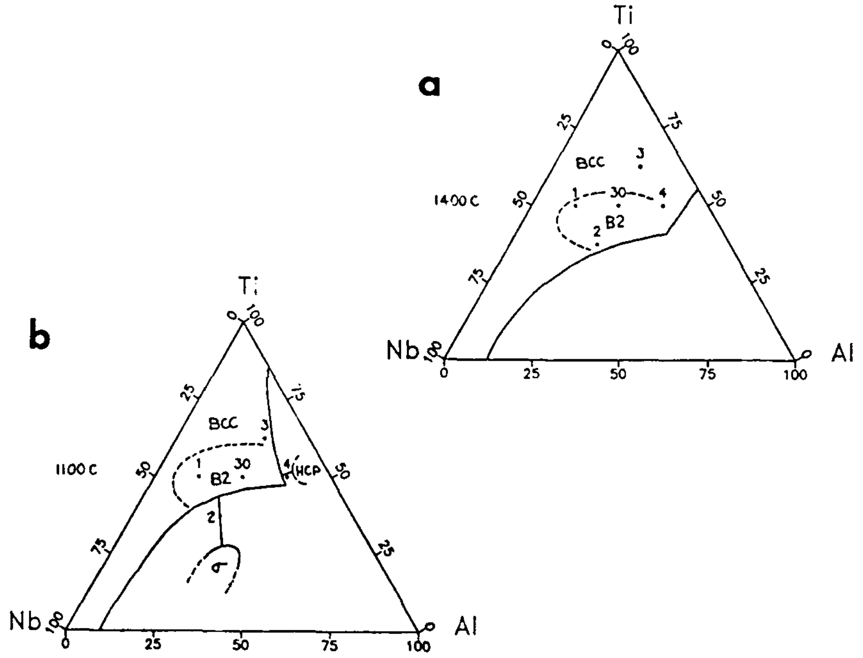

FIG.5 The estimated single phase field of the BCC phase at (a) 1400°C and (b) 1100°C. Dashed line shows a possible field where the BCC phase is ordered to B2. Tie lines to the sigma and hcp phases determined by microprobe are shown in (b).

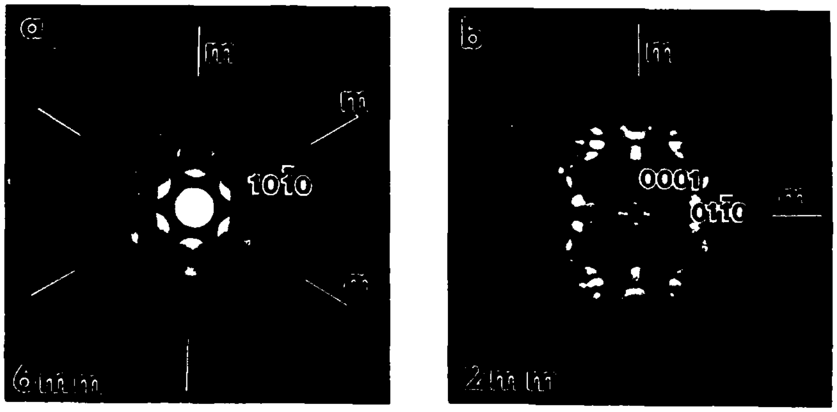

FIG.6 CBED from a single domain of alloy #4 anealed at 700°C for 26 days at [0001] (a) and [1120] (b) zone axis orientations showing 6mm and 2mm whole pattern symmetry consistent with the $P6_3/mmc$ space group of $B8_2$ structure.

OMEGA-RELATED PHASES IN A Ti-Al-Nb ALLOY

Leonid A. Bendersky and William J. Boettinger

Metallurgy Division, National Institute of Standards and Technology,
Gaithersburg, MD 20899

Study of phase equilibria in the Ti-Al-Nb system is often complicated by the possibility of rapid ordering reactions of a chemical or displacive type during cooling from high temperatures. In the present study we have investigated the decomposition of the high temperature B2 phase of composition Ti-37.5at%Al-12.5at%Nb into "omega-type" phases during either cooling or low temperature annealing. Formation of an "omega-type" phase from the high temperature B2 matrix of composition Ti-27.8at%Al-11.7at%Nb was observed previously by [1]. If the "omega-type" phase forms by pure displacive ordering, i.e. by collapse of (111) plane pairs of the B2 phase, the resulting structure will be as shown in Fig.1a (termed ω'). The chemical order of the ω' phase is directly inherited from the B2 structure. The space group of the ω' phase is P3ml (#164). The same authors [1] suggested a secondary transformation of the ω' phase to another omega-type phase with the B8$_2$ structure shown in Fig.1b. The space group for the B8$_2$ structure is hexagonal P6$_3$/mmc (#194) with reflection conditions such that the 1100 reflection is present, but the 0001 (or $000\ell, \ell=2n+1$) is absent.

C.12

This note confirms the presence of the phase with the B8$_2$ structure as an equilibrium low temperature phase using convergent beam electron diffraction (CBED). However the mechanism of the low temperature decomposition of the B2 phase is more complex than was suggested by Strychor et al. [1]; viz., an intermediate trigonal phase, ω'' is formed with a structure shown in Fig.1c.

X C.7

Fig.2a,b show convergent beam electron diffraction (CBED) patterns of an omega-type phase annealed at 700 C for one month. The whole pattern symmetry is 6mm for the [0001] orientation and 2mm for the [11$\bar{2}$0] orientation. These whole pattern symmetries determine unambiguously that the phase has hexagonal point group symmetry 6/mmm (see tables in [2]). The absence of odd 000ℓ reflections in a diffraction condition obtained by exciting only one row suggests that they are kinematically forbidden. Observation of dynamic extinction in a kinematically forbidden 0001 reflection in the form of a black cross (Fig.2b) for the [11$\bar{2}$0] zone axis, (a result of the simultaneous presence of a screw axis and a glide plane) can be explained only by the space group P6$_3$/mmc. This result seems to suggest the existence of an equilibrium low temperature TiAlNb B8$_2$ phase (in equilibrium with D019 and L1$_0$ phases, as will be shown elsewhere [3]).

All specimens cooled from high temperature go through a rapid phase transformation during cooling from the B2 to a different "omega-type" phase. The phase has selected area diffraction patterns indistingushiable from the B8$_2$ phase (Fig.3). Using microdiffraction it was shown that odd 000ℓ reflections are present (Fig.4). The same is true for all hh00 reflections. Therefore, the phase has neither the B8$_2$ nor the ω' structure. The diffraction data fits the proposed ternary ω'' phase shown on Fig.1c. X-ray single crystal diffraction results seem to confirm this [3].

ACKNOWLEDGEMENT

The support of the DARPA under Order #6065 is appreciated.

REFERENCES

1.R.Strychor, J.C.Williams and W.A.Soffa, Met.Trans., 19A, 225 (1988).
2.B.F.Buxton, J.A.Eades, J.W.Steeds and G.M.Rackham, Phil.Trans., 281, 171 (1976).
3.L.A.Bendersky, W.J.Boettinger and C.B.Shoemaker, to be published.

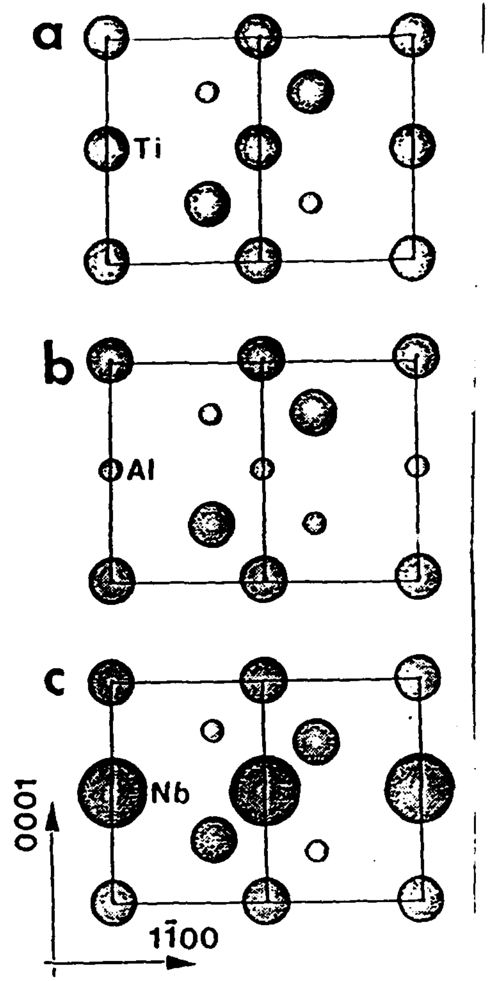

Fig.1 Projected structure of one hexagonal unit cell of the ω'(a); $B8_2$(b); ω"(c) phases in the $[11\bar{2}0]$ direction.

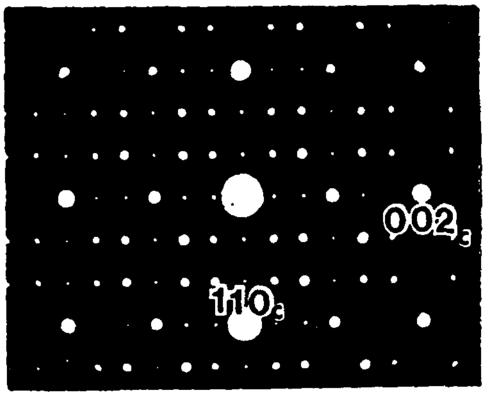

Fig.3 SAD pattern from the cooled specimen at $<110>_{cub}$ orientation. The same pattern was observed for the annealed specimen.

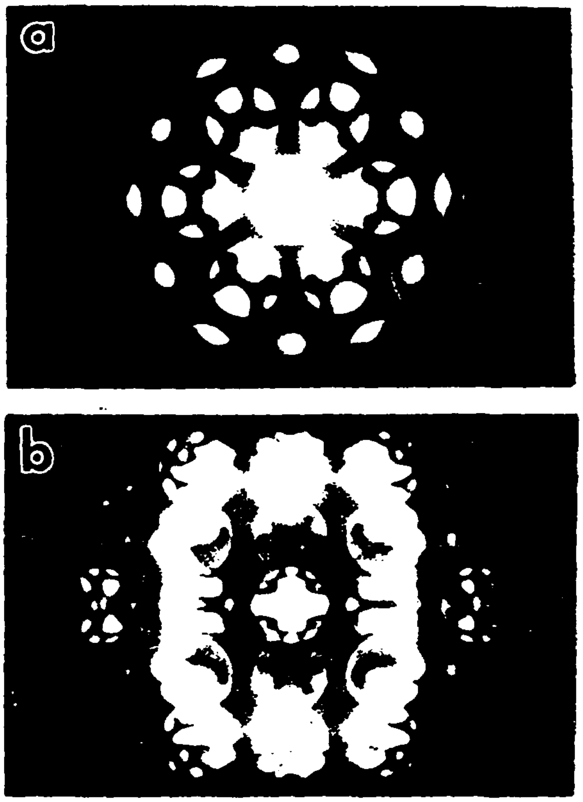

Fig.2 CBED patterns at [0001] (a) and $[11\bar{2}0]$ (b) zone axis orientations of an annealed specimen. The $P6_3/mmc$ space group of $B8_2$ structure can be derived.

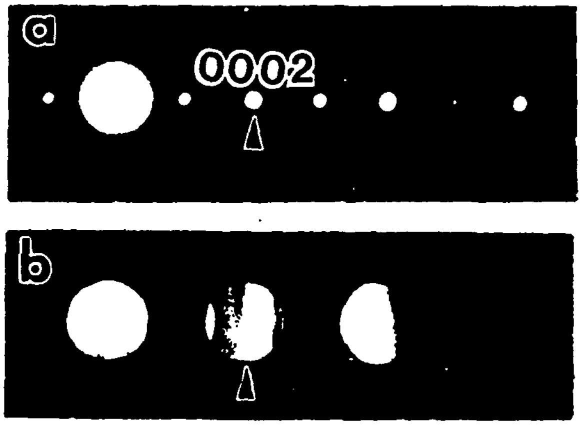

Fig.4 SAD(a) and CBED(b) patterns of a row of 0001 reflections showing the presence of odd reflections for the cooled specimen.

Acta metall mater. Vol. 38, No. 6, pp. 931-943, 1990
Printed in Great Britain

0956-7151/90 $3.00 + 0.00
Pergamon Press plc

THE FORMATION OF ORDERED ω-RELATED PHASES IN ALLOYS OF COMPOSITION Ti_4Al_3Nb

L. A. BENDERSKY, W. J. BOETTINGER, B. P. BURTON and F. S. BIANCANIELLO
Metallurgy Division, National Institute of Standards and Technology, Gaithersburg, MD 20899, U.S.A.

and

C. B. SHOEMAKER
Department of Chemistry, Oregon State University, Corvallis, OR 97331, U.S.A.

(*Received* 22 *November* 1989)

Abstract—During cooling of an alloy of composition Ti_4Al_3Nb from a B2 phase field above 1100°C, a metastable trigonal ($P\bar{3}m1$) ω-related phase, designated ω'', forms along with small amounts of $D0_{19}$ and $L1_0$ phases. The ω'' phase exhibits partial collapse of 111 planes and reordering relative to its B2 parent. An apparently equilibrium low temperature phase with the $B8_2$ structure was found after 26 days of annealing at 700°C. Both ω'' and $B8_2$ structures were verified by means of transmission electron microscopy and by single crystal X-ray diffraction. The latter permitted detailed analysis of the collapse parameters and site occupancies. The observed transformation path, $B2(Pm\bar{3}m) \rightarrow \omega''(P\bar{3}m1) \rightarrow B8_2$ $(P6_3/mmc)$, occurs in two steps. The first involves a subgroup transition during cooling that is primarily displacive with reordering consistent with the trigonal symmetry imposed by the ω-collapse. The second involves a supergroup transition during prolonged annealing that is primarily replacive and constitutes a chemical disordering. The direct equilibrium transformation, $B2 \rightarrow B8_2$, without the formation of an intermediate trigonal phase, can only occur by a reconstructive transformation.

Résumé—Pendant le refroidissement d'un alliage de composition Ti_4Al_3Ab à partir de la phase B2 au dessus de 1100°C, une phase rhomboédrique métastable ($P\bar{3}m1$) reliée à la phase ω, et appelée ω'', se forme en même temps que de petites quantités des phases $D0_{19}$ et $L1_0$. La phase ω'' révèle un effondrement partiel des plans {111} et une remise en ordre par rapport à la phase mère B2. Une phase de structure $B8_2$, apparement en équilibre à basse température, est observée aprés 26 jours de recuit à 700°C. Les deux structures ω'' et $B8_2$ sont vérifiées par microscopie électronique en transmission et par diffraction de rayons X. Cette dernière technique permet une analyse détaillée des paramètres d'effondrement et de l'occupation des sites. La transformation observée $B2(Pm\bar{3}m) \rightarrow \omega''(P\bar{3}m1) \rightarrow B8_2(P6_3/mmc)$, se produit en deux étapes. La première implique une transition de sous-groupe pendant le refroidissement, qui est essentiellement displacive, avec une remise en ordre compatible avec la symétrie rhomboédrique imposée par l'effondrement de ω. La deuxième implique une transition de sur-groupe pendent le recuit prolongé, qui constitue un désordre chimique. La transformation directe d'équilibre, $B2 \rightarrow B8_2$, sans formation de phase rhomboédrique intermédiaire, ne peut se produire que par une transformation reconstructive.

Zusammenfassung—Während des Abkühlens der Legierung Ti_4Al_3Nb aus einem B2-Phasenfeld oberhalb 1100°C bildet sich eine metastabile trigonale ($P\bar{3}m1$)-ω-verwandte Phase, bezeichnet mit ω'', zusammen mit kleinen Mengen der $D0_{19}$- und $L1_0$-Phasen. Die ω''-Phase weist teilweise Kollaps der 111-Ebenen und Umordnung verglichen zu ihren B2-Eltern auf. Eine offenkundig bei tiefer Temperatur im Gleichgewicht stehende Phase mit $B8_2$-Struktur wurde nach Auslagerung bei 700°C für 26 Tage gefunden. Die ω''- und die $B8_2$-Struktur wurden mittels Durchstrahlungselektronenmikroskopie und Einkristall-Röntgenbeugung nachgewiesen. Die Röntgenuntersuchung ermöglichte auch die genaue Bestimmung der Kollapsparameter und der Besetzung der Gitterplätze. Der beobachtete Weg der Umwandlung $B2(Pm\bar{3}m) \rightarrow \omega''(P\bar{3}m1) \rightarrow$ $B8_2(P6_3/mmc)$ läuft in zwei Schritten ab. Der erste betrifft den Übergang einer Untergruppe während des Abkühlens, welcher erster Linie displaziv mit Umordnung ist, dieser ist verträglich mit der durch den ω-Kollaps aufgezwungenen trigonalen Symmetrie. Der zweite Schritt umfaßt den Übergang einer Übergruppe während der langen Auslagerung; dieser ist primär replaziv und stellt eine chemische Entordnung dar. Die direkte Gleichgewichtsumwandlung $B2 \rightarrow B8_2$, ohne Bildung einer trigonalen Zwischenphase, kann nur durch eine rekonstruktive Umwandlung erfolgen.

1. INTRODUCTION

Titanium aluminides (Ti_3Al and TiAl) with Nb additions have received considerable attention as potential low density, high strength and creep resistant materials for high-temperature applications. The development of optimum properties will require thermomechanical processing that is based on a complete knowledge of the phase transitions in this system.

Phase equilibria in the Ti–Al–Nb system are poorly understood because of the limited number of systematic studies, and because of the inherent complexity of the phase relations. With the exception of [1], detailed studies of this system have been conducted primarily for Ti_3Al alloys with Nb substitutions of up to 30 at.% for Ti, i.e. along the Ti_3Al-Nb_3Al pseudobinary section [2–7]. All of these studies report the existence of a high temperature b.c.c. or B2 phase over this composition range. Cooling a sample from the high temperature b.c.c. or B2 field, or annealing at low temperature, can produce various phases and microstructures depending upon the Nb content, the details of heat treatment or both. Strychor *et al.* [2] have shown that at low Nb content (< 5 at%), the b.c.c. phase transforms martensitically to an h.c.p. α' phase during quenching. During quenching of alloys with higher Nb content (5–17 at.%), the b.c.c. phase orders chemically to the B2 structure and then partially transforms to yield an "ω-type" phase in the B2 matrix. After aging this phase was identified as having the $B8_2$ structure. Banerjee *et al.* [3] reported an orthorhombic phase based on the composition Ti_2AlNb that was observed in a Ti-25 at.% Al-12.5 at.% Nb alloy slowly cooled from a high temperature $B2 + D0_{19}$ (α_2-phase) field. Several papers have addressed the phase equilibria involving this orthorhombic phase with the B2 and $D0_{19}$ phases [4–7].

The present paper is primarily concerned with the sequence of phase transitions by which a high temperature B2 ternary solution phase of composition Ti_4Al_3Nb is transformed into the low temperature $B8_2$ ω-related phase; transformation during both cooling and low temperature annealing are considered. The observed transformation sequence, $B2 \rightarrow \omega'' \rightarrow B8_2$, involves a metastable intermediate phase, ω'', that is of lower symmetry than either the initial B2 or final $B8_2$ states of the system. This phase has partially collapsed $(111)_{b.c.c.}$ planes and is reordered relative to B2 and thus involves both chemical (replacive) and displacive order/disorder transitions with strong coupling between the two. The observed phases are all structurally related, and therefore, the underlying thermodynamics of this transformation sequence are interpreted in terms of symmetry relations, and domain variant relations between the various phases.

The "ω-collapse" is a displacive phase transition that occurs in b.c.c. based systems. In it, two-thirds of the $(111)_{b.c.c.}$ layers "collapse" into double layers and the other third remain as single layers. In an elemental b.c.c. crystal or a disordered b.c.c. solution the sequence of $(111)_{b.c.c.}$ layers in a one dimensional representation (Table 1) transforms from ... A—A—A—A ... into ... A—A/A—A ... and $(111)_{b.c.c.}$ layers become $(0001)_h$ layers in the hexagonal or trigonal product phase. If *diffusionless* ω-collapse occurs in a chemically ordered B2 crystal with stoichiometry AB then the ω-related product phase (which is referred to as ω') will directly inherit B2 chemical order [Table 1, Fig. 1(a, b)]. That is, the B2 layer sequence ... A—B—A—B—A—B—A ... transforms into the trigonal ω-related sequence ... A—B/A - - - - B - - - - A/B—A ... and the hexagonal c-axis of the ordered ω-type phase is twice that of the disordered ω-phase. The double layers would have one neighboring single layer that is pure B and one that is pure A.

A diffusionless $B2 \rightarrow \omega'$ transition would yield a $P\bar{3}m1$ crystal with four distinct Wykoff sites (1a, 1b, $2d_1$ and $2d_2$) but only two distinct site occupancies (as in B2). Thus, ω' is inherently unstable with respect to changes in chemical order that lead to four rather than two distinct site occupancies because the inherited B2 occupancies are characteristic of a higher symmetry than $P\bar{3}m1$. The ω' configuration is an idealized state that can only be physically realized if ω-collapse occurs without any changes in chemical order. When the ω' chemical order does change, it can do so without any phase transition *per se*, and without any nucleation event. For convenience, this more stable configuration is referred to as ω'' [Fig. 1(c)], but it must be emphasized that *ω' and ω'' are two configurations of the same phase*. The notation ω' is only a convenient name for the idealized configuration with B2 order that was inherited in a diffusionless transition.

The ω-collapse may be "complete" or "incomplete" (meaning that the double layers are planar, or rumpled, respectively). The inherited B2 order in ω' would create trigonal symmetry ($P\bar{3}m1$) even if the ω-collapse were complete because that is the symmetry of ω' chemical order; this is analogous to the fact that $L1_0$ CuAu is tetragonal even if $c/a = 1$. Provided the single layers remain planar and symmetrically distinct (different occupancies), then chemical order in the double layers implies that they must be rumpled. In Fig. 1(b) it can be seen that the single layers adjacent to each double layer indeed have different occupancies. A consideration of the interactions between single and double layers in terms of pairwise interaction parameters that are functions of interatomic separations suggests that the ordered

Table 1. Crystallographic information

Struckturbericht or phase name	Prototype	Space group	$(111)_{cubic}$ or $(0001)_{trig,hex}$ Layer sequence
A2	W	$Im\bar{3}m$	A - A A
B2	CsCl	$Pm\bar{3}m$	A B A
ω	ωTi	$P6/mmm$	A A A A
Trigonal-ω	$Nb_{1-x}Zr_x$	$P\bar{3}m1$	A A·A A
ω', ω''	—	$P\bar{3}m1$	A B A B A B A
$B8_2$	Ni_2In	$P6_3/mmc$	A A B A B A A

Note: (1) A, B and A/B above correspond to the occupants of Wyckoff [illegible] 2d, 2d in space group $P\bar{3}m1$. All these structures [illegible] $P\bar{3}m1$ is a subgroup of all of the others. (2) Both solid and dashed [illegible] to emphasize that they are not required [illegible]

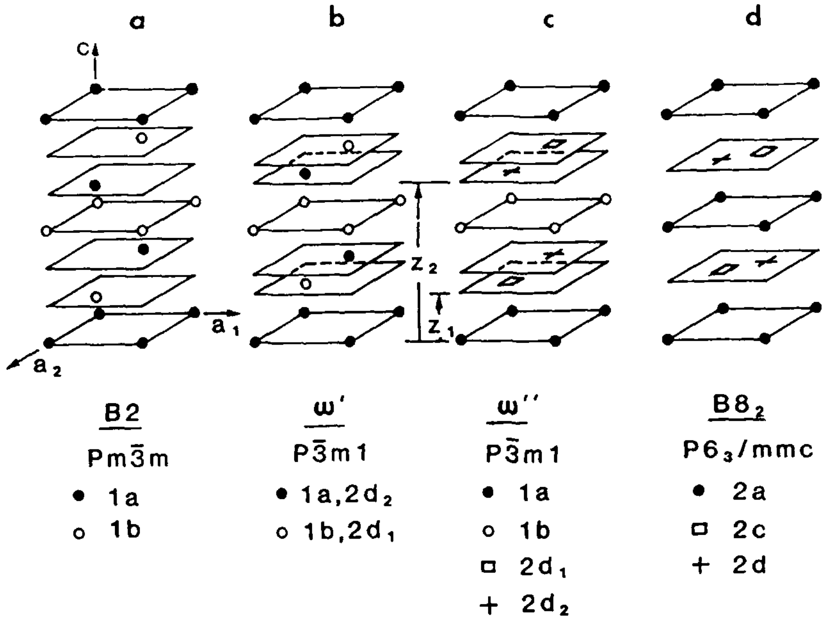

Fig. 1. Schematic drawing of (a) B2; (b) hypothetical ω'; (c) ω''; (d) $B8_2$ crystal structures. Different symbols represent different sites occupancies.

double layers could only be planar (fully collapsed) as an accidental degenerecy, e.g. at an isolated point in pressure, temperature, composition space. It is therefore inevitable that the double layers in ω' be rumpled and that the z coordinates of the 2d sites in P$\bar{3}$m1 have general (not special) values. Note however, that rumpling seems to occur also in the absence of chemical order (e.g. the trigonal ω Zr–Nb alloys [8]).

If the B2 occupancy is that reported by Banerjee *et al.* [9]; viz. Ti on one site and Al plus Nb on the other, then the P$\bar{3}$m1 sites of ω' would have the 1a and $2d_2$ sites occupied by Ti and the 1b and $2d_1$ sites occupied by a disordered mixture of Al and Nb (for $z_1 < z_2$). For the trigonal P$\bar{3}$m1 space group all reflections are allowed [10]; but as Strychor *et al.* [2] pointed out, when B2 ordering is perfectly preserved, the structure factor of the $1\bar{1}00$ reflection is numerically zero. In as-quenched and in heat treated samples, they observed reflections at $\frac{1}{3}\,11\bar{2}_{b.c.c.}$ positions of selected area electron diffraction patterns (SADP) which correspond to the $1\bar{1}00$ reflection of the ω-phase. They concluded that the ordered ω-phase had the $B8_2$ structure [Fig. 1(d)]. The $B8_2$ structure is a hexagonal ($P6_3/mmc$ space group) ω-derivative with basal layer sequence . . . A—A/B—A—B/A—A . . . for A_2B stoichiometry, or . . . C—A/B—C—B/A—C . . . for ABC stoichiometry. In the $B8_2$ structure the double layers are not rumpled, and if they were, such rumpling would destroy the mirror plane in (0, 0, 0, 1/4). Experimentally, one can distinguish P$\bar{3}$m1 from $P6_3/mmc$ by the presence or absence of odd $000l$ reflections respectively.

The $B8_2$ structure has been observed in several metallurgical systems in which a high temperature phase has a b.c.c. structure. Banerjee and Cahn [11, 12] have observed the formation of the $B8_2$ phase during aging of disordered ω in Zr–Al and discussed the occurrence of displacive and chemical (replacive) ordering. A $B8_2$ phase based on Ni_2Al has also been observed by Reynaud [13–14] and Lasalmonie [15].

The present investigation was conducted using an alloy of composition Ti_4Al_3Nb which was part of a more general survey of Ti-Al-Nb alloys [16]. It exhibits many microstructural features similar to the ω-type structures found by Strychor *et al.* [2] for a Ti-27.8 at.% Al-11.7 at.% Nb alloy. The composition studied lies on the TiAl-TiNb pseudobinary section midway between the compositions TiAl and Ti_2AlNb. An alloy along this section was chosen for the following reasons. The B2 occupancy reported by Banerjee *et al.* [9] showed that Ti tends to occupy one site while Al and Nb tend to occupy the other site; whereas, the $D0_{19}$ occupancy reported by Konitzer *et al.* [17] have shown that, Ti and Nb tend to occupy one site and Al the other. Thus one might argue that alloys along the Ti_3Al–Nb_3Al section would favor the formation of the hexagonal and the related orthorhombic phases. Alloys along the section TiAl–TiNb would provide maximum B2 order and increase the probability that B2 derivatives will form. This of course assumes that enough Nb is present to avoid the $L1_0$ γ-TiAl phase in the ternary but not so much that the metastable miscibility gap of the b.c.c. phase based in the Ti–Nb binary system [18] is a factor.

2. EXPERIMENTAL

An alloy with the Ti_4Al_3Nb composition was prepared by arc melting. Approximately ten remelts were necessary to ensure complete melting of the components. The cast button solidified as a b.c.c. phase and exhibited only slight dendritic microsegregation (~2 at.%) with no second phase. Pieces from the button were homogenized at 1400°C for 3 h under 2/3 atm gettered Ar gas. Precision of temperatures in that furnace is estimated to be about 20°C. Samples were placed on a Y_2O_3-coated Al_2O_3 substrate supported by a moveable pedestal. Cooling to room temperature was performed by lowering the pedestal out of the hot zone of the furnace into a lower cold chamber. The initial cooling rate was estimated to be about 400°C/min. One of these pieces was examined in the as-cooled condition and is designated HT1. Two sets of specimens (HT2 and HT3) were treated at 1100°C. The HT2 specimen was prepared using a 4 day hold at 1100°C during cooling from 1400°C followed by cooling to room temperature at ~400°C/min. The HT3 specimen was prepared by encapsulating Ta foil-wrapped slices in evacuated and He-backfilled quartz tubes and heat treating at 1100°C for 4 days followed by a water quench. These water quenched samples were not homogenized at 1400°C. A fourth set of samples (HT4) was obtained by a heat treatment of homogenized samples in similar tubes at 700°C for 26 days followed by a water quench. Sample HT1 was analyzed for O, N and H with 630, 50 and 7 ppm by weight respectively as determined by inert gas fusion (O, N) and vacuum hot extraction (H). The thermal histories of the specimens are summarized in Table 2.

All four specimens (HT1–HT4) were studied by transmission electron microscopy (TEM). TEM thin foils were prepared by standard twin-jet electropolishing using a 300 ml methanol, 175 ml *n*-butanol, 30 ml $HClO_4$ electrolyte at 0°C.

Optical and SEM/microprobe metallography of all four specimens was also performed because the scale of some of the microstructural details formed at high temperatures was quite coarse. Compositional analysis was performed on unetched samples using elemental standards.

The HT1 and HT4 specimens were also studied using single crystal X-ray diffractometry [19]. For that purpose small (< 0.5 mm) cubes were cut with a slow speed diamond saw from single grains observed by optical microscopy.

High load (120 kg) diamond pyramid indentation testing was performed. All samples described in this paper shattered whereas other compositions in the Ti–Al–Nb system (e.g. Ti_2AlNb and Ti_5Al_2Nb) do not crack.

Table 2. Thermal history of the investigated specimens

Specimen	Stage 1	Stage 2
HT1	1400°C, 4 h, SC	—
HT2	1400°C, 4 h, SC	1100°C, 4 days, SC
HT3		1100°C, 4 days, WQ
HT4	1400°C, 4 h, SC	700°C, 26 days, WQ

SC cooling rate of ~400 K min

WQ water quenched

3. RESULTS

3.1. *Microstructures of samples annealed at 1400 and 1100°C*

All specimens cooled or quenched from 1400 and 1100°C (HT1, HT2 and HT3) contain two different microstructural scales: one on the order of 10^3 to 10^1 μm observed by optical metallography, and another on the order of 10^{-1} μm or less, only observed by TEM. In these samples the coarse scale represents the microstructure present at high temperature while the fine scale represents a phase transformation of the matrix during cooling. First we describe the coarse structure and indicate the equilibrium phases present at temperature and second we identify the crystal structure of the matrix as transformed after cooling.

3.1.1. Phases present at temperature. On the scale of optical and SEM microscopy, the 1400°C sample (HT1) consists of large single phase grains. The composition of these grains as determined with SEM microprobe was Ti–36.2 at.% Al–12.5 at.% Nb in good agreement with the nominal alloy composition. The 1100°C samples (HT2 and HT3) consisted of

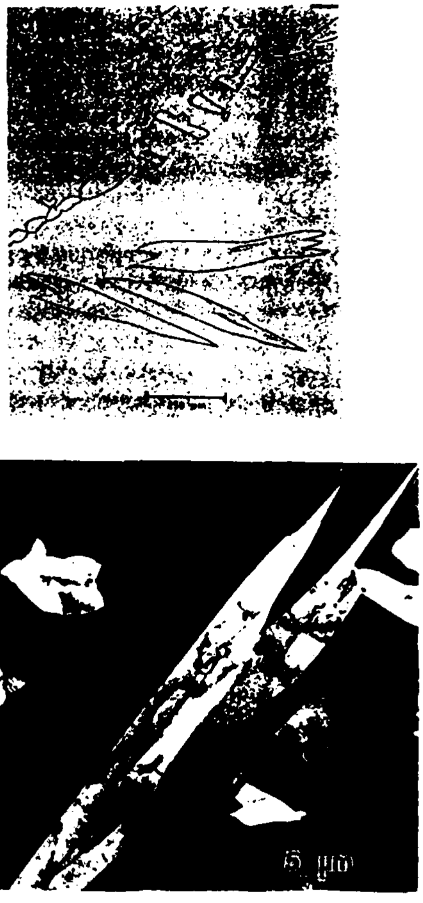

Fig. 2. Optical (a) and TEM (b) images of precipitates formed at 1100°C (HT3 specimen). The TEM image shows a complex morphology of the precipitates which was identified as a duplex structure of two Al–Ti phases ($D0_{19}$ and $L1_0$)

large grains of the same phase (as will be evident later) with an included second consituent comprising about 6% of the sample volume as shown in Fig. 2(a). The second constituent occurred in a facetted morphology with reentrant angles suggesting that the constituent might not be a single orientation. Examination of this second constituent with TEM [Fig 2(b)] and SAD (Fig. 3) indicated that they were duplex particles of $D0_{19}$ and $L1_0$ phases based on binary Ti–Al phases. The two phases structure was not identified until the TEM work was done leading to a false conclusion in a previous preliminary report [16]. The two phases coexist with the commonly observed orientation relationship (11$\bar{1}$) and [110] of the $L1_0$ parallel to the (0001) and [11$\bar{2}$0] of the $D0_{19}$ (Fig. 3). They both have an orientation relationship with the transformed B2 matrix, as shown in Fig. 3. Both phases were quite large (> 10 μm) suggesting they were present at the heat treatment temperature of 1100°C.

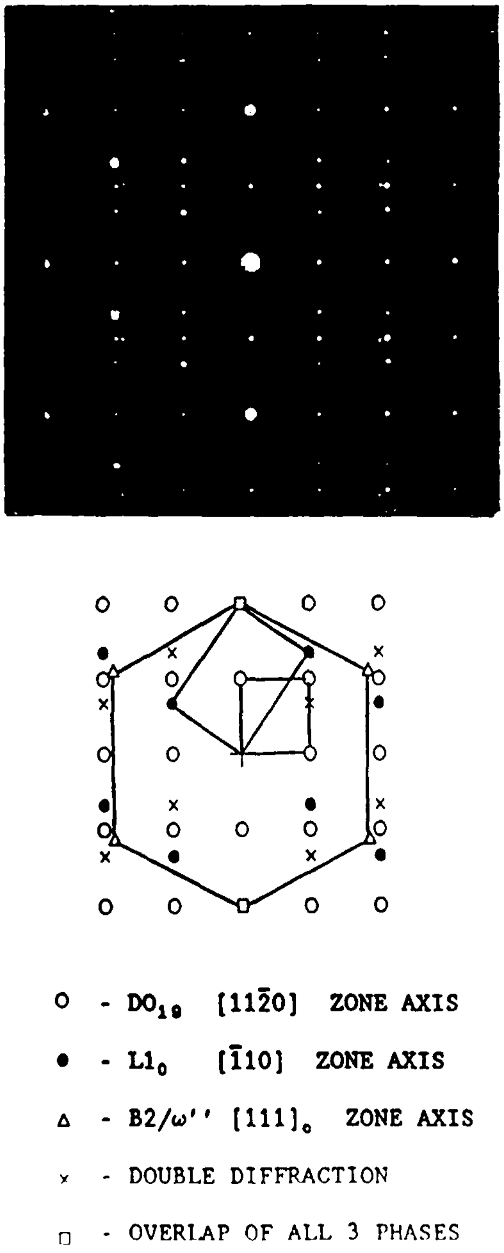
O - DO_{19} [11$\bar{2}$0] ZONE AXIS
● - $L1_0$ [$\bar{1}$10] ZONE AXIS
△ - B2/ω'' [111]$_0$ ZONE AXIS
x - DOUBLE DIFFRACTION
□ - OVERLAP OF ALL 3 PHASES

Fig. 3. SADP from one of the HT3 specimen, precipitates (Fig. 2a) showing the following orientation relationship between the DO_{19} (h) and $L1_0$ (t) phases: [11$\bar{2}$0]$_h$, [$\bar{1}$10]$_t$ and (0001)$_h$, (11$\bar{1}$)$_t$

The identity of the matrix phase present at 1400 and 1100°C for this alloy composition can only be inferred. The fine scale microstructure observed by TEM strongly suggests the decomposition of a B2 phase during cooling from temperature as described in detail below. No B2 APB's have been observed indicating stability of the B2 order as high as 1400°C. As recent investigations have shown [16], the B2 phase exists as an equilibrium high temperature phase over a large compositional field of the Ti–Al–Nb system. For several other alloy compositions, the B2 phase was found directly in cooled specimens. TEM observation shows that the microstructures of the HT1 and the matrix of the HT2 specimens are similar. This indicates that the decomposition of the B2 phase occurs at some temperature below 1100°C during continuous cooling.

STEM/EDX composition analysis was performed to estimate the compositions of the matrix, $D0_{19}$, and $L1_0$ phases in HT2. Sample HT1, which is uniform in composition, was used to determine the experimental Cliff–Lorimer coefficients. The results are given in Table 3 which also summarizes the equilibrium phases present in this alloy at temperature (results for 700°C to be described below are also included).

3.1.2. Formation of the ω-type phase during cooling. The microstructure and crystallography of the transformed matrix phase which forms during cooling from temperatures of 1100°C and above involves ω-type phases. Selected area diffraction (SAD) with a large aperture from HT1 shows patterns with strong reflections corresponding to the B2 lattice and additional weaker superlattice reflections, e.g. $[110]_c$ and $[111]_c$ cubic zone axes are shown in Fig. 4(a–b). According to Strychor *et al.* [2], who showed similar diffraction for a Ti–27.8 at.% Al–11.7 at.% Nb alloy, the superlattice reflections can be described as belonging to the ordered omega-type phase with the following lattice parameters for its hexagonal Bravais lattice: $a = 0.46$ nm and $c = 0.58$ nm (the c-parameter is twice that of disordered omega-phase). We will

Table 3. Equilibrium phases in Ti–37.5 at.% Al–12.5 at.% Nb at various temperatures

Temperature (°C)	Phases	Composition Ti at.%	 Al at.%	 Nb at.%
1400	B2*	50	37.5	12.5
1100	B2*	53	34	13
	$L1_0$	45	45	10
	$D0_{19}$	54	34	11
700	$B8_2$	52.5	34.5	13
	$L1_0$	41	50	9
	$D0_{19}$ (trace)			

*Structure inferred from the ordered ω-type decomposition product.

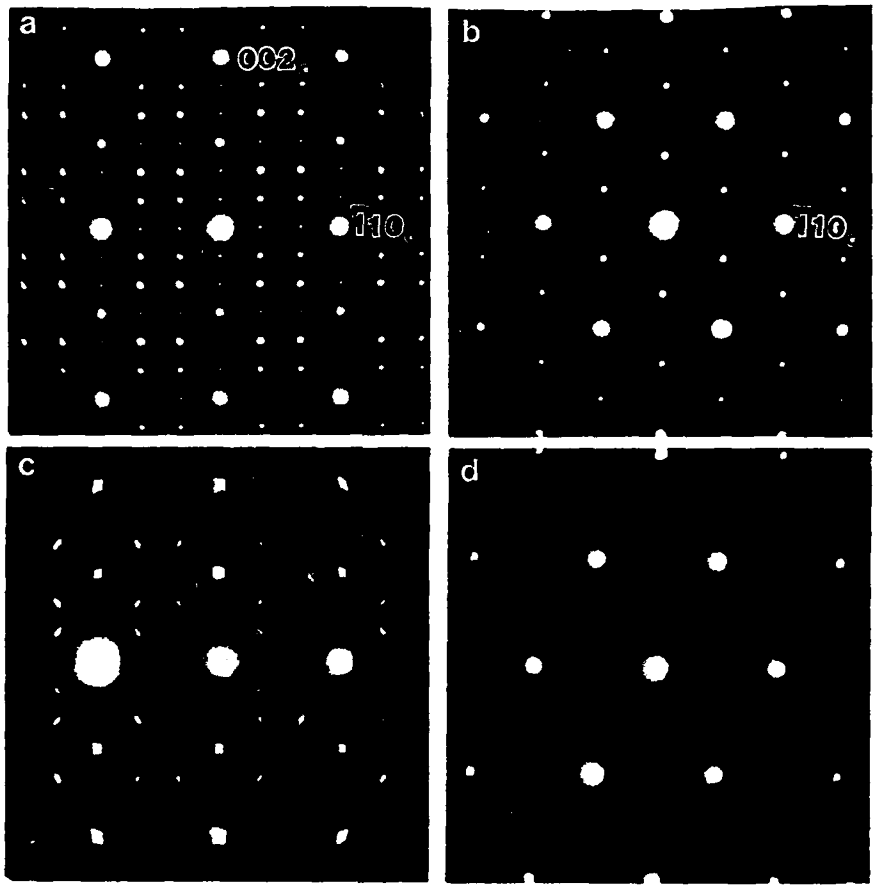

Fig. 4. SADP's from decomposed B2 phase of the HT1 specimen cooled from 1400°C at ~400°C/min (a, b) and of the HT3 specimen water-quenched from 1100°C (c, d). (a, c) $[110]_{bcc}$ zone axis; (b, d) $[111]_{bcc}$ zone axis.

show that this phase has the trigonal space group $P\bar{3}m1$ with the structure of ω'' shown in Fig. 1(c) and not the $B8_2$ structure shown in Fig. 1(d).

The omega-type phase observed here occurs in the usual orientation relationship with the parent cubic phase: $(111)_c \| (0001)_h$ and $[1\bar{1}0]_c \| [11\bar{2}0]_h$, which produces four rotational variants. The SAD patterns are superpositions of these four variants of the omega-type phase. The pattern $[110]_c$, [Fig. 4(a)], consists of two $\langle 11\bar{2}0 \rangle_h$ and two $\langle 1\bar{1}02 \rangle_h$ zone axes, and the pattern $[111]_c$, [Fig. 4(b)], consists of one $[0001]_h$ and three $\langle 2\bar{2}01 \rangle_h$ zone axes. The $\langle 1\bar{1}02 \rangle_h$ and $\langle 2\bar{2}01 \rangle_h$ patterns of the omega-type phase are practically indistinguishable from the $[110]_c$ and $[111]_c$ patterns of the B2 phase as seen in zero order Laue zones [but they can be distinguished by a difference in the radii of higher order Laue zones (HOLZ)]. Some reflections in the patterns are the result of dynamic double diffraction, e.g. in the $[110]_c$ pattern, the $\frac{1}{3}\bar{h}h0_c$ and $\frac{1}{3}001_c$ reflections are caused by double diffraction (verified by their disappearance after tilting along this row of reflections).

TEM observation shows that the microstructures of the HT1 and the matrix of the HT2 specimens are similar in spite of different heat treatments and slight differences in composition due to the formation of the $D0_{19}$ and $L1_0$ phases in HT2. Their microstructures consist of small (<0.2 μm) domains producing complex contrast in a bright-field image, Fig. 5(a), due to some overlapping through the TEM foil thickness. The domains can be clearly seen using dark-field imaging with a reflection belonging only to one rotational variant of the omega-type phase, e.g. with the $1\bar{1}00$ reflection. Such a dark-field image is shown in Fig. 5(b). Some of the imaged regions contain internal boundaries. The presence of triple junctions of the boundaries implies the existence of at least three translational domain subvariants for each rotational domain variant [as imaged in dark field in Fig. 5(b)].

It is important to find out if the odd $000l$ reflections are absent in order to distinguish between the structure of the various ω-type and $B8_2$ phases. For that purpose tilting along a row of $000l$ (or 111_c) reflections was performed in order to eliminate roots for double diffraction. As can be seen in Fig. 6(a) where only the one row is excited, no extinction of odd reflections is observed. However the result can be due to the double diffraction between two variants, viz 0002 (= 111_c) of one variant and $02\bar{2}1$ (= 111_c)

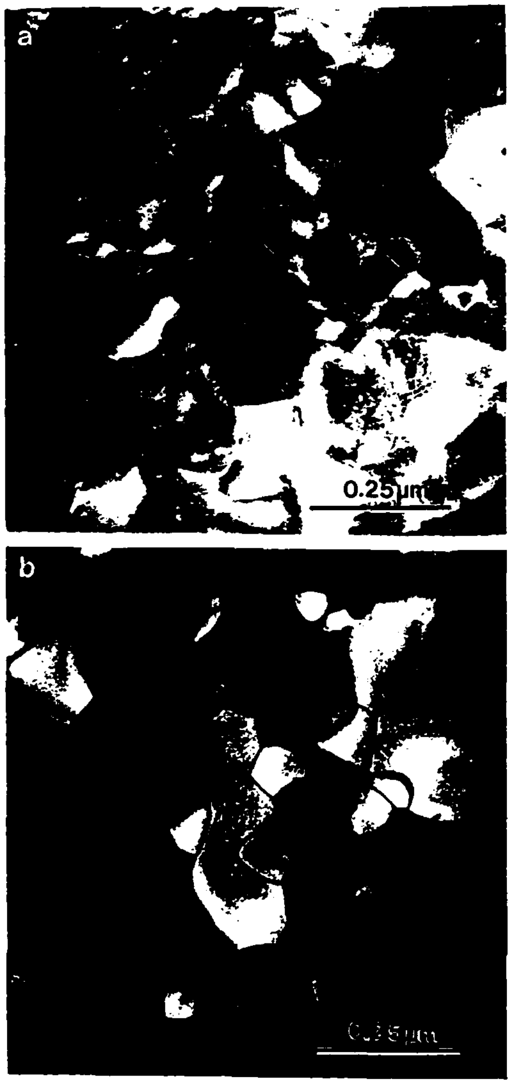

Fig. 5. Microstructure of the HT1 specimen cooled from 1400°C. TEM complimentary bright-field (a) and dark-field (b) images. Dark-field shows only one (out of four) rotational variant of the ω-type phase. Observed interfaces within the domains separate translational domains.

of the other variant from the same row. To eliminate this possible effect, microdiffraction from a small thin area was used in order to ensure diffraction from only a single domain. The result is shown in Fig. 6(b), where odd 000l reflections are clearly seen for one variant.

Microdiffraction from a neighboring domain shows $0\bar{2}21(=0003)$ reflection for another variant Fig. 6(c)]. The observation of odd 000l reflections suggests that the phase has *trigonal rather than hexagonal symmetry*.

From dark-field imaging of different single rotational variants [similar to that shown in Fig. 5(b)], it is evident that the omega-type phase is the major phase occupying most of matrix. This is in contrast to many other alloys (including the composition studied by [2]) where ω phase usually exists only as small particles in a matrix. However from the TEM observation only, it is difficult to decide if there is a retained B2 or b.c.c. phase as well. A cubic phase can not be imaged separately because of perfect overlapping of its reflections with those of the omega-type phase. Morphologically there is no evidence for the presence of a retained B2 phase (one would expect to see a continuous layer separating the ω-type phase domains). It is in principle possible to detect the cubic phase using convergent beam diffraction and analysis of HOLZ reflections. This however would not give an overall morphological picture and the phase identification would be complicated by possible overlapping of domains. It should be noted, however, that results from single crystal X-ray diffraction suggest that a certain amount of the cubic phase was retained in sample HT1.

Sample HT3 was prepared to determine if the higher cooling rate of water quenching could prevent transformation of the high temperature cubic phase to the ω-type phase. This was unsuccessful as is evident from the SAD patterns taken from the HT3 specimen as shown in Fig. 4(c, d). The patterns can be compared with those in Fig. 4 (a, b) from the HT1 specimen because they are in the same cubic orientation. The HT3 quenched specimen has the same sort of omega-type reflections, however they are diffuse maxima rather than sharp spots. For the $[110]_c$ zone axis no double diffraction spots like $\frac{1}{3}\,\bar{1}10_c$ or $\frac{1}{3}\,001_c$ are present. There is strong diffuse intensity in the form of spot streaking and arcs, typical of the early stages of ω-phase formation. In addition, diffuse

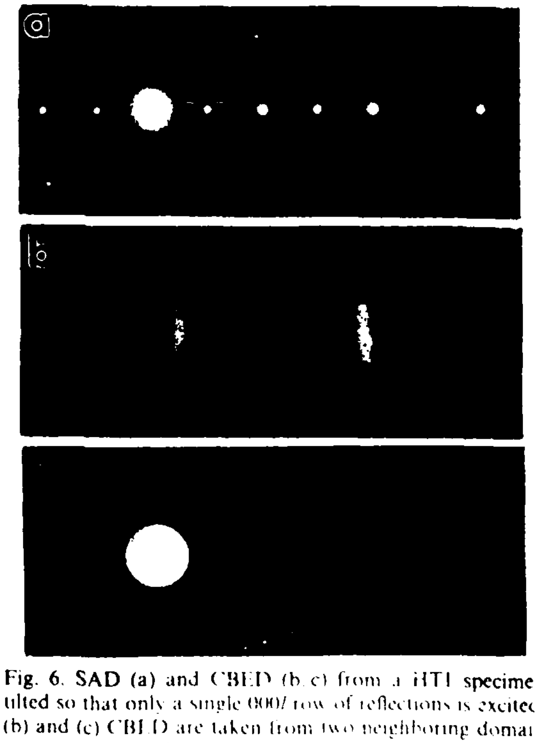

Fig. 6. SAD (a) and CBED (b, c) from a HT1 specimen tilted so that only a single 000l row of reflections is excited (b) and (c) CBED are taken from two neighboring domain (different rotational variants)

maxima in $\frac{1}{2}\bar{1}10_c$-type positions are also observed [Fig. 4(c)] which is evidence for retained B2 matrix usually showing displacive $[1\bar{1}0](110)$ instability [16]. Comparison of the $[111]_c$ zone axis patterns shows that the $1\bar{1}00$ reflections are much weaker in the HT3 specimen than in the HT1 (or HT2) specimens. Dark-field images using a strong reflection (belonging simultaneously to several variants and possibly to the cubic phase) in a two beam condition have contrast consisting of striations [Fig. 7(a)]. A dark-field image using a $1\bar{1}00$ reflection belonging only to one variant of the ω-type phase shows uniform distribution of very small diffuse particles (~2–3 nm), Fig. 7(b). It is not clear whether the weak $1\bar{1}00$ reflections in the HT3 specimen are due to their structure factor or to the volume fraction of the ω-type phase in the B2 matrix.

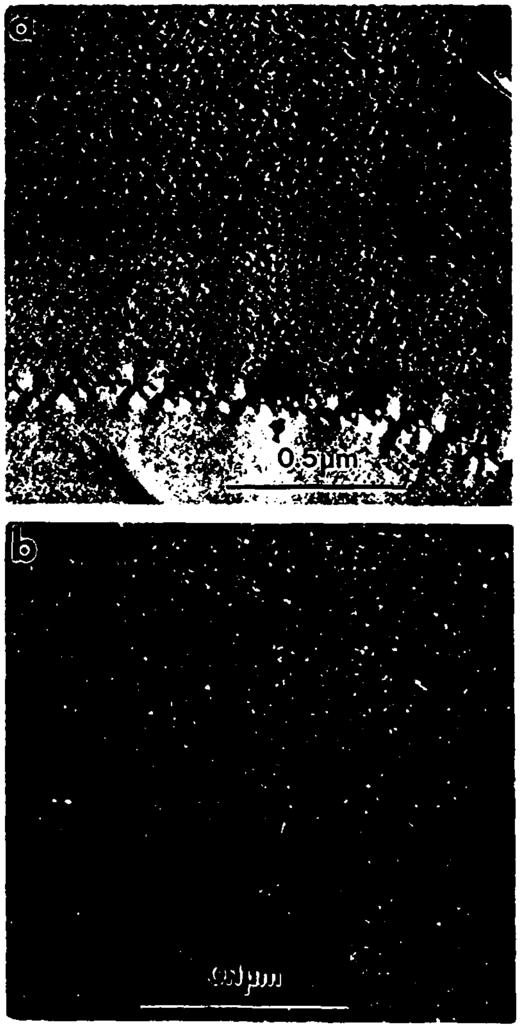

Fig. 7. Microstructure of the HT3 alloy matrix. A dark-field image using a cubic phase reflection shows striation contrast (a). A dark-field image using a $1\bar{1}00$ reflection of the ω-type phase shows very small discrete particles (b).

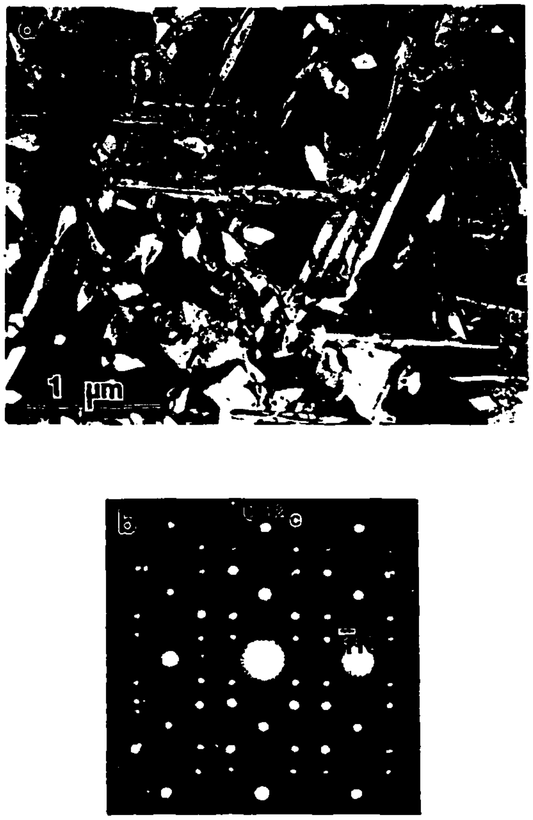

Fig. 8. (a) TEM micrograph of the alloy annealed at 700°C showing multi-domain structure and needles. (b) SADP of matrix phase.

3.2. Microstructure of samples annealed at 700°C

The microstructure of sample HT4 as observed by optical microscopy revealed large grains with a size established by the 1400°C treatment and a very fine needle precipitate structure formed at 700°C. TEM observation of the matrix phase shows that the microstructure has features similar to the matrices of the HT1 and HT2 specimens, i.e. predominantly a multidomain structure of a phase with ω-type reflections, Fig. 8(a, b). The ω-type phase has lattice parameters and orientation relationships practically identical to those in the HT1 and HT2 specimens [compare Fig. 8(b) with Fig. 4(a)]. However, the domains have a size that is almost an order of magnitude coarser than in the HT1 and HT2 specimens (~0.6 μm in size). As will be shown below, the size of these domains results from a phase transformation process from the trigonal ω'' phase produced during cooling from 1400°C to a $B8_2$ phase during heat treatment at 700°C.

The domains are large enough to perform accurate convergent beam electron diffraction (CBED) symmetry analysis from an area thick enough to have dynamical diffraction effects. Figure 9 shows large and small magnification CBED patterns for the [0001] and $[11\bar{2}0]$ zone axis orientations. As is clearly seen from the patterns, the whole pattern symmetry is 6 mm for the [0001] orientation and 2 mm for the $[11\bar{2}0]$ orientation. The symmetries are inconsistent with the symmetry of the trigonal ω-type phase

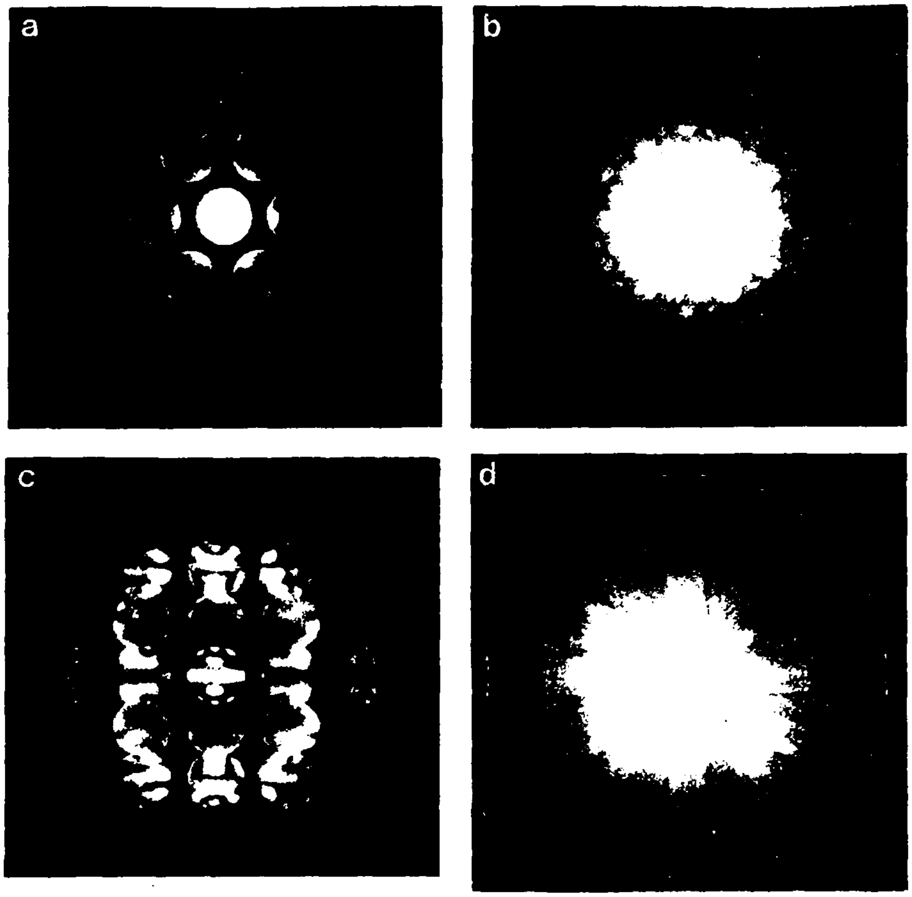

Fig. 9. High (a, c) and low (b, d) magnification CBED patterns in [0001] and [11$\bar{2}$0] orientations from a single domain of the matrix phase in an alloy annealed at 700°C. the patterns are consistent with point group symmetry 6/mmm.

determined for the HT1 and HT2 samples. (For the trigonal space group P$\bar{3}$m1, the CBED whole pattern symmetry must be 3m and 2, respectively.) The observed whole pattern symmetries establish unambiguously that the phase has hexagonal point group symmetry 6/mmm [20].

Additional confirmation that the matrix phase in the 700°C sample has hexagonal symmetry is the absence of odd 000*l* reflections (Fig. 10) under diffraction conditions similar to those shown in Fig. 6(b), suggesting that they are kinematically forbidden. This is in accord with the observation of dynamic absences in the form of a black cross [Fig. 9(c)] for a kinematically forbidden 0001 reflection in the [11$\bar{2}$0] zone axis. These dynamical absences are the result of the simultaneous presence of a screw axis and a glide plane in the structure, which can only be explained by the space group $P6_3/mmc$ [20, 21]. The $P6_3/mmc$ space group is that of the $B8_2$ structure suggested by Strychor and co-authors for the Ti–Al–Nb omega-type phase [2] [Fig. 1(d)], and is confirmed here.

Since the microstructure of the HT4 specimen prior to the 700°C treatment consisted of the ω″ phase, the main effect of the 700°C annealing seems to be an ω″→$B8_2$ transformation. In addition to the transformation of the omega-type phase from trigonal to hexagonal symmetry, fine precipitates also formed during the annealing. These were identified as needles found in a common orientation within the hexagonal $B8_2$ matrix, Fig. 11(a). The phase was identified by microdiffraction, Fig. 11(b), as the $L1_0$ phase, and its composition as well as that for the nearby $B8_2$ matrix were estimated by EDS and are given in Table 3. Occasionally trace amounts of the $D0_{19}$ phase were seen in a peculiar band morphology in combination

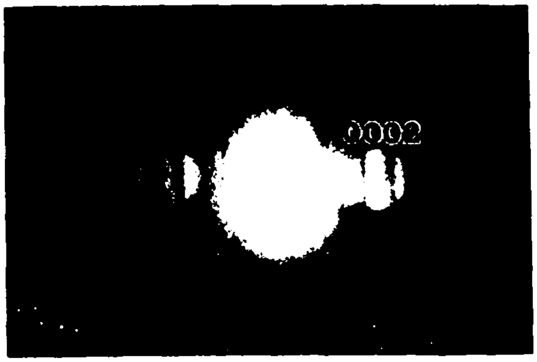

Fig. 10. Single row excitation showing absence of odd 000*l* reflections.

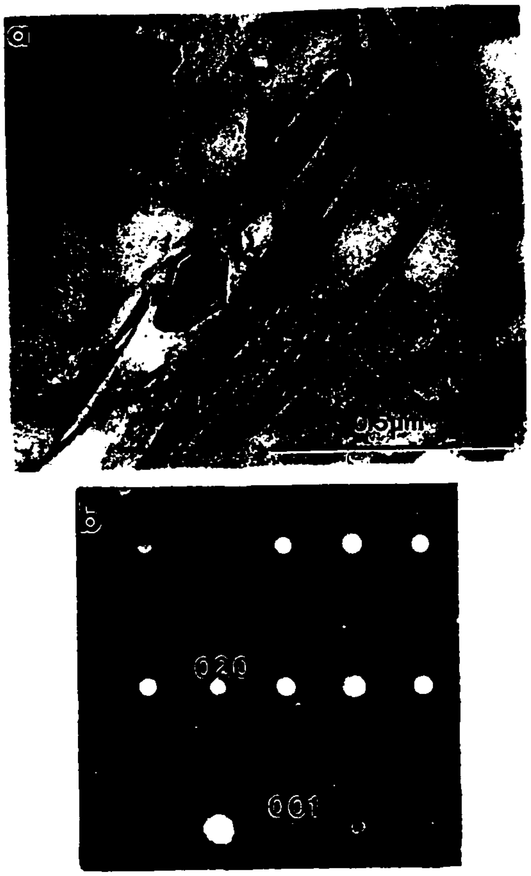

Fig. 11. (a) Needles observed in alloy annealed at 700°C and (b) identified as the $L1_0$ phase.

with the $L1_0$ phase. As summarized in Table 3, the equilibrium phases at 700°C are primarily $B8_2$ and $L1_0$, with a trace amount of $D0_{19}$.

Early stages of the transformation from the ω" phase to the two major phases were occasionally observed in some regions of the HT2 specimens (probably those regions were subjected to slower cooling than the regions whose microstructures were described under the 1100°C treatment). Figure 12(a) shows a dark-field image of one of these HT2 specimens in a condition where only one rotational variant of the ω-type phase is imaged, and where some noticeably larger domains are seen. Careful CBED analysis shows that the large domains have the hexagonal symmetry of the $B8_2$ phase while the smaller domains have the trigonal symmetry of the ω"-phase. The larger domains have a structure of translation domain boundaries different from that which is typically observed in the trigonal phase, Fig. 5, i.e. triple junctions are observed in the ω"-phase but there are absent from the large $B8_2$ domains. The transformed phase usually forms along heterogeneities, as shown in Fig. 12(b). The heterogeneity was identified by SAD and microdiffraction as the $L1_0$ phase, in the case of Fig. 12(c)

3.3. Single crystal X-ray diffraction study of ω" and $B8_2$ phases

Single crystal X-ray diffraction experiments were performed on HT1 and HT4 samples using Mo K_α radiation in order to verify and refine the structures of the ω" and $B8_2$ phases suggested by the TEM observations. The structure refinements were performed using the intensities of the non-superimposed

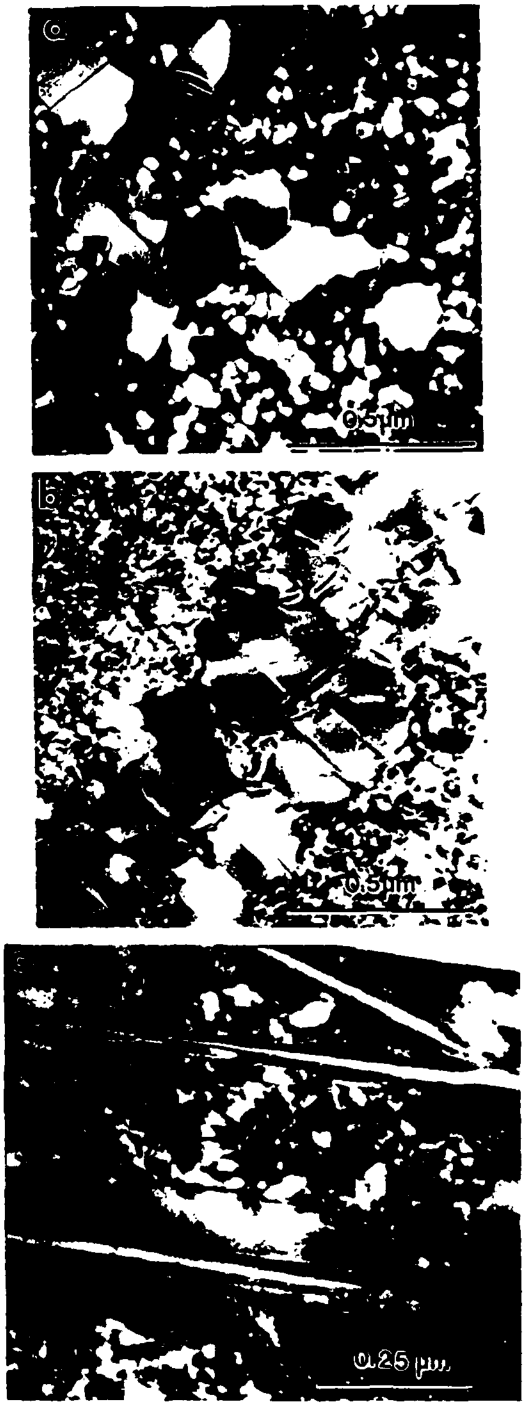

Fig. 12 (a) Large $B8_2$ domains adjacent to fine ω" domains. (b) Formation of $B8_2$ domains along an unidentified heterogeneity and (c) along a plate of the $L1_0$ phase reflections from one of four variants in the full-matrix least-squares program contained in the TEXRAY system [19]. The final R value was 0.032 for the ω'' phase and 0.076 for the $B8_2$ phase. The interpretation of the refined values of the scattering factors was based on the assumptions: (a) a composition of Ti_4Al_3Nb for the ω'' phase and the $B8_2$ phase; (b) no more than two species on each site for ω''. The results are summarized in Tables 4 and 5.

With the exception of whether residual B2 or b.c.c. exists, the TEM and X-ray results are consistent. This shows that the matrix phase of alloys cooled from 1400 or 1100°C, designated ω'', is a partially collapsed trigonal ω phase with an atomic arrangement different from but related to, the precursor B2 phase. The $B8_2$ phase annealed at 700°C involves reordering and completion of the collapse.

4. DISCUSSION

Except for the small amounts of $L1_0$ and $D0_{19}$ phases that were formed, the sample retained an approximately constant composition throughout the transformation sequence: $B2 \rightarrow \omega'' \rightarrow B8_2$. Chemical ordering of b.c.c. to B2 presumably occurred on cooling at some temperature above 1400°C, but this transition was not documented in the present study. The almost complete transformation of the B2 phase to an ω-type phase permits the observation of domain boundaries associated with the four rotational crystal variants and the three translational subvariants. In Fig. 5(b) three subvariants are observed within a single rotational variant. The availability of large grains containing the ω'' and $B8_2$ variants also permitted detailed single crystal analysis of the collapse parameters and site occupancies.

4.1. *Structural relations*

All observed (or inferred) crystal structures of this transformation sequence can be described in terms of the $P\bar{3}m1$ space group. The correspondence between hexagonal and cubic unit cell parameters is: $a_1 = [1\bar{1}0]_c$; $a_2 = [01\bar{1}]_c$; $c = [111]_c$. Four Wyckoff positions are sufficient to describe the structures: 1a (0, 0, 0); 1b (0, 0, 1/2); $2d_1$ $(1/3, 2/3, z_1)$ and $(2/3, 1/3, 1\text{-}z_1)$; $2d_2$ $(1/3, 2/3, z_2)$ and $(2/3, 1/3, 1\text{-}z_2)$. In Table 6 we summarize the site occupancies (related to chemical order parameters) and z-parameters (related to displacive order parameters) that characterize the different structures. All occupancies are based on the composition Ti_4Al_3Nb. Only ω'' and $B8_2$ values were confirmed. It is apparent that the transformation sequence may be viewed as a continuous change of atomic occupancy and position.

Table 4. Structure of 1400°C sample (ω'')

1. $P\bar{3}m1$ space group, $a = 0.4555(1)$ nm, $c = 0.5542(1)$ nm

	x	y	z
1a 0.88Ti + 0.12 Nb	0	0	0
1b 0.68 Nb + 0.32 Al	0	0	1/2
$2d_1$ 0.97 Al + 0.03 Ti	1/3	2/3	0.2245(3)
$2d_2$ Ti	1/3	2/3	0.7175(2)

2. Residual B2 or b.c.c. phase derived from analysis of intensities of twin (superimposed) reflections

Table 5. Structure of 700 C sample matrix ($B8_2$)

1. $P6_3/mmc$ space group, $a = 0.4580(3)$ nm, $c = 0.5520(4)$ nm

	x	y	z
2a 0.5Ti + 0.125Al + 0.375Nb	0	0	0
2c Al	1/3	2/3	1/4
2d Ti	1/3	2/3	3/4

2. No residual B2 or b.c.c. phase from analysis of intensities of twin (superimposed) reflections

4.2. *Site occupancy in* ω''

The measured site occupancies of the ω'' phase indicate that the first change in chemical order is the transfer of Nb atoms out of double layers ($2d_1$, $2d_2$ sites) and into single layers (1a, 1b sites). The excess Nb "flows" to adjacent single layers in differing amounts due to different initial compositions of the single layers. The 1a sites, which were mostly Ti, pick up a smaller amount of Nb than do the 1b sites, which were originally a disordered mixture of Al and Nb. The absence of Nb from the double layers in the ω'' structure is consistent with near neighbor (nn) Lennard-Jones potentials for Al–Ti and Al–Nb nn pairs [22], and with the b.c.c. Ti–Nb interaction parameter in Moffat and Kattner [18]. These parameters indicate that: (1) the most stable "bond" type is Al–Ti (≈ -56 kJ/mol); 2) the Al–Nb bond is slightly less stable (≈ -51 kJ/mol); (3) the Ti–Nb bond is weakly unstable (≈ 5 kJ/mol); (4) the Al–Ti bond is more stable *at shorter distances* than the Al–Nb bond. The nn coordination polyhedra in the ω'' and $B8_2$ structures are different for atoms that are in double vs single layers. Those in double layers have more short bonds and therefore it is not surprising that Al–Ti ordering occurs on the double layers rather than Al–Nb ordering. In fact, the A–B distance in B2 is 0.277 nm whereas the Ti–Al distances in the double layers in the ω'' and $B8_2$ phases are 0.265 and

Table 6. Site occupancies and z parameters of phases using the $P\bar{3}m1$ space group

Site	**Element/ z-parameter**	**Phase** B2	ω'	ω''	$B8_2$
1a	**Ti**	**1**	**1**	**0.88**	**1/2**
	Al	**0**	**0**	**0**	**1/8**
	Nb	**0**	**0**	**0.12**	**3/8**
1b	**Ti**	**0**	**0**	**0**	**1/2**
	Al	**3/4**	**3/4**	**0.32**	**1/8**
	Nb	**1/4**	**1/4**	**0.68**	**3/8**
$2d_1$	Ti	0	0	0.03	0
	Al	3/4	3/4	0.97	1
	Nb	1/4	1/4	0	0
	z_1	1/6	$1/6 < z_1 < 1/4$	0.22	1/4
$2d_2$	Ti	1	1	1	1
	Al	0	0	0	0
	Nb	0	0	0	0
	z_2	4/6	$4/6 < z_2 < 3/4$	0.72	3/4

Note: B2 is $Pm\bar{3}m$ in which 1a = 1a, $2d_2$ and 1b = 1b, $2d_1$. $B8_2$ is $P6_3/mmc$ in which 2a = 1a, 1b and 2c = $2d_1$ and 2d = $2d_2$.

0.264 nm respectively. Therefore, the energetic basis for Nb "flowing" out of the double layers is the maximization of Al–Ti bonds which are the most stable. In the $B8_2$ structure the double layers are completely composed of Al and Ti with all of the Nb found on the single layers.

4.3. Symmetry relations

It useful to examine the subgroup/symmetry relations [10] that describe the transformation sequence $A2 \rightarrow B2 \rightarrow \omega'' \rightarrow B8_2$, i.e. $Im\bar{3}m \rightarrow [2]\ Pm\bar{3}m \rightarrow [4]\ R\bar{3}m \rightarrow [3]\ P\bar{3}m1 \rightarrow [2]\ P6_3/mmc$ (Fig. 13) because these relations can tell us; (1) which transitions are required to be first-order and which are allowed to be second-order (Landau theory [23]); (2) how many rotational or translational variants may be created/destroyed in the transition; (3) which intermediate phases are *likely* to be metastable. *The International Tables of Crystallography* [10] lists "maximal nonisomorphic subgroups" which are the space groups of possible product phases that form if the symmetry reduction does not include an intermediate step, e.g. $P\bar{3}m1$ is not listed as a maximal non isomorphic subgroup of $Pm\bar{3}m$ but $R\bar{3}m$ is, and $P\bar{3}m1$ is a maximal nonisomorphic subgroup of $R\bar{3}m$. The *index* of symmetry reduction (or increase) is an integer shown in brackets above that is equal to the number of symmetry elements in the supergroup divided by the number in the subgroup. If the index is an odd integer then the transition is required to be first-order in character (except at an isolated point), and if it is even then it may be either first- or second-order [23]. The index also corresponds to the number of domains variants that may be created in the product phase after a transition.

The $B2 \rightarrow \omega''$ transition involves two steps of symmetry *reduction*: (1) $Pm\bar{3}m \rightarrow R\bar{3}m$ corresponds to a homogeneous trigonal distortion that selects one of the four $\langle 111 \rangle$ directions in the B2 phase as the $\bar{3}$-axis in the trigonal ω- type phase; (2) $R\bar{3}m \rightarrow P\bar{3}m1$ selects which (111) planes collapse to form double layers and which remain as single layers. The real $B2 \rightarrow \omega''$ transition also involves chemical reordering. The index of four that is associated with homogeneous trigonal distortion gives the number of rotational variants, and the index of three that is associated with plane collapse gives the number of translational subvariants with each rotational variant. There is no

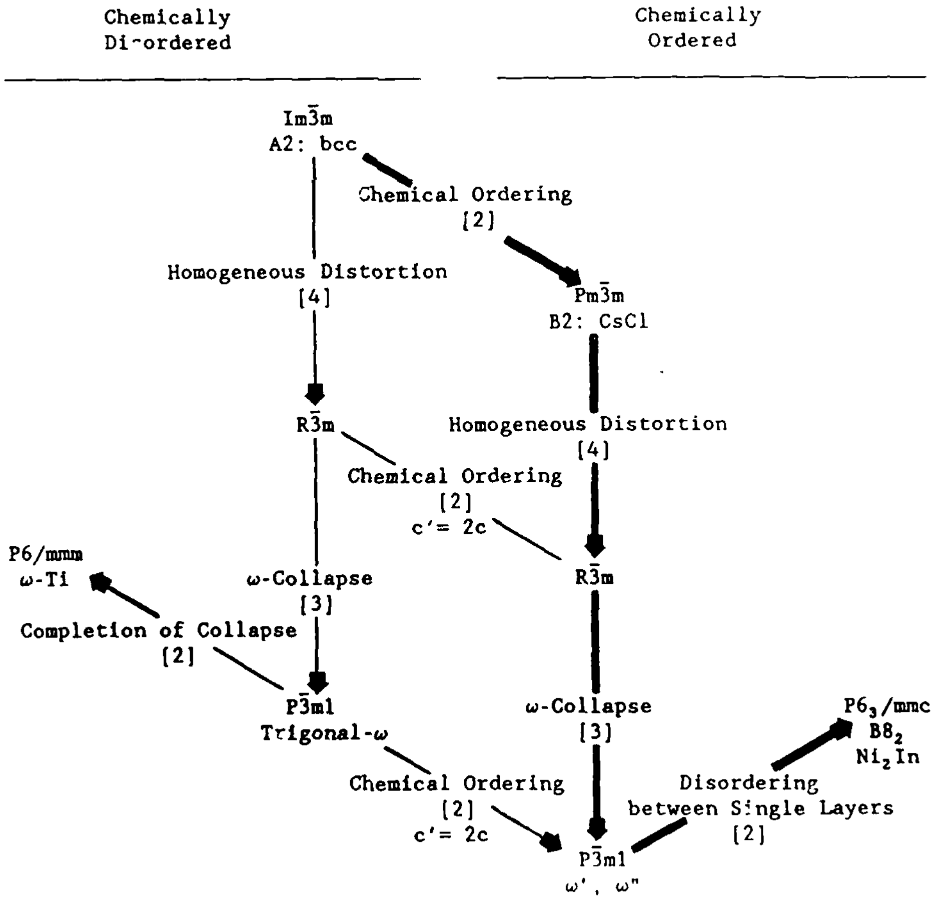

Fig. 13. Subgroup supergroup symmetry relations that describe the observed transformation path (shown as bold lines) $b.c.c. \rightarrow B2 \rightarrow \omega'' \rightarrow B8_2$, i.e. $Im\bar{3}m \rightarrow Pm\bar{3}m \rightarrow R\bar{3}m \rightarrow P\bar{3}m1 \rightarrow P6_3/mmc$, and other possible paths. Vertical lines indicate diffusionless transitions and angled lines indicate transitions that require diffusion (reordering) with the exception of the completion of the omega collapse for disordered ω.

evidence for a distinct R$\bar{3}$m phase associated with the homogeneous distortion, and there is no need for such a phase to be physically realized in the Pm$\bar{3}$m$\rightarrow$P$\bar{3}$m1 transition.

The $\omega''\rightarrow B8_2$ transition involves a symmetry increase. $P6_3$/mmc is a supergroup of P$\bar{3}$m1. An increase in symmetry is typically, but not always, associated with an increase in entropy so the low symmetry phase is expected to be the low temperature phase as well. Therefore, isothermal supergroup formation in the $\omega''\rightarrow B8_2$ transition suggests that ω'' is metastable. A much stronger indication of its metastability is that the $\omega''\rightarrow B8_2$ transition proceeds from a more ordered ω'' phase to a less ordered $B8_2$ phase. That is, the 1a and 1b site occupancies which are different in ω'' become indentical in $B8_2$, and this implies an increase in configurational entropy.

Evidently because ω'' is metastable, the equilibrium transformation is B2(Pm$\bar{3}$m)$\rightarrow B8_2$($P6_3$/mmc) which must be strongly first-order because $P6_3$/mmc is not a subgroup of Pm$\bar{3}$m. The observed path, B2$\rightarrow\omega''\rightarrow B8_2$, traverses a state of minimum symmetry (ω'', P$\bar{3}$m1) that is a subgroup of both Pm$\bar{3}$m and $P6_3$/mmc. This space group of minimum symmetry is in fact the intersection of the parent and product space groups. The formation of ω'' as an intermediate metastable phase provides a continuous structural path for the alloy to accomplish the B2 to $B8_2$ transition. Whether the $\omega''\rightarrow B8_2$ transformation is in fact continuous in the present case is not clear. As seen in Fig. 12 the $B8_2$ phase appears to form adjacent to $L1_0$ needles in the ω'' matrix and the domains of the $B8_2$ phase are much larger than those of the parent ω''. Both observations tend to suggest that the $B8_2$ has nucleated in the ω''. On the other hand it is possible that the $L1_0$ needles precipitate from the ω'' matrix creating a slight shift in ω'' composition locally that kinetically favors the continuous transformation to the $B8_2$. In this case the increased domain size of the $B8_2$ may be the result of domain coarsening. Nonetheless the observed formation of the intermediate metastable phase ω'' suggests that the concepts of subgroup/supergroup paths are important in the present case and the existence of the path provides the basis for a common thermodynamic function for all the phases involved [24].

4.4. Frustration

As mentioned above the strong near neighbor ordering tendencies in this system promote the formation of Al–Ti and Al–Nb nn pairs. The B2 structure permits an "unfrustrated" configuration of nn pairs such that *all* Al's may be surrounded by Ti's, and no Al–Al nn's need exist. The ω'' and $B8_2$ structures, however, only permit "frustrated" nn configurations in which the configuration with a maximum number of Al–Ti and Al–Nb bonds still has some unfavorable Al–Al nn's. Frustration reduces the critical temperatures of order–disorder transitions by introducing competing interactions. The partial disordering accompanying the $\omega''\rightarrow B8_2$ transition, where double layers remain ordered, but single layers become disordered (identical) is a manifestation of the frustration induced by the omega collapse.

Acknowledgement—The authors would like to thank A. J. Shapiro for the microprobe results, L. C. Smith for the metallography, and M. E. Williams for the TEM specimen preparation. Discussions with F. W. Gayle and J. W. Cahn are greatly appreciated as well as the support of DARPA under order No. 6065.

REFERENCES

1. T. J. Jewett, J. C. Lin, N. R. Bonda, L. E. Seitzman, K. C. Hsieh, Y. C. Chang and J. H. Perepezko, *Mater. Res. Soc. Symp. Proc.* **133,** 69 (1989).
2. R. Strychor, J. C. Williams and W. A. Soffa, *Metall Trans.* **19A,** 225 (1988).
3. D. Banerjee, A. K. Gogia, T. K. Nandi and V. A. Joshi, *Acta metall* **36,** 871 (1988).
4. M. J. Kaufman, T. F. Broderick, C. H. Ward, R. G. Rowe and F. H. Froes, *Proc. Sixth World Conf. on Titanium*, Cannes, France (1988).
5. M. J. Kaufman, AFWAL Technical Report-88-4113 (1988).
6. K. Muraleedharan and D. Banerjee, *Metall. Trans.* **20A,** 1139 (1989).
7. H. T. Kestner-Wykamp, C. H. Ward, T. F. Broderick and M. J. Kaufman, *Scripta metall* **23,** 1697 (1989).
8. S. K. Sikka, Y. K. Vohra and R. Chidambaram, *Prog. Mater. Sci.* **27,** 245 (1982).
9. D. Banerjee, T. K. Nandy and A. K. Gogia, *Scripta metall* **21,** 597 (1987).
10. *International Tables of Crystallography* (edited by T. Hahn), Vol. A. Reidel, Dordrecht (1978).
11. S. Banerjee and R. W. Cahn, *Acta metall.* **31,** 1721 (1983).
12. S. Banerjee and R. W. Cahn, in *Solid–Solid Phase Transformations* (edited by H. I. Aaronson, D. E. Laughlin, R. F. Sekerka and C. M. Wayman), p. 1005. TMS-AIME, Warrendale, Pa (1982).
13. P. F. Reynaud, *J. appl. Crystallogr.* **9,** 263 (1976).
14. P. F. Reynaud, *Scripta metall.* **11,** 765 (1977).
15. A. Lasalmonie, *Scripta metall* **11,** 527 (1977).
16. L. A. Bendersky and W. J. Boettinger, *Mater. Res. Soc. Proc.* **133,** 45 (1989).
17. D. G. Konitzer, I. P. Jones and H. L. Fraser, *Scripta metall.* **20,** 265 (1986).
18. D. L. Moffat and U. R. Kattner, *Metall. Trans.* **19A,** 2389 (1988).
19. C. B. Shoemaker, D. P. Shoemaker and L. A. Bendersky, *Acta crystallogr.* To be published.
20. B. F. Buxton, J. A. Eades, J. W. Steeds and G. M. Rackham, *Phil. Trans.* **281,** 171 (1976).
21. M. Tanaka, H. Sekii and T. Nagasawa, *Acta crystallogr.* **A39,** 825 (1983).
22. M. Enomoto and H. Harada, *Metall. Trans.* **20A,** 649 (1989).
23. L. Landau and E. M. Lifschitz, *Statistical Physics*. Pergamon Press, Oxford (1976).
24. B. P. Burton. To be published.

Submitted to
Acta Met, 6.8.90

COHERENT PRECIPITATES IN THE BCC/ORTHORHOMBIC TWO PHASE FIELD OF THE Ti-Al-Nb SYSTEM

L. A. Bendersky, W. J. Boettinger and A. Roytburd

Metallurgy Division

National Institute of Standards and Technology

Gaithersburg, MD 20899

ABSTRACT

Alloys of composition Ti_2AlNb and Ti_4AlNb_3, cooled from 1400°C and equilibrated at 700°C for 26 days, were both found to consist of two phases: the Ti- and Nb-rich bcc phase and the orthorhombic phase based on Ti_2AlNb. Depending on the alloy composition, each phase was observed as a precipitate with a plate morphology in the matrix of the other phase. In both cases the phases share a common direction, $[011]_{bcc} \parallel [001]_{ort}$, and interface (habit) plane, $(2\bar{1}1)_{bcc} \parallel (1\bar{1}0)_{ort}$. Geometrical patterns of plates of the different orientational variants were also observed. Analysis of the orientation relation, habit plane and plate patterns are consistent with the concept of a strain-type transition even though long range diffusion is required.

1. INTRODUCTION

Recent studies of the phase equilibrium in the Ti-Al-Nb system show the presence of an apparently equilibrium ternary ordered orthorhombic (ORTH) phase at low temperatures based on Ti_2AlNb stoichiometry [1,2]. This phase has the Cmcm space group and a proposed ordering which, if perfect, has 4 Al atoms in the $4c_1$ Wyckoff position, 4 Nb atoms in the $4c_2$ position and 8 Ti atoms in the 8g position [1]. The phase is structurally related to the hexagonal DO_{19} Ti_3Al phase by additional chemical ordering involving Ti and Nb in the basal plane and the associated orthorhombic distortion [1]. This ORTH phase is also structurally related to the BCC structure in the same manner as the orthorhombic α'' martensite which forms from the high temperature BCC phase in Ti-Nb and Ti-Ta systems during quenching [3,4].

The structural relationship between the ORTH phase and BCC can be described as shuffles of alternating $(110)_c$ cubic planes along the $[1\bar{1}0]_c$ direction plus a homogeneous strain with principal axes along the $[110]_c$, $[001]_c$, and $[1\bar{1}0]_c$ directions. A special ratio of the principal strains in the $(110)_c$ plane and shuffles to the close-packed positions will produce hexagonal symmetry, i.e. the α phase. The well-known lattice correspondence, shown in Fig. 1, was first determined for α'' martensite by Bagaryatskii [3], as: $[100]_o \simeq \langle 001\rangle_c$; $[010]_o \simeq \langle 1\bar{1}0\rangle_c$; $[001]_o \simeq \langle 110\rangle_c$ (o - ORTH, c - BCC cubic). The α'' martensitic phase is disordered and has the Cmcm space group with 4 atoms per centered unit cell (4c Wyckoff position) [3,4]. The ordered ORTH phase has a unit cell which is twice as large as the disordered martensite in the basal plane.

A pseudo-binary section of the the ternary Ti-Al-Nb between the compositions TiAl and TiNb must have the Ti_2AlNb ORTH phase near the center and the BCC TiNb(Al) phase on one side at low temperatures. Therefore, a two phase field between these two phases is anticipated. The structural relationship between these phases will be seen to play a major role in the development of the observed two-phase microstructures, which have the potential of being coarsening-resistant microstructures. Microstructures with either a presumably soft (disordered) matrix and harder (ordered) precipitates or vice versa can be produced depending on composition. Such combinations are currently being examined as artificial composites of γ-TiAl with Nb-Ti alloys [5]. A study of the microstructures and phase equilibria developed at 700°C is the main purpose of this work.

2. EXPERIMENTAL PROCEDURE

Two alloys with compositions Ti_4AlNb_3 (Alloy 1) and Ti_2AlNb (Alloy 2) were prepared by arc melting. A minimum of ten remelts was necessary to ensure mixing of the components. Cast buttons were homogenized at 1400°C for three hours in a vacuum tight furnace under 2/3 atm of gettered Ar. During heat treatment samples rested on a Y_2O_3-coated Al_2O_3 substrate supported on a moveable pedestal which could be lowered out of the hot zone of the furnace into a lower chamber. The cooling rate of the samples during such quenching was estimated to be about 400°C/min. SEM microprobe of these samples gave compositions of Ti-12.2 at % Al-37.2 at % Nb and Ti-23.9 at % Al-25.0 at % Nb. Oxygen, nitrogen and hydrogen levels were 500, 320, 34 and 500, 130, 22 wppm for Alloys 1 and 2 respectively.

For the study of the two phase equilibrium, the homogenized samples were annealed at 700°C for 26 days. In order to understand the details of the formation of the microstructure of the Ti_2AlNb alloy, annealing at 700°C for different lengths of time was also done. The annealings were performed by encapsulating Ta foil-wrapped samples in evacuated and He-backfilled quartz tubes.

TEM foils were prepared by standard twin-jet electropolishing procedure using a 300 ml methanol, 175 ml n-butanol and 30 ml $HClO_4$ electrolyte at 0°C. X-ray diffraction was performed from the surface of unetched metallographic specimens to determine matrix lattice parameters.

3. RESULTS

3.1 Microstructure of the 1400°C annealed samples

Optical metallography of both alloys reveals the absence of the dendritic microsegregation of the cast structure and the presence of very coarse (mm size) single phase grains. TEM examination shows that for both alloys the high temperature phase was preserved during cooling and is BCC with B2 (CsCl) ordering. As mentioned in our earlier publication [6], the superlattice reflections due to the B2 ordering are much stronger for Alloy 2 than for Alloy 1 (Fig. 2a,b). For Alloy 2, no anti-phase domain boundaries due to the B2 ordering were observed in dark-field imaging. These boundaries should have been present after cooling at 400 K/min if the alloy was disordered BCC at 1400°C. For Alloy 1, the superlattice reflections are so weak that dark-field imaging was practically impossible.

Strong diffuse streaks along the <011>* reciprocal directions and a complex diffuse shape for the fundamental reflections, possibly due to intersection of the streaks with the Ewald sphere, are characteristic of both alloys. These features are seen in selected area electron diffraction (SAD) patterns (Fig. 2a,b) which show both alloys in a [100] zone axis orientation. As a consequence of these diffraction effects, two-beam images show striation or "tweed" contrast. The striation directions lie approximately along the traces of $(110)_c$ planes. This tweed structure is a precursor of the shear transformation that completely converts the B2 to the ORTH after short aging times of Alloy 2 at 700°C as described in section 3.4. In some locations a high density of dislocations of unknown origin were also observed.

3.2 ORTH Precipitates in a BCC Matrix

After annealing at 700°C for 26 days, the Alloy 1 microstructure consists of a matrix phase (with the same grain size as at 1400°C) and micron size precipitates uniformly distributed in the matrix (Fig. 3a,b). The precipitates are frequently found connected to each other in a V-shaped or zig-zag morphology composed of different orientational variants, reminiscent of many martensitic structures. Observations of different TEM foils suggest a plate-like shape of the precipitates. Closer observation shows that the plates most often have a lens-type cross-section and that the curved interfaces separating the precipitate and the surrounding matrix contain interfacial dislocations and ledges (Fig. 4). Within the matrix phase, strong distortions of unclear origin are indicated by diffuse and distorted spots in selected area diffraction (SAD) patterns. These distortions are similar to those observed in SAD patterns for samples annealed at 1400°C (Fig. 2).

Fig. 5 shows a SAD pattern taken from an area which includes the matrix and several variants of precipitate. On the basis of such SAD patterns, together with microdiffraction from individual precipitates, the precipitate phase was identified as the ORTH Ti_2AlNb and the matrix phase was identified as the disordered BCC phase. The presence of these and no other phases was confirmed by X-ray diffraction, from which the lattice parameters were determined as: $a_o = 0.605$ nm; $b_o = 0.961$ nm; $c_o = 0.465$ nm for the ORTH phase, and $a_c = 0.328$ nm for the BCC phase. EDX using experimental Cliff-Lorimer coefficients (obtained from a homogeneous sample of known composition) showed that the phases were different in composition with the following estimates (without thickness correction) of the phase compositions: Ti_2AlNb for the ORTH phase and Ti-45 at% Nb-10 at% Al for the BCC phase.

Indexing of the SAD pattern for two variants of the ORTH phase and the matrix is shown in Fig. 5. Within the accuracy available from SAD, the orientation relationship[1] (OR) between the two phases was determined:

$$[011]_c \parallel [001]_o$$
$$(\bar{2}\bar{1}1)_c \parallel (110)_o \text{ (for the first variant)}$$
$$(21\bar{1})_c \parallel (1\bar{1}0)_o \text{ (for a second variant).}$$

Considering the structural similarity between the ORTH and close-packed hexagonal phase, the OR is the same as the well-known Burger's OR between BCC and HCP phases. This orientation relationship gives 12 orientational variants of the ORTH phase in the BCC matrix - two rotated ±3° around each of the six $<110>_c$ matrix phase directions.

---

[1] The orientation relation can also be written as $[011]_c \parallel [001]_o$ and $[1\bar{1}1]_c \parallel [1\bar{1}0]_o$.

Fig. 6 shows an image of a precipitate plate in an orientation where $(1\bar{1}2)_c/(110)_o$ are parallel to the electron beam. In this orientation the precipitate/matrix interface has long straight segments which are the edge-on $(1\bar{1}2)_c/(110)_o$ planes. As determined by trace analysis, the average habit plane of the lenticular precipitates has the approximately the same orientation. Macroscopically curved parts of the lenticular interface are constructed of terraces of $(1\bar{1}2)$ planes with a density of steps related to the deviation from the $(1\bar{1}2)$ plane. Observation of the inclined interfaces in the TEM foil suggests that the terrace edges are not fixed crystallographically.

3.3 BCC Precipitates in an Orthorhombic Matrix

After annealing at 700°C for 26 days, the Alloy 2 microstructure consists of a matrix phase containing a small volume fraction of fine, uniformly dispersed precipitates. Formation of this equilibrated microstructure was found to be a relatively complex process, which is described below. The matrix phase was identified by SAD as the ORTH Ti_2AlNb phase. CBED patterns similar to those shown by Banerjee et al. [1] confirmed the Cmcm space group. Fig. 7a shows an image of the precipitates when the matrix is oriented with its $[001]_o$ zone axis (corresponding SAD in Fig. 8) parallel to the electron beam. The precipitates are disk-like (seen edge on) with their parallel habit planes taking two different orientations, $(110)_o$

and $(1\bar{1}0)_o$ of the matrix. Imaging of the precipitates with the habit plane inclined shows the disk morphology (Fig. 9). The disk thickness ranges between 3 and 10 nm.

In addition to the $[001]_o$ zone axis reflections of the matrix, the SADP in Fig. 8 shows reflections belonging to the precipitate phase, which were indexed as those of the BCC phase. There are two rotational variants of the BCC phase corresponding to two different habit plane orientations, so that $[1\bar{1}0]_c \parallel [001]_o$ and either $(112)_c \parallel (110)_o$ for the $(110)_o$ habit plane, or $(11\bar{2})_c \parallel (1\bar{1}0)_o$ for the $(1\bar{1}0)_o$ habit plane. The orientation relationship and habit plane are the same as that found for Alloy 1.

Although the disk-like precipitate morphology was the one most commonly observed, two other forms were occasionally noticed. One is a disk with bulging faces as shown in Fig. 10a. Here the curved faces of the precipitate consist of ledges with $(110)_o$ terraces similar to those found for Alloy 1. The edges of the ledges do not show any particular crystallographic directions and are curved as can be seen from an inclined image taken of the precipitate (Fig. 10b). These bulging disks are thicker than the flat disks (~30 nm) and probably represent an advanced stage of coarsening.

The other shape observed occasionally was a very long (several μm), relatively thin, parallel-sided plate (Fig. 11). The plate has a habit plane which can significantly deviate from the observed $(110)_o$-type. These very long plates are usually connected to a grain boundary, as described below.

3.4 Mechanism of formation of the 700°C equilibrium microstructure

For Alloy 1, the formation of the equilibrium 700°C microstructure was a one step process involving the precipitation of the second phase (ORTHO) from a supersaturated matrix (BCC) established at high temperature. For Alloy 2, as the different annealing times at 700°C show, the precipitation step was preceded by two other steps:

(a) complete transformation of the retained high temperature B2 phase to the ORTH phase with a highly faulted microstructure;

(b) recrystallization of the faulted ORTH phase into fault-free ORTH grains.

Fig. 12 shows typical microstructures of alloy 2 after annealing at 700°C for 15 min (a), 24 hr (b) and 7 days (c). As micrograph (a) demonstrates, the initial B2 phase was completely transformed during this short time to a single phase, plate-like structure of the ORTH phase. This plate-like morphology suggests a martensitic-type transformation accompanied by chemical ordering. The defect structure of the plates can be removed by subsequent recrystallization, the beginning of which is observed in Fig. 12b. New grains of the ORTH phase are free of defects, and precipitation of the equilibrium BCC phase occurs either in the bulk, or at moving grain boundaries, Fig. 12c. Details of this martensitic transformation will be published elsewhere [7].

4. DISCUSSION

We will first discuss the possible shape of the pseudobinary TiNb-Ti_2AlNb section of the phase diagram and account for the sequence of transitions which occur upon cooling from the B2 phase field. We then focus on the observed orientation relation, the habit plane of the precipitates, and their macroscopic arrangement using three complementary approaches. Using only the point group symmetries of the involved phases, possibilities for orientation relations and precipitate shapes with extremal energies are investigated. Consideration of the lattices spacings of the involved phases permits a determination of the transformation strain between the two phases and the effect of elastic energy on the precipitate morphology, OR and arrangement. This continuum mechanics approach was developed for martensitic transformations, but has been successfully used in many cases for diffusion controlled precipitation [8-10]. Finally the crystallographic details of the interfacial structure and atomic matching will be considered.

4.1 Phase Diagram and Transformation Path

The phase constitution at various temperatures is summarized in Fig. 13a. We have included additional unpublished results [7] on heat treated samples of alloy 2 at temperatures of 1100, 970, 940, 890, 850°C and alloy 1 at 1100°C. A partial pseudobinary section between the compositions TiAl and TiNb is shown. In the composition range between TiAl and Ti_2AlNb, equilibrium involving α_2, γ, and a $B8_2$ phase at 700°C [11] are not shown. Due to the preliminary nature of the phase diagram work, the diagram is approximated as a quasibinary for simplicity. This is reasonable because tie lines appear to lie fairly close to the plane of the section according to the measured compositions. The ORTH phase has Ti and Nb substitution on Ti sites of the α_2 Ti_3Al, keeping ~25 at % Al [1]. Thus the width of this phase in a section at constant Ti content is likely to be quite narrow. The BCC to B2 transition has been assumed to be second order with no two-phase field. The composition TiNb is disordered BCC at all temperatures above ~ 550°C [12]. In fact the BCC phase shows a calculated metastable miscibility gap at 513°C [12]. Thus the B2 phase does not exist in the Ti-Nb binary and the BCC-B2 transition temperature must plunge at high Nb content in the pseudobinary diagram. This curve must intersect the upper ORTH to B2 boundary somewhere between 700 and 850°C to be consistent with the data. Above the temperature of this intersection, the equilibrium is ORTH with B2, while below it the equilibrium is ORTH with BCC. This latter equilibrium is responsible for the plate-like structures studied in the present paper.

With this preliminary phase diagram one can now interpret the sequence of transitions which occur on cooling alloys 1 and 2 from 1400 and ageing at 700°C. Schematic free energy composition diagrams at 1100 and 700°C are also shown in Fig. 13b,c. This permits the sketching of a B2 to ORTH T_0 curve. On cooling from 1400°C, alloy 2 crosses this T_0 curve making it possible to form the ORTH phase at constant composition. This transformation has much of the fine structure of a martensitic reaction but appears to occur isothermally during short aging times at 700°C. This ORTH phase is supersaturated with Nb and is unstable with respect to the formation of a two phase mixture of ORTH and BCC phases.

For alloy 1 cooling from 1400°C provides the possibility to form a very weakly ordered B2 phase prior to the precipitation of the ORTH precipitates consistent with the observations. The position of the metastable extension of the order-disorder line into the BCC + ORTH field would determine this possibility. Because this phase is supersaturated with Al, aging would produce ORTH precipitates and a subsequent loss of B2 order in the matrix.

4.2 Orientation Relation and Plate Habit Plane

Symmetry Considerations - The crystallographic symmetries of the precipitated phase and the matrix (surrounding media) phase can provide basic information about various allowed orientations and precipitate morphologies. According to Cahn and Kalonji [13], an intersection group must be determined. The intersection group (for more general cases called the group of the Wulff plot, W) is the group of point symmetry elements that are common for both crystals in the relative orientation under investigation. The ratio of the index of group W to the index of the group of the matrix phase (the index is equal to the number of symmetry elements) is the number of precipitate variants. The symmetry of the W group puts constraints on the precipitate morphology, and also shows if the orientation relationship is a symmetry-dictated extremum [13].

In the present case, the BCC phase has $m\bar{3}m$ point group of order 48, and the ORTH phase has mmm point group of order 8 [14]. Stereographic projections of the point group elements of both phases are shown in Fig. 14 a,b. We can classified all possible OR's according to the symmetry of the intersection group.

The highest symmetry will be mmm (2/m 2/m 2/m), which is the same as that of the ORTH phase. This occurs for OR's where three orthogonal 2-fold axes of the ORTH phase coincide with an orthogonal triplet of 4- or 2-fold axes (<100> or <110>) of the BCC phase.

The next highest symmetry of the intersection group is obtained by rotating the above OR about one of the coincident 2-fold axes (Fig. 14c). The symmetry will be monoclinic 2/m of order 4, and does not depend on the rotation angle. For this case the number of variants can be simply found. If the BCC phase is the matrix (as in Alloy 1), there are 12 orientational variants of the ORTH phase precipitate (12 = 48/4). When the ORTH phase is the matrix (as in Alloy 2), there are only 2 orientational variants of the BCC phase precipitate (2 = 8/4).

A third type of ORs with no parallel 2-fold axes have an intersection group $\bar{1}$ of order 2. It gives 4 variants of the BCC precipitates in the ORTH matrix and 24 variants of the ORTH precipitates in the BCC matrix.

The second type of OR with 2/m intersection group symmetry corresponds to that observed experimentally in the present work for both types of precipitates, i.e. $[011]_c \parallel [001]_o$ and $(2\bar{1}1)_c \parallel (1\bar{1}0)_o$. For the 2/m intersection group there is a symmetry dictated extremum only with respect to changes which would splay the two superimposed 2/m axes. Rotations of the OR around this 2/m symmetry axis do not have a symmetry preferred orientation. Therefore, parallelism of the $(110)_c$ and $(001)_o$ planes is dictated by a symmetry extremum (Because it is experimentally observed it is a minimum.) and locked-in for some range of lattice parameters and external conditions. On the other hand, the apparent parallelism of the $(112)_c$ and $(110)_o$ planes in the observed OR is not a symmetry extremum, and therefore continous deviations are expected which would depend on lattice parameters of the phases and interfacial energy, and in general on temperature or composition.

The 2/m intersection group also gives the minimal symmetry of the precipitate form. One of the monoclinic 2/m point group forms is a pinacoid composed of planar faces which are parallel to the 2-fold axis (the faces are hk0 planes for the ORTH phase and corresponding $h\bar{h}l$ planes of the BCC phase) [15]. In other words, the faces must be planes containing $[001]_o$ and

$[110]_c$. The precipitate form corresponds to the experimentally observed planar disks. Since the h,k and l indexes are not restricted, the angle of the disk plane about the 2/m axis is not fixed by symmetry. Therefore other reasons must be found to understand the observed low index habit plane.

Calculation of Habit Plane and OR using Minimization of Elastic Energy - There are two basic assumptions required for the elastic approach:

1. The transformation BCC $\rightleftharpoons$ ORTH is considered to result from a strain of one lattice into another and from shuffling of the $(011)_c$ or $(001)_o$ planes.
2. The coherency of the two-phase state is maintained, i.e., displacements of all points are continuous (strains are compatible). This is only true if the displacement of the shuffles, for which the average strain is zero, is ignored.

The lattice deformation required for this transformation written in orthonormal coordinate system coinciding with the $[100]_c$, $[0\bar{1}1]_c$, and $[011]_c$ axes of the cubic lattice and corresponding to the edges of the ORTH cell (Fig. 1) is described by the matrix:

$$\overset{\approx}{D} = \begin{pmatrix} \lambda_a & 0 & 0 \\ 0 & \lambda_b & 0 \\ 0 & 0 & \lambda_c \end{pmatrix} = \begin{pmatrix} 1 & 0 & 0 \\ 0 & 1 & 0 \\ 0 & 0 & 1 \end{pmatrix} + \begin{pmatrix} \epsilon_a & 0 & 0 \\ 0 & \epsilon_b & 0 \\ 0 & 0 & \epsilon_c \end{pmatrix} \equiv \overset{\approx}{1} + \overset{\approx}{\epsilon}_o \qquad (1)$$

where $\lambda_a = a_c/(a/2) = 1.084$, $\lambda_b = a_c\sqrt{2}/(b/2) = 0.965$, $\lambda_c = a_c\sqrt{2}/c = 0.998$ using the measured values for the values for the lattice constants. $\overset{\approx}{\epsilon}_o$ is the self strain of the ORTH → BCC transformation. Its principle values are $\epsilon_a = 1-\lambda_a = 0.084$, $\epsilon_b = 1-\lambda_b = -0.035$, and $\epsilon_c = 1-\lambda_c = -0.002$.

Minimization of elastic energy can lead to many different precipitate shapes. For the present case, the shear is large compared to the dilatation;

i.e., $[(\epsilon_a - \epsilon_b)/2]/[(\epsilon_a + \epsilon_b + \epsilon_c)/3] \approx 4$, and thus the minimum of elastic energy corresponds to the plate shape for precipitates [16].

The equilibrium orientation of plate habit planes has been discussed in [17-19]. When the principle strains ϵ_a, ϵ_b, ϵ_c have different signs (as in the present case), it was shown that the precipitate could be uniaxially stressed along one of the axes associated with principal strains of the same sign [17]. This axis would be unrotated after transformation. The stress effectively changes the lattice strain required for transformation to one having a zero eigenvalue in this direction. The elastically strained precipitate phase and the matrix can then have an invariant plane. The invariant plane would be the equilibrium habit plane of the plate precipitate. The habit plane contains this unrotated axis as a zone axis. This is equivalent to the hypothesis of Dahmen [19] that the habit plane which contains an invariant line and another direction of small lattice strain can minimize the elastic energy of a coherent plate.

In the present case the invariant axis is the c-axis because the principle strain ϵ_c is an order of magnitude less than the other strain with the same sign (ϵ_b). The small value of the strain ϵ_c in comparison with other principle strains determines the stability of the observed orientation relation $(001)_o \parallel (011)_c$ with respect to small variations of the lattice parameters. This agrees with the symmetry dictated extremum concept above.

The deformation $\overset{\approx}{D}$ combined with the elastic strain associated with the uniaxial stress in the c-direction gives the invariant plane strain, $\overset{\approx}{D}'$ as

$$\overset{\approx}{D}' = \overset{\approx}{D} + \overset{\approx}{\epsilon}_{el} = \begin{pmatrix} \lambda_a & 0 & 0 \\ 0 & \lambda_b & 0 \\ 0 & 0 & \lambda_c \end{pmatrix} + \begin{pmatrix} \nu\epsilon_c & 0 & 0 \\ 0 & \nu\epsilon_c & 0 \\ 0 & 0 & -\epsilon_c \end{pmatrix} = \begin{pmatrix} \lambda_a' & 0 & 0 \\ 0 & \lambda_b' & 0 \\ 0 & 0 & 1 \end{pmatrix} \qquad (2)$$

where $\lambda'_a = \lambda_a + \nu\epsilon_c$, $\lambda'_b - \lambda_b + \nu\epsilon_c$, and ν is the Poisson ratio. The normal to the invariant plane, $\bar{n}$, the displacement, $\bar{s}$, and the rotation about the c-axis of the BCC lattice with respect to the ORTH lattice, θ, can be obtained in the normal way [20] from

$$\overset{\approx}{R}\overset{\approx}{D}' = \overset{\approx}{1} + \bar{s} \otimes \bar{n} \tag{3}$$

where $\bar{s} \otimes \bar{n}$ is a diadic product $(s_i n_j)$ and

$$\overset{\approx}{R} = \begin{Bmatrix} \cos\theta & \sin\theta & 0 \\ -\sin\theta & \cos\theta & 0 \\ 0 & 0 & 1 \end{Bmatrix}. \tag{4}$$

Defining two parameters Λ and r by

$$\Lambda = \{(\lambda_a'^2 - 1)/(1 - \lambda_b'^2)\}^{\frac{1}{2}} \tag{5}$$

$$r = \lambda'_b/\lambda'_a, \tag{6}$$

the normal $\bar{n}$ and displacement $\bar{s}$ in the *ORTH frame are*

$$n_1/n_2 = \pm \Lambda, \; n_3 = 0; \quad s_1/s_2 = \mp r\Lambda, \; s_3 = 0, \tag{7}$$

and in the BCC (rotated) frame they are

$$n_1/n_2 = \pm r\Lambda, \; n_3 = 0; \quad s_1/s_2 = \mp \Lambda, \; s_3 = 0, \tag{8}$$

with

$$|\bar{s}| = |\lambda'_a - \lambda'_b|. \tag{9}$$

The rotation, θ of the BCC frame about the c-axis with respect to the ORTH frame is given by

$$\cos\theta = \frac{1 + \lambda'_a\lambda'_b}{\lambda'_a + \lambda'_b}. \tag{10}$$

For the present lattice parameters, $\theta = \pm 3.10°$. This rotation agrees with the orientation relation found; i.e., $(1\bar{1}0)_o$ parallel to $(2\bar{1}1)_c$. Assuming $\nu = 0.3$, $n_1/n_2 = 1.392$ in the BCC frame. This plane is only 0.4° away from $(2\bar{1}1)_c$ in close agreement with the observed habit. (The angle between $(2\bar{1}1)_c$ and $(100)_c$ is 35.3°, between the invariant plane and $(100)_c$ is 35.7°). Accordingly the corresponding invariant plane in the ORTH lattice is very closed to $(1\bar{1}0)_o$. For the displacement, $s_1/s_2 = -1.566$ in the BCC frame. This direction is 2.7° from $[21\bar{1}]_c$ (the angle between $[21\bar{1}]_c$ and $[100]_c$ is 35.3°, between the displacement direction and $[100]_c$ is 32.6°). The corresponding direction in the ORTH lattice is close to $[110]_o$.

It is evident that the calculated habit plane orientation as well as the orientation relation must change with changing lattice parameters. In contrast to the relation $[001]_o \parallel [011]_c$, the relation $(1\bar{1}0)_o \approx \parallel (2\bar{1}1)_c$ is not stable to small changes in lattice parameters from an elastic point of view. So the conclusions of the examination of the orientation relations using the minimum elastic energy principle are in agreement with result of the symmetry analysis.

Microscopic atomic matching along the habit plane - The interface energy is a minimum when densely-packed planes of the lattices are in good matching contact along the habit plane. We will examine possible atomic matchings of the interface for the observed $(2\bar{1}1)_c/(1\bar{1}0)_o$ habit plane. Since this plane is very close to an invariant one for the measured lattice parameters of the phase, the directions in the habit plane are invariant. Fig. 15 shows one of the possible atomic structures of the interface as viewed along $[001]_o$. One can see the expected perfect matching, as well as the magnitude of the displacement $\bar{s}$.

Deviation from the $(2\bar{1}1)$ habit plane orientation must lead to a creation of terraces with steps of the $(2\bar{1}1)$ planes approximating the interface. This situation is connected with a sharp increase of the interface energy. For a habit plane which deviates slightly from $\{2\bar{1}1\}_c$, the interstep distance ℓ would be very large. In general, only for a plate of thickness $h \gg \ell$ can one expect that the equilibrium habit be determined by a minimum of elastic energy rather than the surface energy [21]. In the present case, both elastic and atomic matching criteria are very close. Therefore the exact orientation $(2\bar{1}1)_c$ can correspond to the minimum even if the trend to a minimum of elastic energy alone dictates slight deviation from this plane.

It should be pointed out that the sole use of a matching criterion of $(110)_o/(2\bar{1}1)_c$ planes to define the OR will in fact predict an addition non-observed OR; i.e., where $(110)_o$ is parallel to $(1\bar{1}2)_c$. This OR was not predicted using the elastic approach above since it would require a different lattice correspondence with a much larger displacement.

4.3 Arrangement of Plates

The plates can exist almost without stress along the plane faces. For a precipitate embedded in a matrix and formed by a strain transformation, each plate has an edge field similar to the field of a dislocation loop with Burgers vector

$$\bar{b} = h\bar{s} \qquad (11)$$

where h is the plate thickness, $\bar{s}$ is the displacement determined above.

The energy of the system of plates can be decreased [21] if the plates form in special arrangements with the edges in close proximity if, like a dislocation reaction, the energetic criterion

$$|\bar{b}_1|^2 + |\bar{b}_2|^2 > |\bar{b}_1 + \bar{b}_2|^2 \qquad (12)$$

is satisfied. The plates will join if the plane of the junction has low surface energy; i.e., a small angle boundary or a twin boundary.

For a BCC plate in the ORTH matrix, the displacement lies nearly parallel to the habit plane and the energy of the combined edge fields decreases if the habits associated with different variants form obtuse angles with each other. It is evident that the misorientation of the lattices of contacting precipitates across the plane of the junction is small and equals twice the angle between the planes $(2\bar{1}1)_c$ and $(110)_o$ before the transformation. In the case of the BCC precipitates, such a configuration was indeed observed although rarely because of the low density of precipitates.

Among all possible pairs of plates of the ORTH phase in the BCC matrix, only plates which intersect each other along $<111>_c$ satisfy the condition of good matching and the criterion of Eqn. 12 (they meet each other at a twin boundary, $\{110\}_c$ or $\{111\}_o$). Thus we should observe zig-zag chains and triangles of plates with a 60° dihedral angle between habit plates. Such is the case in the present investigation (e.g. Fig. 3). A similar arrangement of plates is typical for martensitic transformations [22-23].

5. CONCLUSIONS

The observed precipitation reactions of both BCC in ORTH and ORTH in BCC phases were shown to be well described by the formalism developed for martensitic transformations. The approach of elastic energy minimization predicts all characteristic features of the observed microstructure; i.e., OR, habit planes, morphology and arrangement of precipitates. Nevertheless the kinetics of the transformations are clearly controlled by both short- and long-range diffusion in order to form precipitates differing in composition and site occupancy from that of the matrix. Two extreme mechanisms of precipitation - (1) martensitic growth with subsequent chemical redistribution and (2) nucleation by fluctuation controlled by only interfacial energy (atomic matching) - may both be ruled out. The first one does not explain the gradual development of the microstructure. The second one, even if yielding the correct OR and habit, would not explain the plate arrangements, and further would give an additional non-observed OR as discussed in 4.2.

We believe that in the present case precipitation occurs by the same lattice reconstruction involving structural dislocations or ledges as for the martensitic BCC to α' (HCP) or α'' (ORTH) transformation. However nucleation and propagation of the ledges is controlled by diffusion of species. The elastic field accumulated during growth is apparently not relaxed by plastic deformation and plays a role in the nucleation of different variants in a correlated way which minimizes overall energy.

ACKNOWLEDGEMENT

The authors acknowledge the efforts of F. S. Biancaniello, M. E. Williams, and A. J. Shapiro. Discussions with J. W. Cahn are greatly appreciated. Research performed under DARPA Order #6065.

REFERENCES

1. D. Banerjee, A. K. Gogia, T. K. Nandi and V. A. Joshi, Acta Met. 36, 871.
2. H. T. Kestner-Weykamp, C. H. Ward, T. F. Broderick and M. J. Kaufman, Scr. Met. (1989) 1697.
3. I. A. Bagaryatskii, G. I. Nosova and T. V. Tagunova, Sov. Phys. Doklady, 3, 914 (1959).
4. A. R. G. Brown, D. Clark, J. Eastebrook and K. S. Jepson, Nature, 201, 914 (1964).
5. G. R. Odette, G.Lucas, S. W. Sheckherd and E. H. Aigeltinger, Mat. Res. Soc. Symp. Proc. (1990) in press.
6. L. A. Bendersky and W. J. Boettinger, Mat. Res. Soc. Symp. Proc., 133, 45-50 (1989).
7. L. A. Bendersky and W. J. Boettinger, NIST, unpublished research.
8. H. M. Ott and T. B. Massalski, Acta Met., 6, 494 (1958).
9. A. Crosky, P. G. McDougall and J. S. Bowles, Acta Met. 28, 1495 (1980).
10. U. Dahmen and K.M. Westmacott, Acta. Met. 34, 475 (1986).
11. L. A. Bendersky, W. J. Boettinger, B. P. Burton, F. S. Biancaniello and C. Shoemaker, Acta Met. (1990) in press.
12. D. L. Moffat and U. R. Kattner, Met. Trans 19A (1988), 2389.
13. J. W. Cahn and G. Kalonji, in Proceedings of the International Conference on Solid-Solid Phase Transformation, The Metallurgical Society of AIME (1981), p.
14. International Tables of Crystallography, vol. A, ed. T. Hahn, D. Reidel Publishing Co. (1987).
15. M. J. Buerger, Elementary Crystallography, J. Wiley & Son, Inc. (1963).

16. I.M. Kaganova, A.L. Roitburd. Sov. Phys. JETP, 67, 1174 (1988); Sov. Phys. Crystal (1989).

17. A.L. Roitburd, N.S. Kosenko. Phys. Stat. Sol., A35, 735 (1976).

18. A.G. Khachaturyan, Theory of Structural Transformation in Solids, Wiley, New York, 1983.

19. U. Dahmen, Acta Met.,30, 63 (1982).

20. C. M. Wayman Introduction to the Crystallography of Martensitic Transformation, Macmillan, New York, 1964.

21. A.L. Roitburd, in Solid State Physics, Vol. 33, H. Ehrenrach, F. Seits, D. Turnbull, eds., 1978, p. 317.

22. H. Warlimont, L. Delaey, in Progress Material Sci., Eds. B. Chalmers, J.W. Christian, T.B. Massalski, Pergamon, 1974.

23. L. M. Utevsky, M. N. Pankova, Metallofizica, 1, 66 (1979).

FIGURES

Fig. 1 Lattice correspondence between BCC and ORTH cells. Only one fourth of the ORTH cell is shown.

Fig. 2 Selected area electron diffraction (SAD) patterns which show both alloys, a) Ti_4AlNb_3 (Alloy 1) and b) Ti_2AlNb (Alloy 2), after cooling from 1400 °C in a [100] zone axis orientation. Strong diffuse streaks along the $<011>^*$ directions and a diffuse shape for the fundamental reflections is characteristic of both alloys. The superlattice 001 reflections due to the B2 ordering are much stronger for Alloy 2.

Fig. 3 Arrangements of lenticular plate-shaped precipitates of the ORTH phase in a BCC matrix in zig-zag arrays, observed in Ti_4AlNb_3 annealed at 700 °C for 26 days. a) SEM, b) TEM, $[111]_c$ orientation of the foil.

Fig. 4 Bright-field image of lenticular precipitates of the ORTH phase in a BCC matrix showing interface dislocations. Ti_4AlNb_3 annealed at 700 °C for 26 days.

Fig. 5 Selected area diffraction (SAD) pattern taken from an area which includes several differently oriented precipitates and the matrix. Indexing of the SAD pattern for two variants of the ORTH phase

(1,2) and the matrix (c) is also shown. Ti_4AlNb_3 annealed at 700 °C for 26 days.

Fig. 6 Image of a precipitate with its interface surface edge-on (parallel to an electron beam direction). The precipitate/matrix interface has long straight segments which are edge-on $(1\bar{1}2)_c/(110)_o$ planes. Curved segments of the interface are constructed of steps (ledges) of the same $(1\bar{1}2)_c/(110)_o$ planes. Ti_4AlNb_3 annealed at 700 °C for 26 days.

Fig. 7 Image of a BCC precipitate in an ORTH matrix. The matrix is oriented with its $[001]_o$ zone axes (corresponding SADP in Fig. 8) parallel to the electron beam. The precipitates are disk-like with their parallel habit planes taking two different orientations of the matrix, $(110)_o$ and $(1\bar{1}0)_o$. Ti_2AlNb after a 26 day heat treatment at 700 °C.

Fig. 8 SADP showing the presence of reflections belonging to the precipitate phase. The reflections were indexed as those of the BCC phase. There are two rotational variants of the BCC phase corresponding to two different habit plane. Ti_2AlNb annealed at 700 °C for 26 days.

Fig. 9 Same as Fig. 7 but with imaging of the precipitates with the habit plane inclined to the beam direction showing the disk-like morphology.

Fig. 10 (a) Ocassionally-observed bulging plate. Faces consist of $(110)_o$ terraces. (b) Dark-field image of the inclined plate showing that the terraces end at edges which show no particular orientation. Ti_2AlNb annealed at 700 °C for 26 days.

Fig. 11 Long thin plate of BCC phase formed at a moving grain boundary during recrystallization. Ti_2AlNb annealed at 700 °C for 26 days.

Fig. 12 Microstructure of Ti_2AlNb annealed at 700 °C for a) 15 min., b) 24 hr., c) 7 days.

Fig. 13 (a) Partial pseudobinary section of the Ti-Al-Nb system at 50 at. % Ti showing proposed equilibrium boundaries between ORTH, BCC an B2 phases estimated from the data shown. Alloys 1 and 2 are on the right and left respectively. (b,c) Schematic free energy - composition diagrams at 1100° and 700°C showing the location of B2 to ORTH T_o curve.

Fig. 14 Stereographic plots of point group symmetries. a) BCC $m\bar{3}m$. b) ORTH mmm shown in an orientation relative to a) which superimposes three orthogonal 2-fold axes of the ORTH phase with an orthogonal triplet of 4- or 2-fold axes (<100> or <110>) of the BCC phase. The intersection point group is mmm. c) superposition of m3m and mmm corresponding to the orientation relation $[011]_c \parallel [001]_o$ and $(2\bar{1}1)_c \parallel (1\bar{1}0)_o$ and yielding an intersection point group of 2/m.

Fig. 15 Possible atomic matching across $(1\bar{1}0)_o/(211)_c$ interface plane, (a) viewed in projection along $[001]_o$. Different size circles represent different occupancies; open and closed circles represent different layers of $(001)_o/(011)_c$.

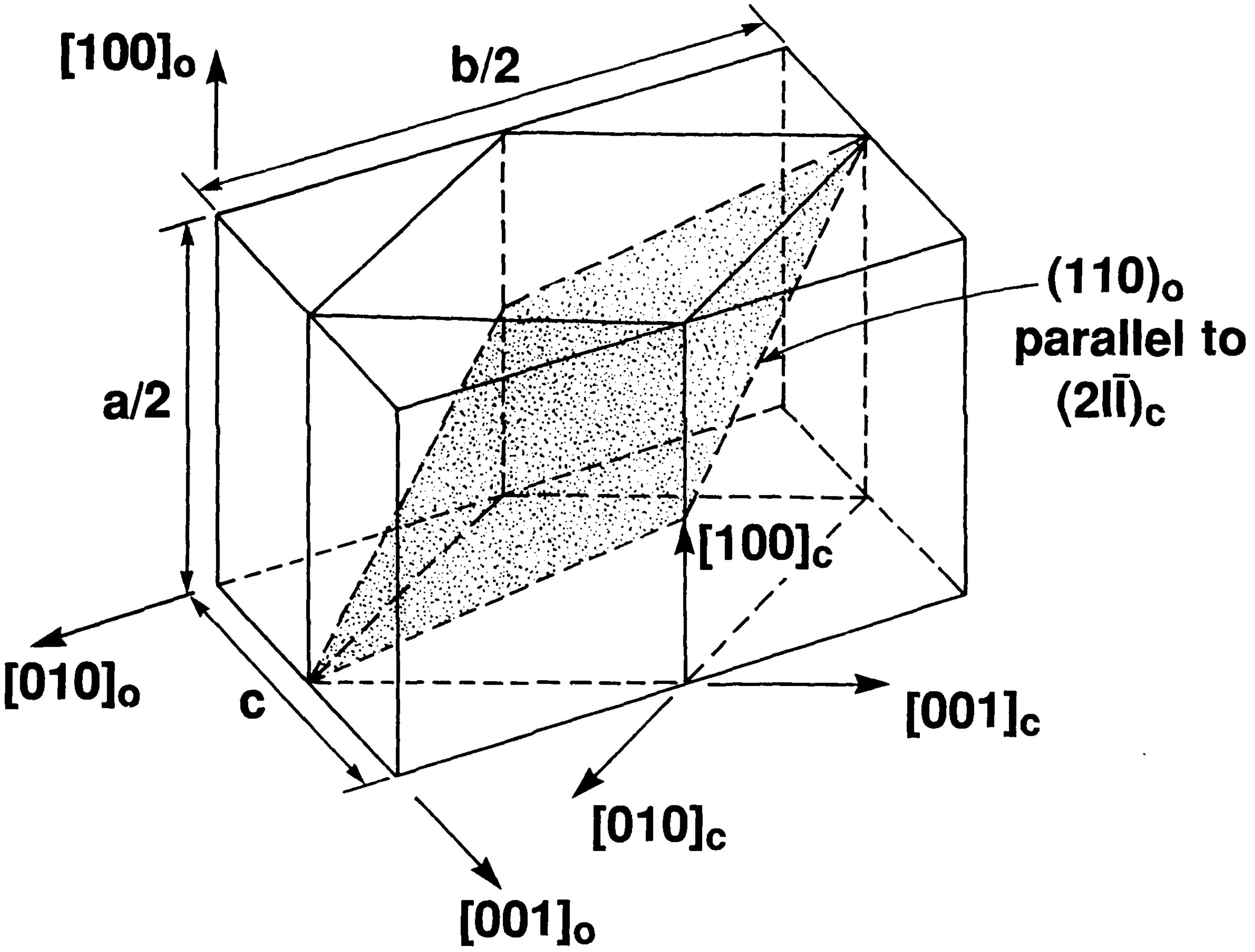
$[100]_o$
b/2
a/2
$(110)_o$ parallel to $(2\bar{1}\bar{1})_c$
$[100]_c$
$[010]_o$
c
$[001]_c$
$[010]_c$
$[001]_o$

Fig1

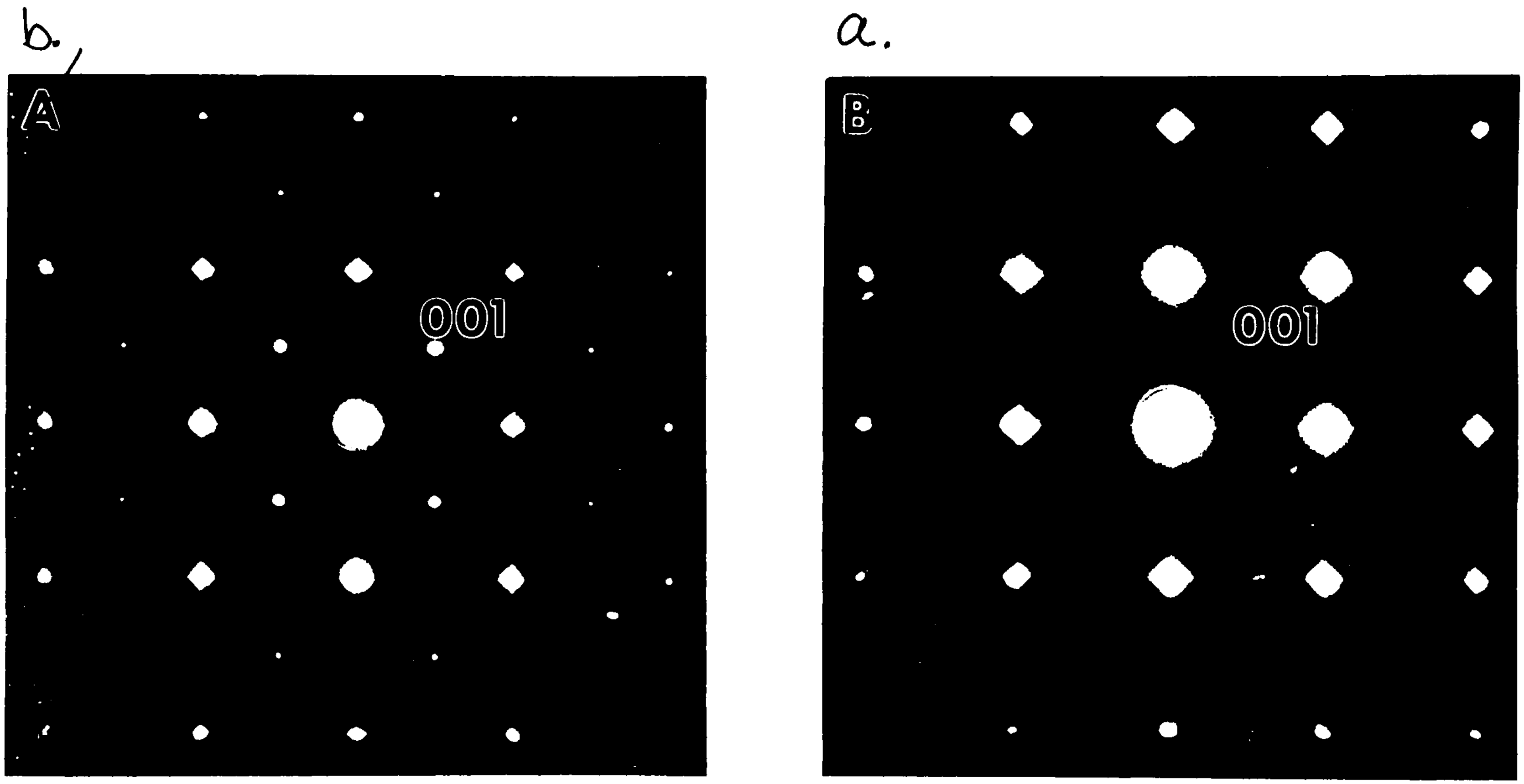

b.

a.

Fig 2

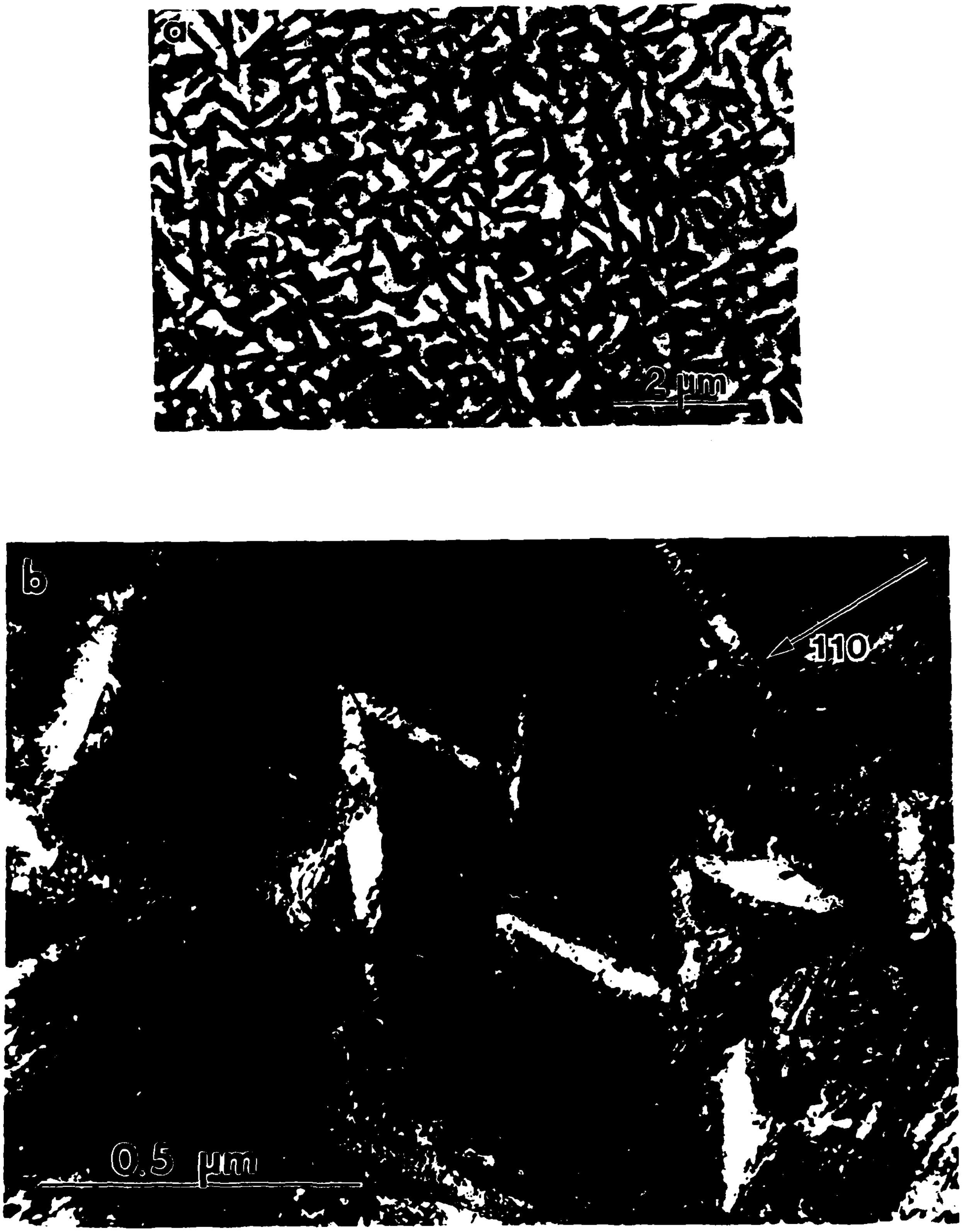
a
2 µm
b
110
0.5 µm

Fig3

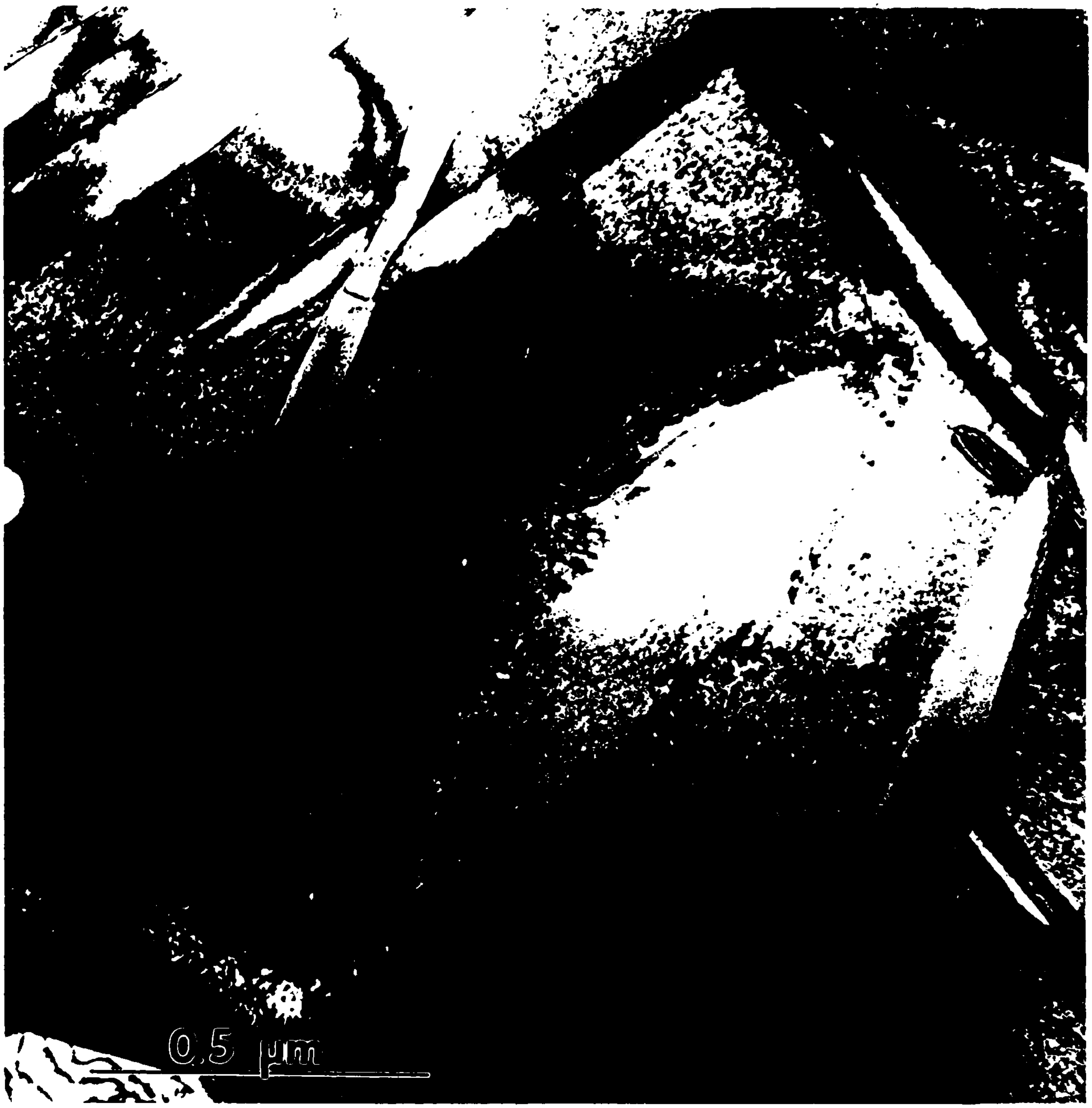

Fig 4

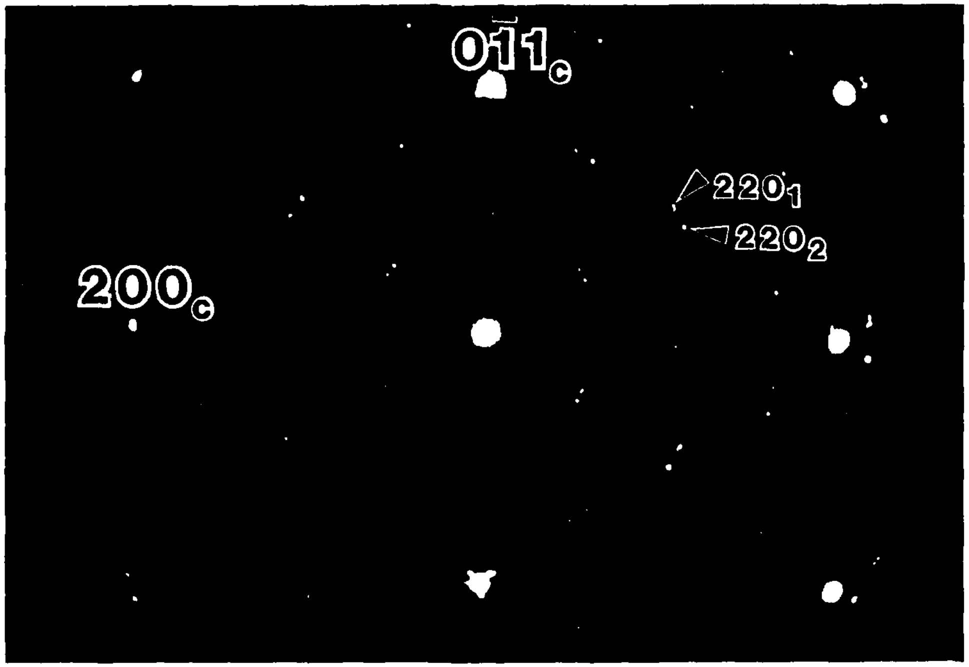
$0\bar{1}1_c$
220_1
220_2
200_c

Fig 5

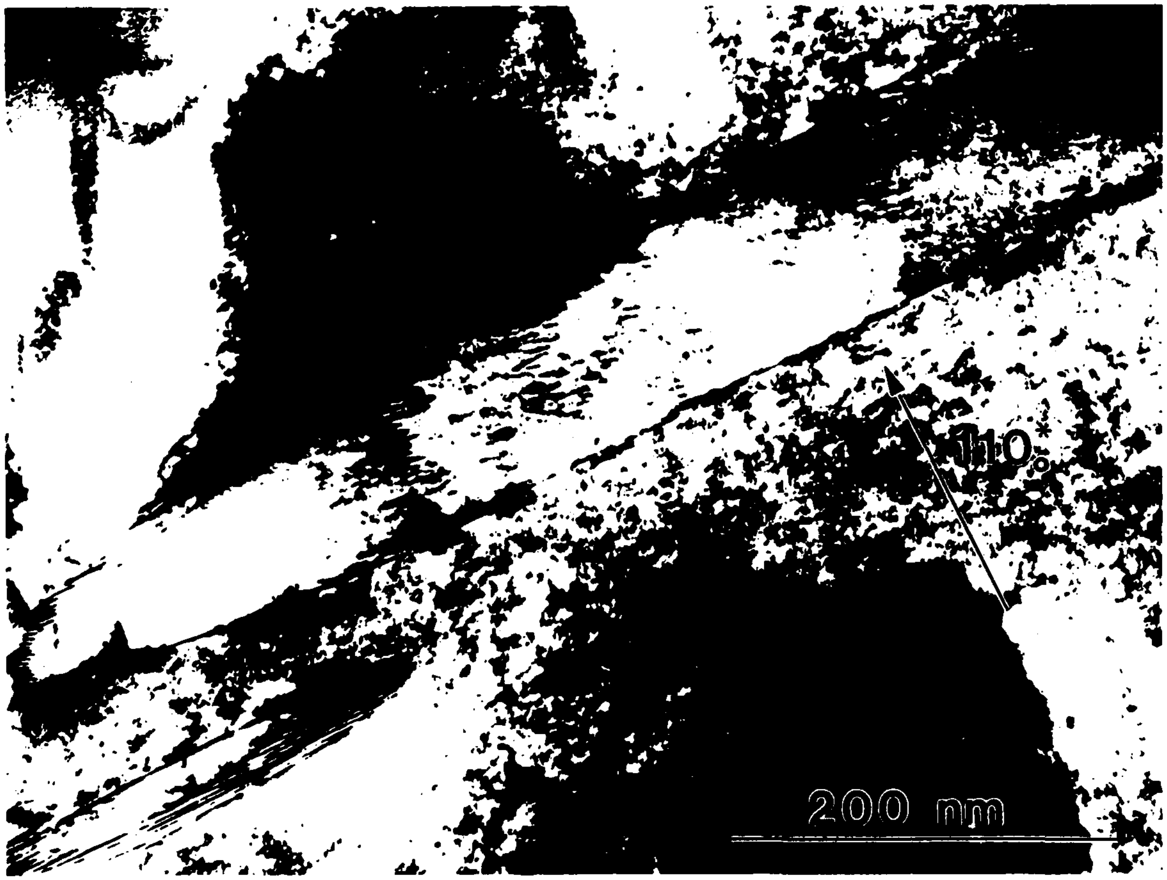

Fig 6

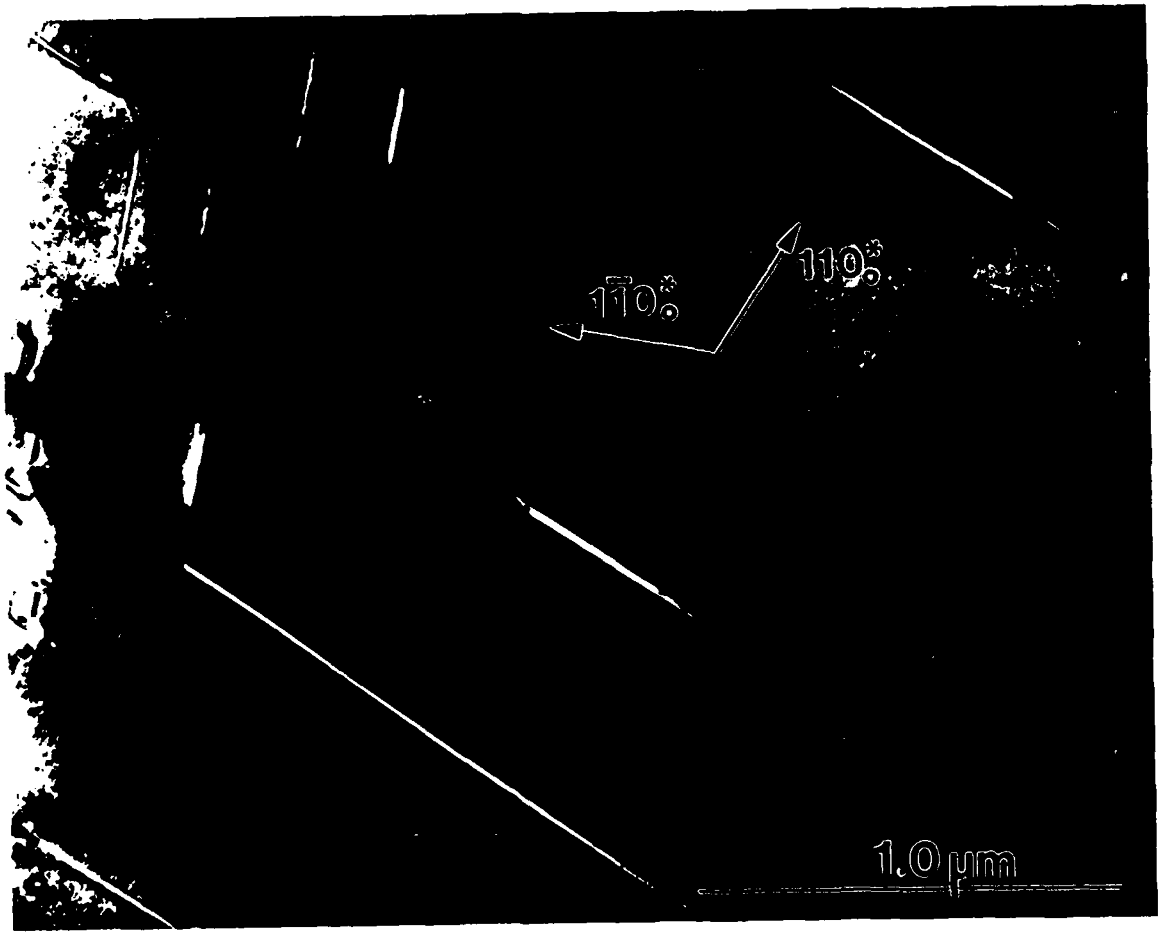
$110^{*}_{\circ}$
$\bar{1}10^{*}_{\circ}$
1.0 µm

Fig 7

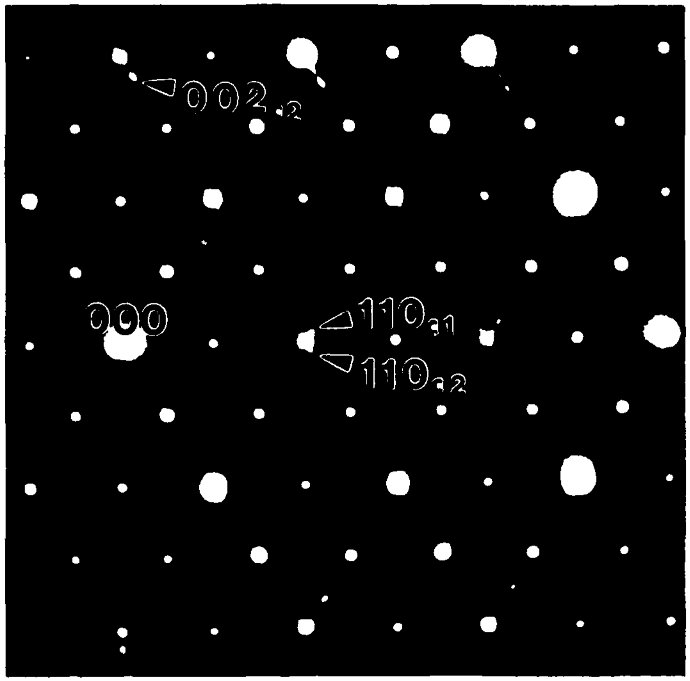

002a2
000
110a1
110a2

Fig 8

Fig 9

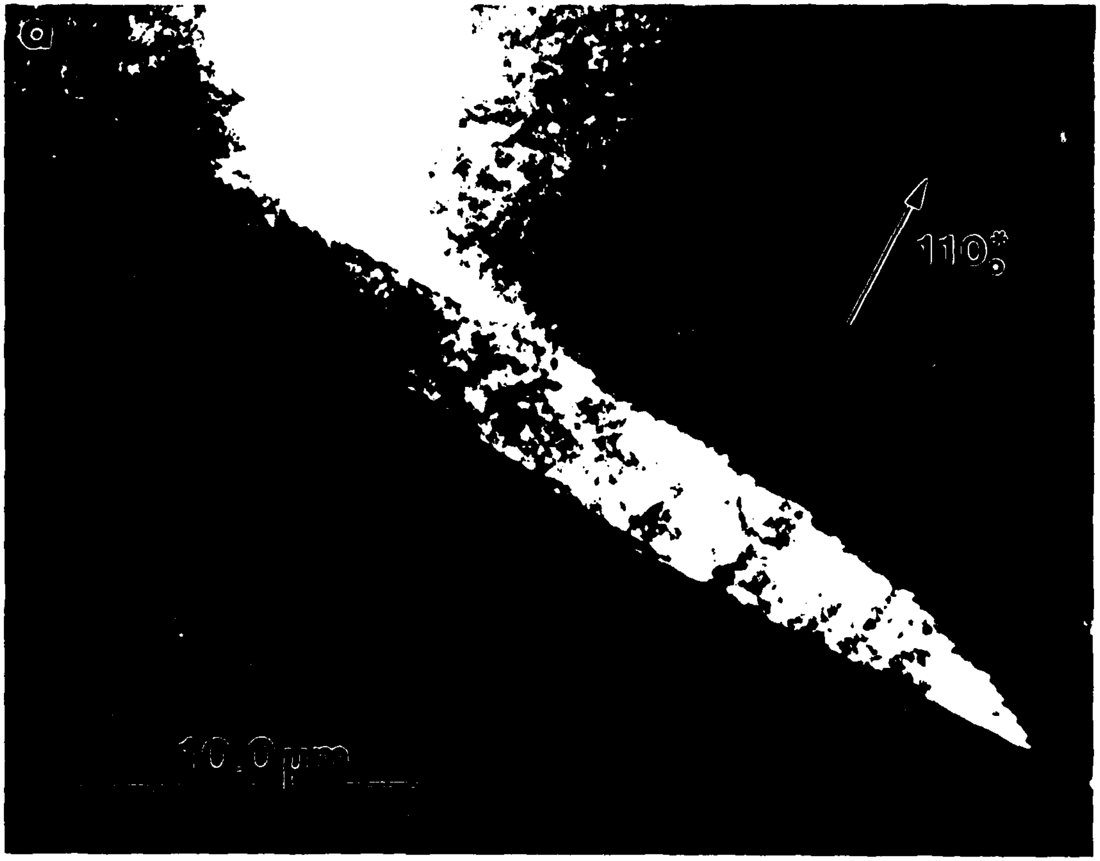
a
110_{o}^{*}
10.0 µm

Fig 10a

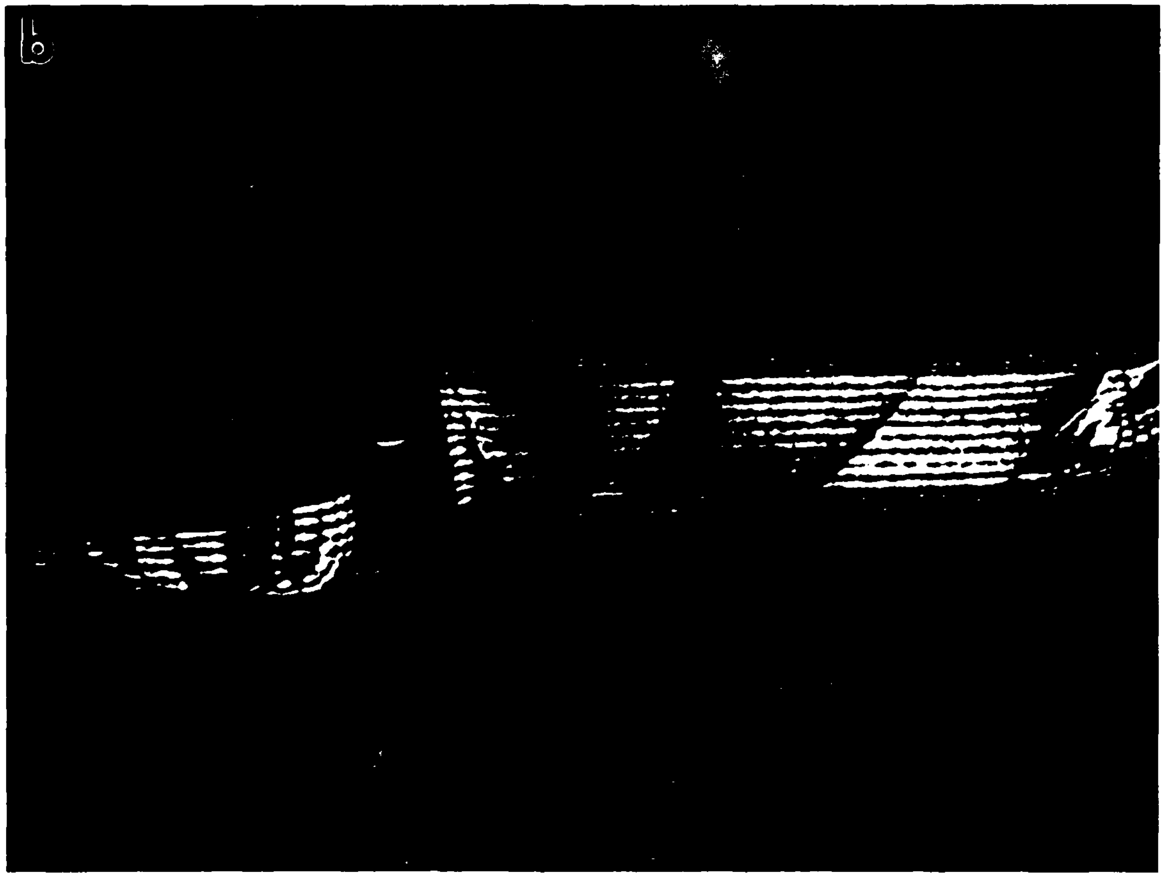

Fig10b

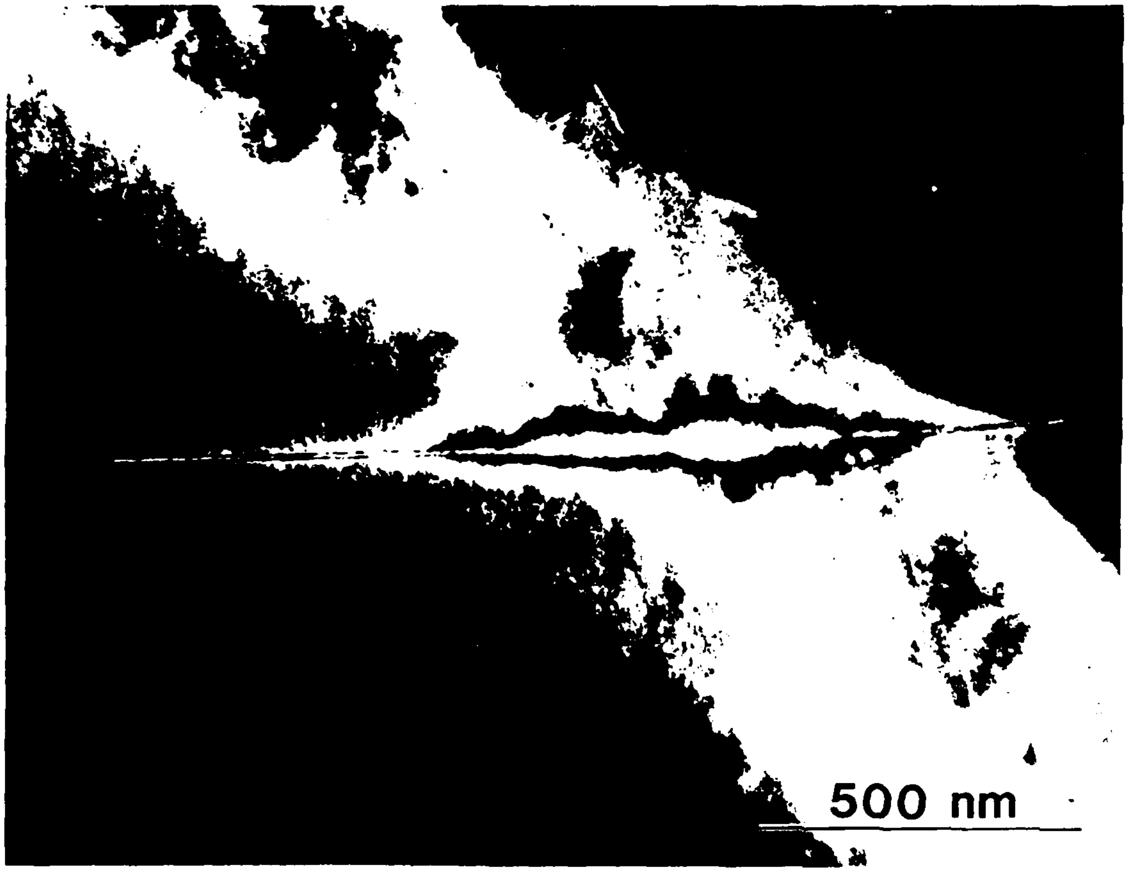

Fig 11

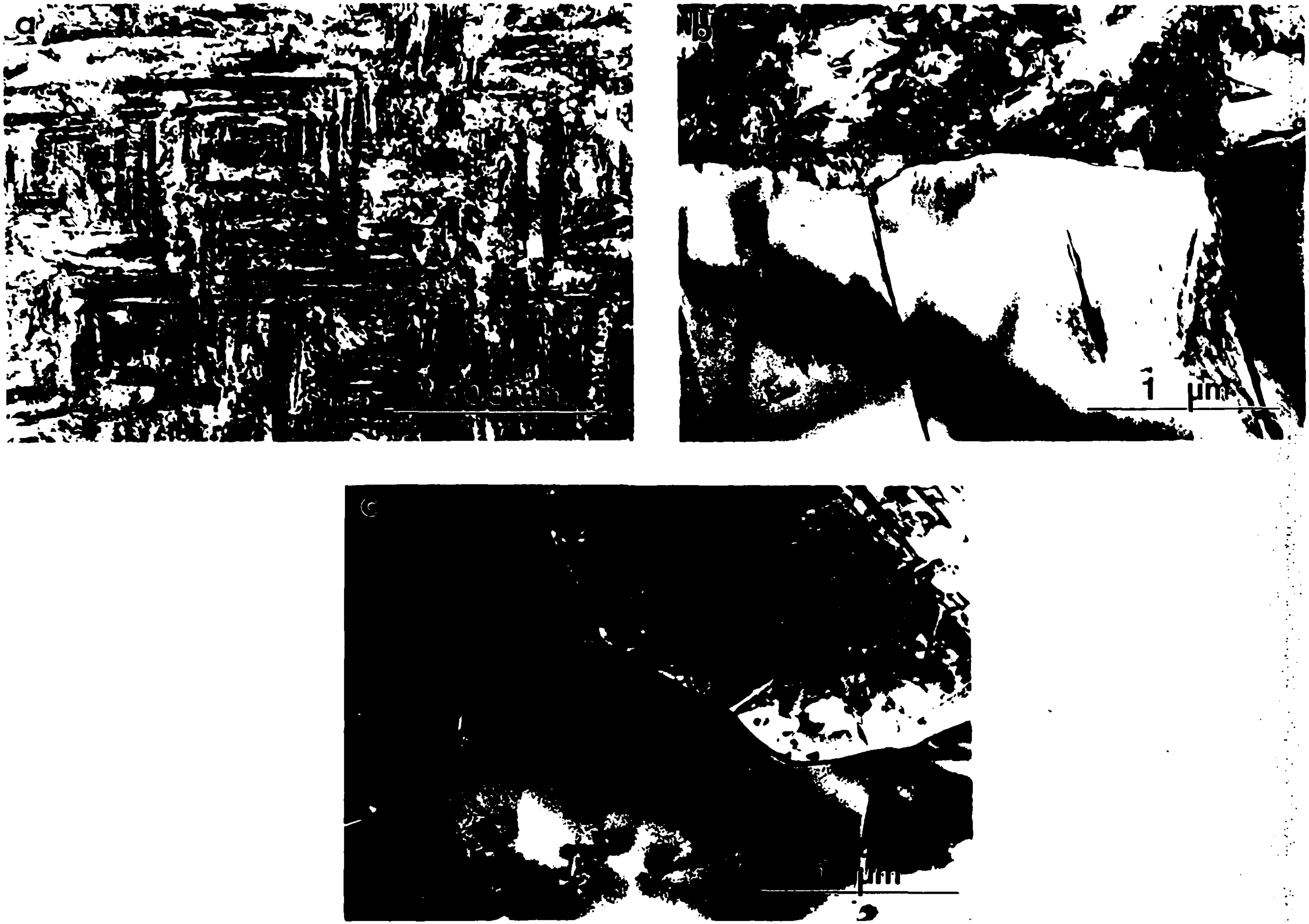
a
500 nm
b
1 µm
c
1 µm

Fig 12

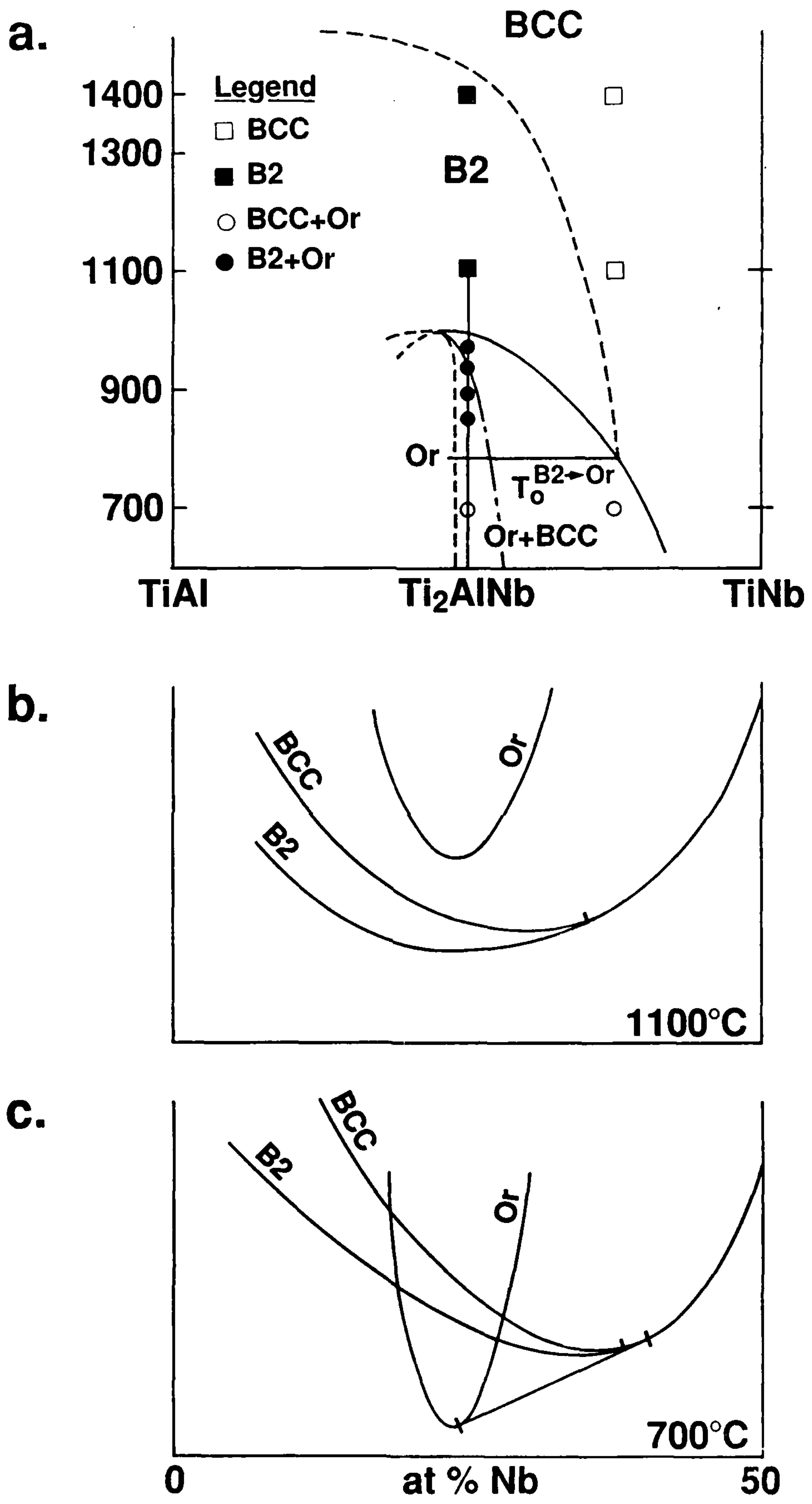
a.
BCC
Legend
□ BCC
■ B2
○ BCC+Or
● B2+Or
1400
1300
1100
900
700
B2
Or
$T_o^{B2\rightarrow Or}$
Or+BCC
TiAl
Ti_2AlNb
TiNb
b.
BCC
B2
Or
1100°C
c.
B2
BCC
Or
700°C
0
at % Nb
50

Fig 13

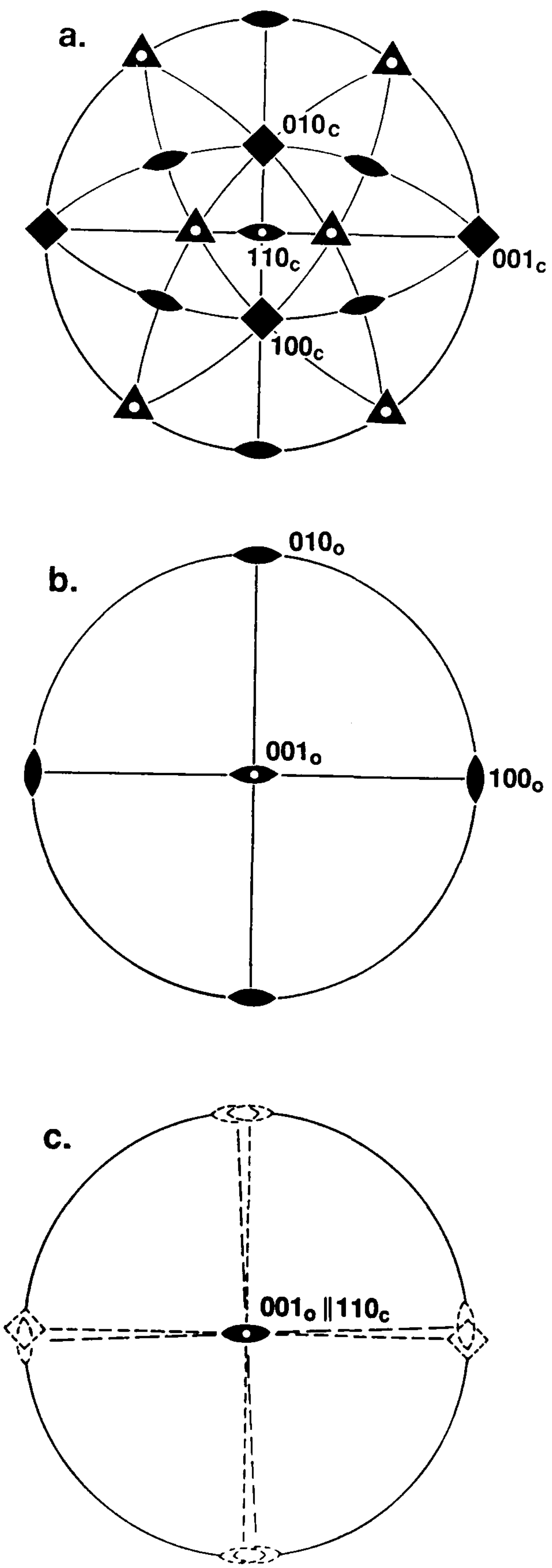
a.
010_c
110_c
001_c
100_c
b.
010_o
001_o
100_o
c.
$001_o \parallel 110_c$

Fig14

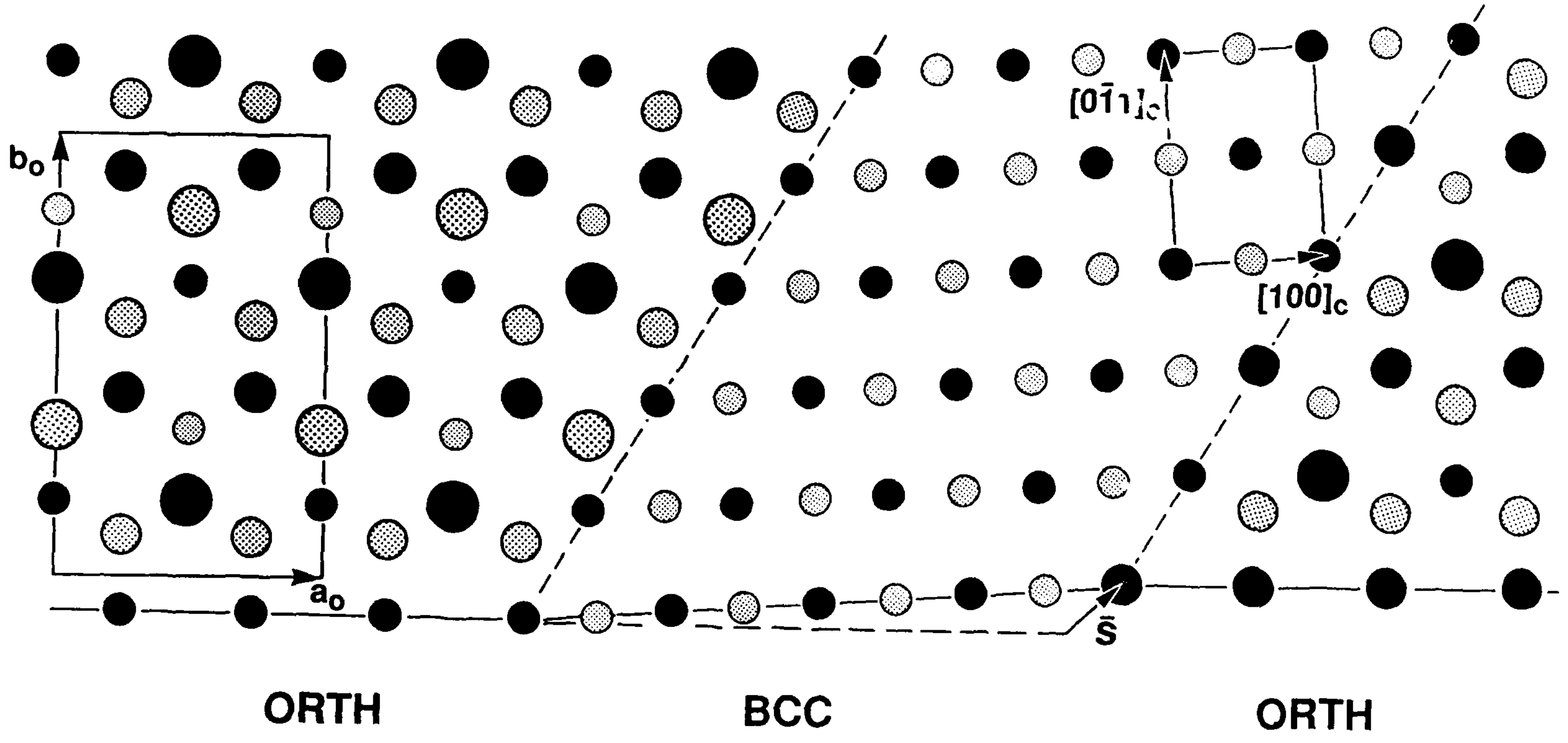
b_o
a_o
$[0\bar{1}1]_c$
$[100]_c$
$\bar{S}$
ORTH
BCC
ORTH

Fig 15

Abstract of paper to be published in the proceedings of "The Seventh International Conference on Rapidly Quenched Metals" to be held Aug .13-17, 1990, Stockholm, Sweden

DISORDER TRAPPING IN Ni_2TiAl

W. J. Boettinger, L. A. Bendersky and J. Cline
NIST, Gaithersburg, MD, USA

M. J. Aziz, G. Q. Lu and J. A. West
Harvard, Cambridge, MA, USA

Objective. To determine whether the Heusler alloy, Ni_2AlTi, with the $L2_1$ crystal structure will form a less ordered related crystal structure, B2 or BCC, after laser surface melting and rapid resolidification.

Methods. Arc melted material was homogenized by heat treatment at 1400°C in gettered Ar for 6 h. Disks 3 mm in dia. and 1 mm thick were prepared by diamond sawing and spark cutting. Laser irradiation of optically polished disks was performed using a pulsed laser with 335 mJ of energy focussed to different spot sizes. Simultaneous measurement of reflectivity was performed to determine the time that the specimen surface was molten, permitting estimation of solidification velocity by way of heat flow calculations. TEM samples were prepared by back grinding and one-sided electropolishing/ion milling to preserve the thin ($\sim 1\ \mu m$) melted region. High temperature X-ray diffraction studies were performed on the homogenized material to be certain of the presence of Heusler order up to the melting point.

Results. The melting point of Ni_2AlTi is 1513 ± 5°C. High temperature x-ray diffraction up to 1425°C showed no reduction in the $L2_1$ superlattice reflection intensities. This indicates that Ni_2AlTi has $L2_1$ order up to the melting point.

Examination of the melted regions by TEM showed in some cases (with the smallest spot size) the presence of a high density of antiphase boundaries in the L21 structure whereas in other cases no domains were observed. Such domains would only be expected when a solid state ordering has occurred. These domain boundaries had <100> displacements indicating that the occurence of a B2 to $L2_1$ transition. No evidence of APB's with <111> displacements was detected indicating the absence of a BCC to B2 transition. These observations strongly suggest that the rapid solidification produced the B2 structure and that subsequent cooling to room temperature produced the $L2_1$ structure and the fine domains. It is not known at present whether higher solidification rates might produce the BCC structure.

Conclusion. Pulsed laser melting and rapid resolidification can induce disorder trapping in Ni_2AlTi. The alloy formed from the melt with the nonequilibrium B2 structure and subsequently transformed to the equilibrium $L2_1$ Heusler structure.